

Design, Analysis and Testing of Rotary type Micro Thermal Actuators

M. Arefin Anwar

A thesis
in
The Department
of
Mechanical and Industrial Engineering

Presented in Partial Fulfillment of the Requirements
For the Degree of Master of Applied Science (Mechanical Engineering) at
Concordia University
Montreal, Quebec, Canada

November 2006

© M. Arefin Anwar, 2006



Library and
Archives Canada

Bibliothèque et
Archives Canada

Published Heritage
Branch

Direction du
Patrimoine de l'édition

395 Wellington Street
Ottawa ON K1A 0N4
Canada

395, rue Wellington
Ottawa ON K1A 0N4
Canada

Your file *Votre référence*
ISBN: 978-0-494-28935-8
Our file *Notre référence*
ISBN: 978-0-494-28935-8

NOTICE:

The author has granted a non-exclusive license allowing Library and Archives Canada to reproduce, publish, archive, preserve, conserve, communicate to the public by telecommunication or on the Internet, loan, distribute and sell theses worldwide, for commercial or non-commercial purposes, in microform, paper, electronic and/or any other formats.

The author retains copyright ownership and moral rights in this thesis. Neither the thesis nor substantial extracts from it may be printed or otherwise reproduced without the author's permission.

AVIS:

L'auteur a accordé une licence non exclusive permettant à la Bibliothèque et Archives Canada de reproduire, publier, archiver, sauvegarder, conserver, transmettre au public par télécommunication ou par l'Internet, prêter, distribuer et vendre des thèses partout dans le monde, à des fins commerciales ou autres, sur support microforme, papier, électronique et/ou autres formats.

L'auteur conserve la propriété du droit d'auteur et des droits moraux qui protègent cette thèse. Ni la thèse ni des extraits substantiels de celle-ci ne doivent être imprimés ou autrement reproduits sans son autorisation.

In compliance with the Canadian Privacy Act some supporting forms may have been removed from this thesis.

Conformément à la loi canadienne sur la protection de la vie privée, quelques formulaires secondaires ont été enlevés de cette thèse.

While these forms may be included in the document page count, their removal does not represent any loss of content from the thesis.

Bien que ces formulaires aient inclus dans la pagination, il n'y aura aucun contenu manquant.


Canada

Abstract

Micro electro mechanical system (MEMS) has opened a new horizon for realizing smaller physical systems. The current trend of developing any physical device for technological applications is to have smaller, economical, reliable and functional devices. MEMS has significantly scaled down the size of the devices while offering more functionality by having fully integrated devices in micro level. MEMS devices have also proven to be cost effective. In MEMS applications, researchers are consistently searching for innovative concepts to develop actuators, which play a key role in any integrated system. Micro electro thermal actuator is one such concept that offers more force and displacement than other mechanisms available in micro level. The present research effort is directed towards development of a novel rotary type micro thermal actuator that may be attractive for various optical applications like switching, diffraction, attenuation etc. This thesis proposes various design topologies which offer rotary motion of cold disc energized by electrical potential. The proposed designs are analyzed by analytical and finite difference methods along with finite element analysis using commercial software, ANSYS. A proposed design for the actuator is analyzed to evaluate influence of parameters. The parametric analysis examines the influence of parameters on the motion of the actuator. A prototype actuator and experiment setup is fabricated to test the performance of the design. The experimental results demonstrate the functionality and effectiveness of the proposed device as an actuator, as well as the validity of the modeling techniques used to simulate the performance of the novel rotary type micro thermal actuator.

This thesis is dedicated to
my mother
and
to the memory of my father

Acknowledgements

I would like to thank my supervisors Dr. Muthukumaran Packirisamy and Dr. A. K. W. Ahmed for showing interest in taking me as a research student and providing me the scope to work in the field of MEMS. I would also like to thank them for providing me advices, training, valuable time and financial support which made my research work and thesis a success.

I would also like to thank Canadian Microelectronics Corporation (CMC) for providing technical support and resources and granting me fabrication space for MEMS chip which enabled me to realize the conceptions pertaining to the novel device. I express my gratitude towards National Science and Engineering Research Council of Canada (NSERC) for providing financial support to obtain necessary infrastructure needed for making this research effort a reality. I take this opportunity to thank ENCS Concordia for SRT support.

My sincere thanks go to Mr. Amrandre Atre former Ph.D. student of Georgia Institute of Technology. He was very patient in reading numerous mails and providing me technical help when ever I got stuck in modeling the device using ANSYS. I also thank staffs specially Arlene Zimmerman at Department of Mechanical and Industrial Engineering for all of their help in my graduate studies.

I am indebted to my parents, sisters and friends who were always there in my down times. I also thank them for standing by me when I was emotionally unstable and at lost after loosing my father. I remember my father in this day who always encouraged me to be a better, well educated

successful person. Finally, I dedicate my work to my mother Mrs. Farida Anwar and my late father Mr. Md. Sirajul Anwar.

Table of contents	vii
List of Figures	ix
List of Tables	xvii
List of Abbreviations and Symbols	xviii
1. Introduction and Literature Review	1
1.1 Motivation	1
1.2 Introduction to MEMS	2
1.3 Challenges in MEMS Device Realization	4
1.4 Market Demand for MEMS Devices	5
1.5 Actuators for MEMS Application	8
1.5.1 Electrostatic Actuator	8
1.5.2 Electro Magnetic Actuator	10
1.5.3 Piezoelectric Actuator	10
1.6 Literature Review	11
1.7 Thesis Objective	19
1.8 Thesis Contribution	20
1.9 Thesis Overview	21
2. Micromachining and Proposed Design for Rotary Type Micro Thermal Actuator	22
2.1 Micromachining Techniques	22
2.1.1 Bulk Micromachining	22
2.1.2 Surface Micromachining	23
2.2 Working Principle of Electro Thermal Actuator	24

2.3	Design Variations in Electro Thermal Actuator	25
2.4	Proposed Design for Rotary Type Micro Thermal Actuator	28
2.5	Summary	36
3.	Modeling of Rotary Type Micro Thermal Actuator and Parametric analysis	37
3.1	Electro Thermal Analysis	37
3.1.1	Thermal Boundary Conditions	37
3.1.2	Analytical Method	38
3.1.3	Finite Difference Method	44
3.2	Rotational Analysis	49
3.3	Finite Element Analysis	50
3.4	Shape Factors	64
3.5	Result Discussions	64
3.6	Parametric Analysis	77
4.	Experimental Testing	85
4.1	Experimental Scheme	85
4.2	Experimental Results and Discussion	88
4.3.1	Validation for Design (1a)	88
4.3.2	Validation for Design (1b)	92
4.3.3	Validation for Design (2)	95
5.	Conclusion and Future Work	99
	Appendix-A: Multi User MEMS Process	102
	Appendix –B:	105
	References	116

List of Figures

Figure 1.1	Global consumptions of MEMS/ MST devices (a) in millions of US dollars and (b) in millions of units	6
Figure 1.2	Comparison of MEMS/ MST device usage by various sectors (Percentage of units) in 2001 and 2006	6
Figure 1.3	Total market for various MEMS/ MST products for the period of 2000-2009	7
Figure 1.4	Comparison of MEMS/ MST device usage by various sectors (Percentage of total units) in 2004 and 2009	7
Figure 1.5	Schematic diagram of the operating principle of an electrostatic microactuator	9
Figure 1.6	(a) Two dimensional electrostatic actuator and (b) a rotary electrostatic micro motor	9
Figure 1.7	(a) DLD™ (developed by Texas Instruments) and (b) linear electrostatic actuator in an optical switch	10
Figure 2.1	Cross section of bulk micromachined membrane integrated with bipolar electronics	23
Figure 2.2	Schematic diagram of processes involved in surface micromachining	23
Figure 2.3	A schematic of traditional in plane micro electro thermal actuator	25
Figure 2.4	Two arm horizontal micro thermal actuator with: (a) straight arm; (b) curved arms	30
Figure 2.5	Vertical electro-thermal actuator	26

Figure 2.6	Vertical electro-thermal actuator	26
Figure 2.7	Arrays of thermal actuators tethered with a flexible yoke	27
Figure 2.8	Chevron type micro thermal actuator	27
Figure 2.9	Schematic of rotary micro thermal actuator. Various segments of the actuator are represented by line shape	28
Figure 2.10	Schematics of square disc rotary actuator with: (a) two arms; (b) four arms	29
Figure 2.11	Schematics of circular disc rotary actuator with:	30
Figure 2.12	Layout diagram of the chip containing rotary type micro thermal actuator	32
Figure 2.13	(a) & (b) Scanning Electron Micrograph (SEM) of the chip containing rotary type micro thermal actuator fabricated in MUMPS technology	33
Figure 2.14	(a) Scanning Electron Micrograph (SEM) of Design (1a) & (b) Close up SEM of the square cold disc of Design (1a)	34
Figure 2.15	(a) Scanning Electron Micrograph (SEM) of Design (1b) & (b) Close up SEM of the square cold disc of Design (1b)	34
Figure 2.16	(a) Scanning Electron Micrograph (SEM) of Design (2) & Close up SEM of the cold disc of Design (2)	35
Figure 2.17	(a) Scanning Electron Micrograph (SEM) of Design (3) & (b) Close up SEM of the cold disc of Design (3)	35

Figure 3.1	(a) Schematic rotary type polysilicon thermal actuator, (b) One dimensional coordinate for the analysis of thermal actuator and (c) Heat transfer modes involved in a section of a micro thermal actuator	39
Figure 3.2	(a) Scheme of rotary type micro thermal actuator, (b) simplified coordinate system, (c) representation of FDM nodal system along the length of the actuator and (d) Heat transfer modes involved in ith element of micro thermal actuator	44
Figure 3.3	(a) Schematic rotary type polysilicon thermal actuator with square disc and (b) One dimensional coordinate system for the analysis of thermal actuator	48
Figure 3.4	(a) Schematic rotary type polysilicon thermal actuator with square disc and (b) One dimensional coordinate system for the analysis of thermal actuator	49
Figure 3.5	A 3-D model of Actuator Design (1a) in ANSYS	51
Figure 3.6	A 3-D model of Actuator Design (1b) in ANSYS	51
Figure 3.7	A 3-D model of Actuator Design (2) in ANSYS	52
Figure 3.8	A 3-D model Actuator Design (3) in ANSYS	52
Figure 3.9	Temperature solution for Model (1a) in ANSYS, under the application of 12V or 3.9606mA	54
Figure 3.10	Vector summation of displacement for Model (1a) in ANSYS, under the application of 12V or 3.9606mA	55

Figure 3.11	Temperature solution for Model (1b) in ANSYS, under the application of 12V or 3.9263mA	56
Figure 3.12	Vector summation of displacement for Model (1b) in ANSYS, under the application of 12V or 3.9263mA	56
Figure 3.13	Temperature solution for Model (2a) in ANSYS, under the application of 12V 4.0439mA	57
Figure 3.14	Vector summation of displacement for Model (2a) in ANSYS, under the application of 12V or 4.0439V	58
Figure 3.15	Temperature solution for Model (2b) in ANSYS, under the application of 12V or 4.0949mA	58
Figure 3.16	Vector summation of displacement for Model (2b) in ANSYS, under the application of 12V or 4.0949mA	59
Figure 3.17	Temperature solution for Model (2c) in ANSYS, under the application of 16.5V or 3.93mA	60
Figure 3.18	Vector summation of displacement for Model (2c) in ANSYS, under the application of 16.5V or 3.93mA	60
Figure 3.19	Temperature solution for Model (2d) in ANSYS, under the application of 16.5V or 3.9495mA	61
Figure 3.20	Vector summation of displacement for Model (2d) in ANSYS, under the application of 16.5V or 3.9495mA	61
Figure 3.21	Temperature solution for Model (3) in ANSYS, under the application of 20V or 3.1004mA	62

Figure 3.22	Vector Summation of displacement for Model (3) in ANSYS, under the application of 20V or 3.1004mA	63
Figure 3.23	Temperature distribution of Model (1a) under the application of 12V or 3.9606mA	65
Figure 3.24	Average temperature of one arm of Model (1a) at different applied voltages	65
Figure 3.25	Rotation of the cold disc of Model (1a) at different applied voltages	66
Figure 3.26	Temperature distribution of Model (1b) under the application of 12V or 3.9263mA	67
Figure 3.27	Average temperature of one hot arm of Model (1b) at different applied voltages	67
Figure 3.28	Rotation of the cold disc of Model (1b) at different applied voltages	68
Figure 3.29	Temperature distribution of Model (2a) under the application of 12V 4.0439mA	69
Figure 3.30	Average temperature of one hot arm of Model (2a) at different applied voltages	69
Figure 3.31	Rotation of the cold disc of Model (2a) at different applied voltages	70
Figure 3.32	Temperature distribution of Model (2b) under the application of 12V or 4.0949mA	70
Figure 3.33	Average temperature of one hot arm of Model (2b) at different applied voltages	71

Figure 3.34	Rotation of the cold disc of Model (2b) at different applied voltages	71
Figure 3.35	Temperature distribution of Model (2c) under the application of 16.5V or 3.93mA	72
Figure 3.36	Average temperature of one hot arm of Model (2c) at different applied voltages	73
Figure 3.37	Rotation of the cold disc of Model (2c) at different applied voltages	73
Figure 3.38	Temperature distribution of Model (2d) under the application of 16.5V or 3.9495mA	74
Figure 3.39	Average temperature of one hot arm of Model (2d) at different applied voltages	74
Figure 3.40	Rotation of the cold disc of Model (2d) at different applied voltages	75
Figure 3.41	Temperature distribution of Model (3) under the application of 20V or 3.1004mA	76
Figure 3.42	Average temperature of one hot arm of Model (3) at different applied voltages	76
Figure 3.43	Rotation of the cold disc of Model (3) at different applied voltages	77
Figure 3.44	Effect of omission of a pair of arms in Model (1)	78
Figure 3.45	Loading of 2 arms in Model (1b) with 4v in ANSYS and resulting potential effects	79
Figure 3.46	Effect of loading 2 arms in Model (1b) with different potentials	80
Figure 3.47	Effect of radius on the rotational behavior of the disc	81

Figure 3.48	Effect of beam dimension on the rotational behavior of the disc	82
Figure 3.49	(a) Model (3), Schematic of rotary type micro thermal actuator with curved beam, (b) Model (2e), Schematic of rotary type micro thermal actuator with straight beams	83
Figure 3.50	Comparison of rotational behavior of Model (3) and Model (2e) as a function of input current	83
Figure 4.1	Outline for rotation measurement for a rotary thermal actuator. Reference line is drawn in (a) before applying load and (b) after applying voltage	85
Figure 4.2	Block diagram for the experimental setup and (b) Voltage-current measurement scheme	86
Figure 4.3	Voltage-current measurement scheme	87
Figure 4.4	Experimental setup for measuring rotation of the rotary type micro thermal actuator	87
Figure 4.5	Appearance of hot spot i.e., maximum temperature in the beam	89
Figure 4.6	I-V characteristics curve for Design (1a) with $\rho_o = 2e-3$ ohm-cm	90
Figure 4.7	Characteristics curve based on tuned resistivity for Design (1a) with $\rho_o = 1.75e-3$ ohm-cm	91
Figure 4.8	(a) Picture of the disc taken before applying voltage and (b) picture of the disc taken after application of 15.29V	91
Figure 4.9	Variation of rotation against the applied voltages for Design (1a)	92
Figure 4.10	I-V characteristics curve for Design (1b) with $\rho_o = 2e-3$ ohm-cm	93

Figure 4.11	I-V characteristics curve based on tuned resistivity for Design (1b) with $\rho_o = 1.75e-3$ ohm-cm	94
Figure 4.12	(a) Picture of disc taken before applying voltage and (b) picture of the disc after application of 3.091V	94
Figure 4.13	Variation of rotation against the applied voltages for Design (1b)	95
Figure 4.14	I-V characteristics curve for Design (2) with $\rho_o = 2e-3$ ohm-cm	96
Figure 4.15	I-C characteristics curve based on tuned resistivity for Design (2) with $\rho_o = 1.75e-3$ ohm-cm	96
Figure 4.16	(a) Picture of the disc taken before applying voltage and (b) picture of the disc after application of 14.04V	97
Figure 4.17	Variation of rotation against the applied voltages for Design (2)	98
Figure A-1:	Cross section of Electrostatic motor after the MUMPS process is completed	103
Figure A-2:	Cross section of Electrostatic motor after release	103

List of Tables

Table 2.1: Dimensional Parameters for the Proposed Designs	31
Table 3.1: Dimensions of Various Models	53
Table 3.2: Properties used for Simulations	63
Table 3.3: Shape factor for cold disc of various models	64
Table 3.3: Shape factor for cold disc of various models	83
Table B-1: Experiment photographs on Design (1a)	105
Table B-2: Experiment photographs on Design (1b)	108
Table B-3: Experiment Photographs on Design (2)	112

List of Abbreviations and Symbols

A	Constant
A_c	Cross sectional area of any element
A_s	Surface area of any element
B	Constant
c	Co-efficient
C	Co-efficient matrix
C_p	Specific heat of polysilicon
dx	Length of an arbitrary element along the actuator
i	Node index
I	Current
J	Current density
k	Time index
K_n	Thermal conductivity of Silicon Nitride
K_p	Thermal conductivity of polysilicon
K_{po}	Thermal conductivity of Poly0
l_c	Length of cold disc
ΔL_c	Thermal expansion of cold disc
l_h	Length of a hot arm
ΔL_h	Thermal expansion of hot arm
m	Constant
q_{i-1}	Net rate of heat conduction into the element
q_{i+i}	Net rate of heat conducted out from the element to the actuator length

q_{joule}	Rate of heat generated inside the element joule heating
$q_{out, sub}$	Rate of heat conducted out to substrate
Q_{in}	Net rate of heat conduction into the element
Q_{joule}	Rate of heat generated inside the element joule heating
$Q_{out, arm}$	Net rate of heat conducted out from the element to the actuator length
$Q_{out, sub}$	Rate of heat conducted out to substrate
R	Radius of cold disc
R_T	Thermal resistance
S	Shape factor
Δt	Time between time step
t_a	Elevation of Polysilicon structure above substrate
t_n	Thickness of Silicon Nitride
t_p	Thickness of Polysilicon structure
t_{po}	Thickness of Poly0
T	Temperature
T_{avg}	Average temperature of hot arm
$\overline{T_c}$	Average temperature of cold disc
$\overline{T_h}$	Average temperature of hot arm
T_{sub}	Substrate temperature
Δu	Element volume
w	Width of hot arm and cold disc
x	Cartesian Coordinate in the actuator length direction
Δx	Distance between nodes

α	Co-efficient of thermal expansion
δ	Angle of rotation of cold disc
ϕ	Diameter of cold disc
ρ	Density
ρ_0	Resistivity at room temperature
ρ_r	Resistivity at any temperature
ξ	Temperature coefficient of resistivity
MUMPS	Multi-User MEMS Processes

Chapter 1

Introduction and Literature Review

1.1 Motivation

Breath taking innovations in Micro Electromechanical Systems (MEMS) are making way into more and more cost effective applications. The capability of sensing with sensors and providing mechanical motion in micro level with actuators can be identified as major achievement of MEMS based devices. This inspires the research effort of having fully integrated miniaturized physical systems on a same wafer that will be able to sense, take decision and act on its own. MEMS has prospective applications in optics, robotics, automobile, aerospace, bio-medical engineering that are just to name a few.

Revolution in communication technology has produced tremendous need for more functionally capable miniaturized devices and accessories because they can reduce the footprint of traditional devices while the cost could be much less. Actuator acts as a major component for integrated physical systems because of its ability to provide motions or act as a response to its environment. Such devices are the core of many optical MEMS (MOEMS) applications like switching, attenuation, diffraction etc. Among different types of actuators, thermal actuators provide larger force and deflection that are important for many applications. Numerous advantages and promising applications of actuator have inspired researchers to investigate various concepts. The present research effort is directed towards the design, analysis and development of a novel, micro thermal actuator. The thesis presents a systematic study of the concept, model development, analysis and

simulation of the model's responses, finally a prototype development for testing and validation.

The following subsections present the background studies and detail review of existing literature in order to develop a clear objective for the present investigation.

1.2 Introduction to MEMS

Success story in Integrated Circuit (IC) industry opened a new horizon for scientists to think small in order to save costly space and paved the way to have physical systems in micro dimension [1]. Miniaturized circuits performed the same function while their mass production proved to be economically cost effective. This inspired the engineers and scientists from other branches of physical science to engage in rigorous research to take advantage of miniaturization in various applications like mechanics, robotics, automobile, aerospace, fluidics, bio-medical engineering, that are just a few to name.

The term Micro Electro Mechanical Systems (MEMS) is widely used for miniaturized sensors and actuators. However, in Europe it is known as Micro System Technology (MST) while in Asia it is referred as micromachines and is referred to as Mechatronics in Japan [2]. By far, there is no single definition for MEMS. Frazier et. al. [2] referred MEMS as very small i.e. submicron to millimeter devices and systems, varying from microsensor elements and microactuators to precision mechanical components. Some scientists describe it as the integration of miniaturized sensors, actuators and signal processing units capable of sensing, taking decision and reacting.

Numerous MEMS devices have been commercialized such as micro accelerometers for air bag deployment in automotive, various micro pressure sensors, inkjet printer head, optical switches for communications, micro mirrors for projection, laser heads in CD and DVD units, read-write head in magnetic hard disks are just to name few. With increasing space constraint and objective of having higher level of performance, miniaturized devices are making their ways into more and more applications. Some of the new branches of MEMS technology with immense potential have appeared, such as micro-optoelectromechanical systems (MOEMS), BioMEMS which is MEMS in health field, RFMEMS etc. In short, the possibility is unlimited in the micro dimension.

According to Ohlckers et. al. [1] the driving factors for the development of MEMS products are as follows:

1. MEMS products have wide range of potential applications
2. Considerable development in the manufacturing infrastructure.
3. Established micromachining techniques like anisotropic, isotropic, selective etching combined with photolithography.
4. Continuing development of design and simulation tools for MEMS devices design.
5. Foundry service is already available for microelectronics industry and is evolving for Microsystems.
6. Successful research experience from solid state technology and microelectronics industry.

7. Availability of materials with good electronic and mechanical properties.

1.3 Challenges in MEMS Device Realization:

Most researchers working in this field, do not have their own fabrication facilities because of high infrastructural cost involved in establishing such facilities. Fortunately, researchers can get their devices fabricated from foundries that offer commercial service. As a result, realization of MEMS device from the phase of design to fabrication could be time consuming and expensive. Learning design errors from unsuccessful devices could prove inefficient and expensive. In order to avoid this problem, designers rely on commercial design and analysis computer aided softwares which enables them to do design and run pre-design simulation for understanding behavior of MEMS devices. Though this practice can improve the chance of success for a typical device but is not error proof. It is mainly because MEMS devices are complex by nature and their operation spans over multiple physics domain. It needs a lot of expertise on the part of the design engineer to include effects of all the physics domain in the design analysis or simulation which almost represents the real life situation. Other factors that slow down the development of MEMS devices are [1]:

1. MEMS products are still not well known to many users, and as a result they are reluctant in using this new technology.
2. MEMS products need lot of time for the development from the conception to realization stage.
3. Development of MEMS products needs lot of resources because of the complexity associated with the development stages.

4. At the conception stage some devices need special processing steps which yield higher cost.
5. Some devices need special packaging to ensure its connectivity with the working environment.
6. Integration of various MEMS components for an integrated system is still complex.
7. MEMS industry is still not matured and has limited resources.
8. Most of the products have low market penetration and the complex development yields high cost.

Despite of all the limitations MEMS industry has proved to grow successfully over the last decade.

1.4 Market Demand for MEMS devices

Over the last decade demand for MEMS devices have grown tremendously [2] and still its market share is expected to grow at a very high pace. This is attributed to the fact that typical MEMS products like sensors and actuators have immense potentials and finding new applications with time where as MEMS is evolving in new demanding fields like MOEMS, micro fluidics, biomedical engineering, aerospace etc. Though there is difference between the studies [3,4] on projected market demand, they fairly show that demand for MEMS devices will keep on growing with time. It is estimated that revenue generated by MEMS technology will rise to US \$34 billion in 2006 from that of US\$ 17 billion in 2002 while the unit consumption of MEMS/MST devices is expected to

increase to over 10 billion from approximately 3.5 billion in this period [3]. The consistency in growth can be seen from the charts presented in Figure 1.1 [3]. A comparison of MEMS/ MST usage by sector is shown in Figure 1.2 [3].

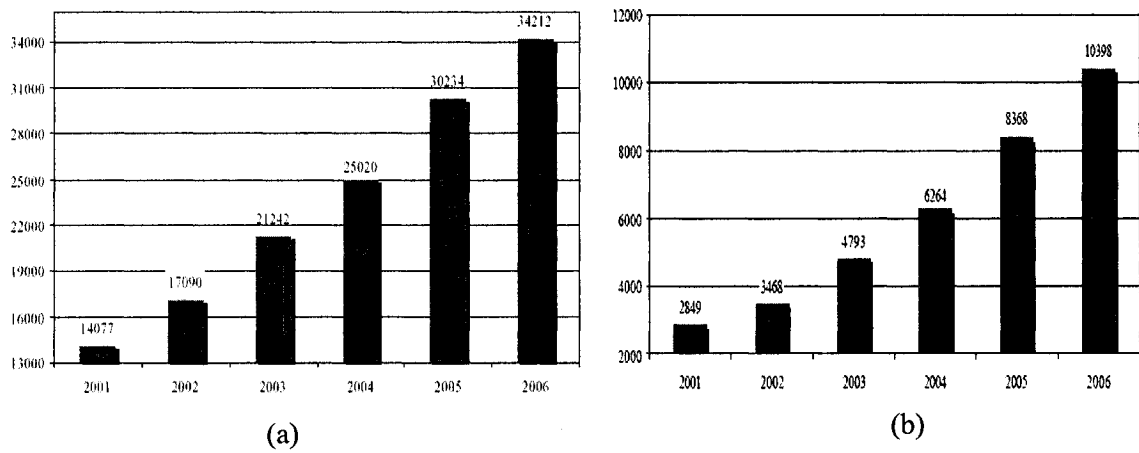


Figure 1.1: Global consumptions of MEMS/ MST devices (a) in millions of US dollars and (b) in millions of units [3]

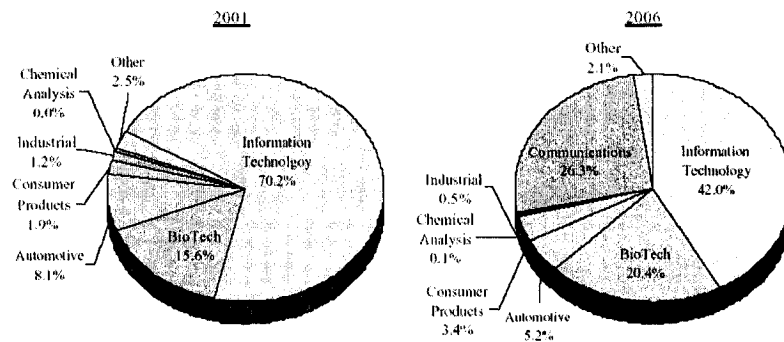


Figure 1.2: Comparison of MEMS/ MST device usage by various sectors (Percentage of total units) in 2001 and 2006 [3]

The estimation in Figure 1.2 shows that the major thrust in the MEMS demand in 2006 would arise due to rapid development in communication technology and Bio-technology.

A similar study conducted for the time period of 2004-2009, by Wicht Technologie Consulting on behalf of NEXUS (The Network of Excellence in Multifunctional Microsystems), an organ established by European Commission [4] show slightly different but similar trend for the usage of the technology. According to this study Figure 1.3 shows the product based market for various MEMS/ MST devices. The results of same study comparing trend in usage by sector is shown in Figure 1.4.

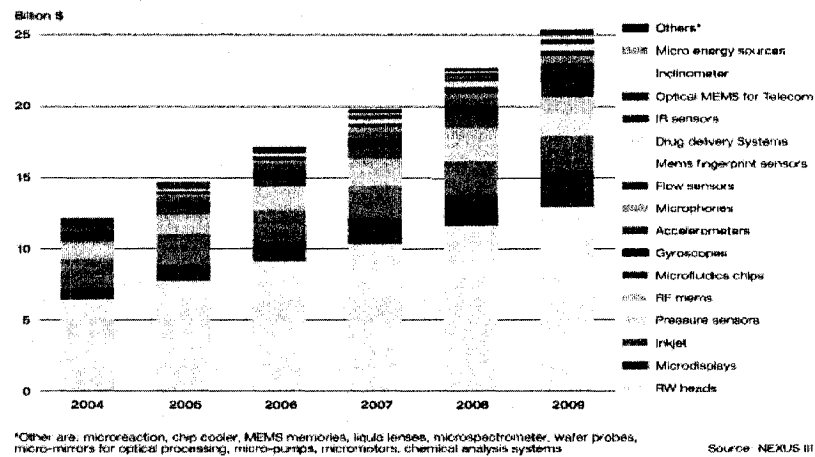


Figure 1.3: Total Market for various MEMS/ MST Products for the period of 2000-2009 [4]

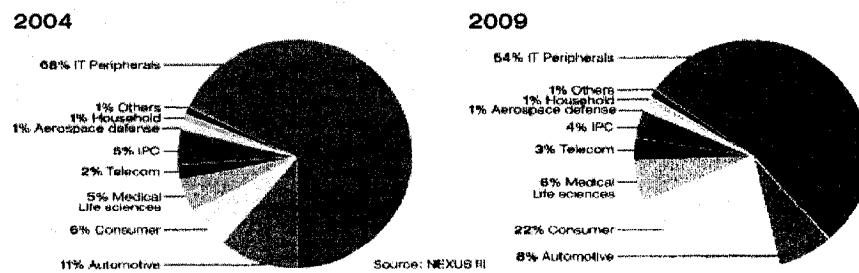


Figure 1.4: Comparison of MEMS/ MST device usage by various sectors (Percentage of total units) in 2004 and 2009 [4]

1.5 Actuators for MEMS application

Microactuators provide the driving force for physical system in micro level. Typical applications of MEMS actuators are: switching, attenuation and diffraction in various optical applications, actuation of micropumps, micromotor, scanning micromirrors etc. Depending on actuation principle different actuation solutions are available in micro dimensions such as, electrostatic, thermal, magnetic and piezoelectric actuation etc. Among these, electrostatic and thermal actuators are the most popular ones. Various concepts for microactuation along with their known advantages and disadvantages are presented in the following subsections.

1.5.1 Electrostatic Actuator

The operating principle of an electrostatic actuator is similar to that of a parallel plate capacitor. When a bias voltage is applied between two electrodes separated by dielectric medium, opposite charges accumulate on the electrodes which provide an electrostatic force and this force in turns will provide the required actuation. A schematic diagram of this arrangement is shown in Figure 1.5. The force developed by this mechanism is proportional to the applied voltage and the distance between the two plates. A good advantage of this actuator is that it has very good repeatability which is very important for precise applications like scanning micro mirrors and optical switching.

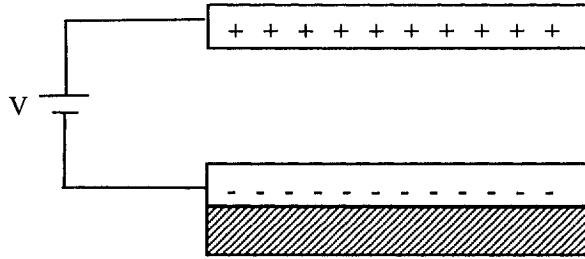


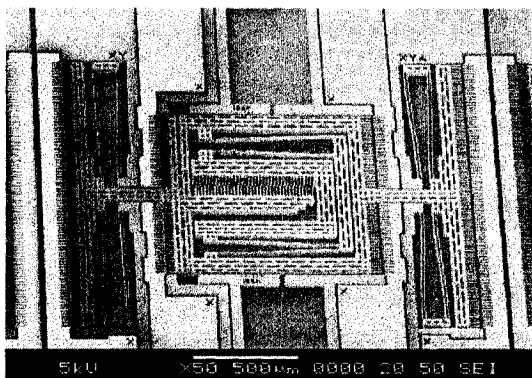
Figure 1.5: Schematic diagram of the operating principle of an electrostatic microactuator

The electrostatic force, F_d generated by applying a voltage can be given by,

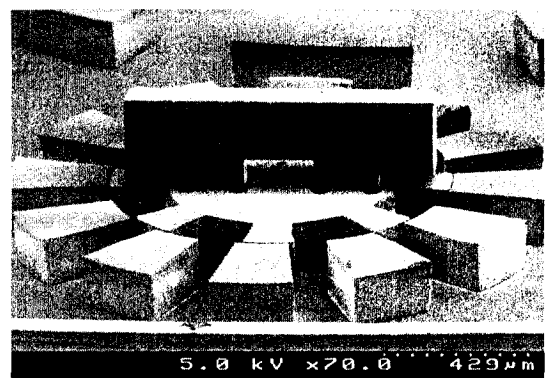
$$F_d = \frac{\partial U}{\partial d} \quad (1.1)$$

where, V is the applied voltage, d is the distance between two plates, U is the energy stored in the two-plate capacitor which is equal to $\frac{CV^2}{2}$, where C is the capacitance.

Disadvantages of an electrostatic actuator include nonlinearity in force vs. voltage relationship, hysteresis and high driving voltage requirement for larger force output. In the following, There are examples of this concept utilized in practical applications. Designs for electrostatic actuator [5] and rotary electrostatic micro motor [6] are shown in Figure 1.6(a) and Figure 1.6(b), respectively.



(a)



(b)

Figure 1.6: (a) Two dimensional electrostatic actuator [5] and (b) a rotary electrostatic micro motor [6].

Other examples where this concept for actuation is used is shown in Figure 1.7. Figure 1.7(a) shows DLD™ developed by Texas Instruments that uses electrostatic actuation principle. Figure 1.7(b) shows a linear electrostatic actuator used in an optical switch [7].

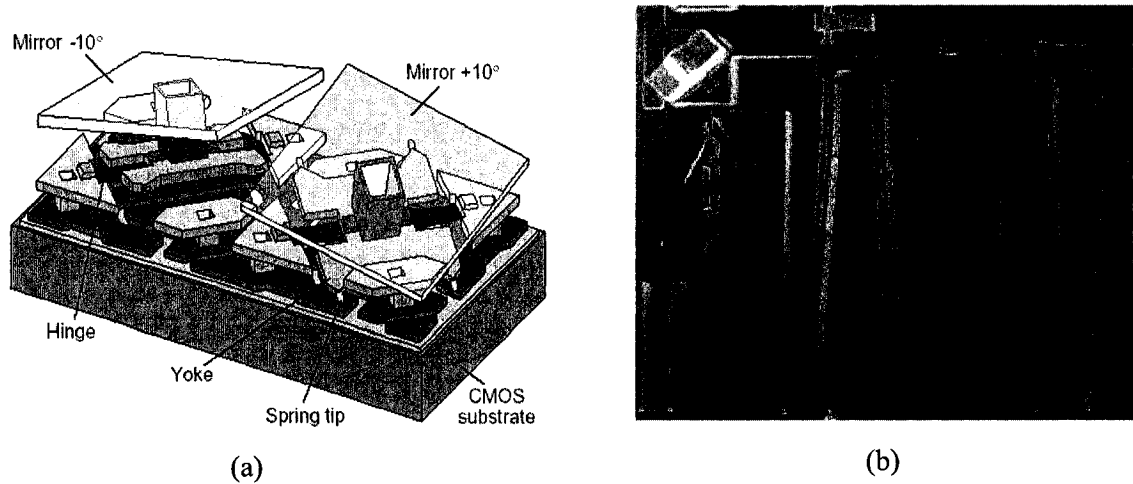


Figure 1.7: (a) DLD™ (developed by Texas Instruments) and (b) linear electrostatic actuator used in an optical switch [7].

1.5.2 Electro Magnetic Actuator

Attraction between electromagnets with different polarity provides the required actuation force for this type of actuator. At low drive voltages it can generate large forces with high linearity. As, disadvantages, it needs shield from other magnetic devices for avoiding induction, lacks proven reliability and needs further development in fabrication process.

1.5.3 Piezoelectric Actuator

This type of actuator operates on the inverse piezoelectric effect i.e. a piezoelectric material is deformed under the application of voltage. Though this type of actuator may provide large force, the main disadvantages of this are that piezoelectric material is

sensitive to temperature variation and it needs further development in fabrication process to prove its potential.

Since thermal actuation is the focus of the present investigation, a detailed review of literature on its state of art is presented in the following.

1.6 Literature review

Before the review done by Kurt Peterson [8] in 1982, application of Silicon was primarily considered to be as electronic material for use in Integrated Circuit (IC). He reviewed the applicability of silicon for mechanical structures. Howe et. al. [9] first fabricated micro cantilever and doubly supported mechanical beams from polycrystalline silicon film using MOS planar process. They also evaluated the structures for their static mechanical properties. The study examined the dependences of maximum free standing length and beam deflection on the thickness of the beam and concluded that such fabrication methodology can be successfully used for fabricating micro mechanical components. This inspiration led to the fabrication of a chemical vapor sensor [10], which can be regarded as the first integrated MEMS device. Since then fabrication technology has seen a lot of developments to arrive at the present state of MEMS devices.

As stated earlier, actuator is very important part of any integrated system that is able to sense and respond. Micro actuators have received special attention in MOEMS for various applications like alignment, switching, diffraction, attenuation etc. There are various actuation mechanisms. Among them Electrostatic and electro thermal actuators

have gained the most popularity. Guckel et. al. [11] pioneered among some of the earliest works on thermal actuator and investigated thermo-magnetic metal flexure actuator. They studied magnetic and thermal effects on the actuation of a metallic flexure (beam) actuator. In the modeling, only conduction through the beam and to the substrate was considered while free convection and radiation were neglected. Their work inspired tremendous effort of research work on the design of electro thermal actuator. Comtois and Bright pioneered on electro thermal actuators [12]. They provided generic design and various assembly techniques for the actuators fabricated utilising surface micro machining [13]. Comtois et. al. [14] provided the design guidelines for maximizing motion and modeling of a typical electro thermal actuator. They also showed applications of electro thermal actuation principle in various design topologies, along with actuator arrays. Comtois and Bright [15] showed application of actuator and their arrays in various optical applications. These actuators provide design directions for compact and powerful devices, low-voltage micro-positioners and self assembling hinges. Self assembly techniques enable flexibility of assembling even after packaging instead of complex manual assembly. Butler et. al. [16] used CMOS compatible actuator arrays for positioning surface micromachined scanning and rotating micromirrors. A computer based digital pulsed control system was developed for the precise positioning of the mirrors. Lerch et. al. [17] fabricated a microgripper using Laser microfabrication. This microgripper is a modified topology of an electro thermal flexure actuator.

Reid et. al. [18] have designed and fabricated a force tester. It was used to measure the force produced by a micro actuator for various design parameters including flexure

length, hot arm width, arm separation and actuator thickness. They showed that an array of actuators combines the force produced by individual actuators. Comtois et. al. [19] experimented on various actuators and their arrays for the study of their performance characteristics like force and deflection with respect to input power and operating frequency. They also observed the effect of long term usage. Based on the dynamic response of the actuators, their operating frequencies were determined. The experimental results assisted them in setting guidelines for selecting proper actuator and configure their arrays while matching the force requirements of various applications. The actuators were fabricated in SUMMiT (Sandia ultra-planar multi-level MEMS technology) [20], which is a four-layer surface micromachined polysilicon process. Performance characteristics of any actuator fabricated by this method, is applicable to actuators fabricated by other surface micromachined polysilicon processes.

Butler et. al. [21] reported on the modeling of lateral actuator and piston micro-mirrors. Both empirical and parametric (finite difference model) methods were used in SPICE. For positioning of the actuators both pulse width and pulse amplitude modulation were used while the period of pulse width were ensured to be much less than the thermal time constant of the actuator. Butler and Bright [22] too used parametric method for the performance study of actuator in SPICE. Proper characterization of resistivity is very important for any actuator study and for this they used empirical resistance measurements and TSUPREM process simulation. Kolesar et. al. [23] characterized in-plane electro thermal flexure actuator by finite element analysis and experimental results. They also showed an alternative method of measuring force by having a narrow cantilever beam in

parallel to the hot and cold arm. Burns and Bright [24] and Kolesar et. al. [25] did a comparative study between single and double hot-arm asymmetrical polysilicon surface micromachined flexure electro thermal microactuators. Having another hot arm reduces parasitic resistance of the cold arm and improves electrical efficiency. In this new topology, since cold arm does not work as current return path, so it can afford to have narrower flexure. A comparison between single and double hot arm shows that latter have more deflection for the same applied load.

Li and Ananthasuresh [26] investigated various Electro-Thermal-Compliant (ETC) micro devices which work on embedded actuation. In this actuation the mechanism and the actuator are indistinguishable. They developed a bulk micromachining process called PennSOIL and fabricated devices using this. They combined PennSOIL with excimer laser micromachining to reduce processing time and to modify the cross-section of the fabricated devices. Testing was done to characterize the process and the resulting material property. Moulton and Ananthasuresh [27] performed analysis on ETC building blocks. Selective doping of ETC increased non-uniform heating and thus the deformation.

Pan and Hsu [28] proposed a new topology for lateral electro thermal actuator. In this topology the actuator consisted of two beams with different lengths but of same cross sectional area. Due to the differential temperature generated in the two beams, asymmetrical thermal expansion takes place. This actuator has potential application in microswitches, optical tweezers and micropositioners. This actuator was used as

microgripper with the benefit of small feature size while offering large working distance and gripping force. They performed analysis of the actuator using commercial finite element package, ANSYS. They considered conduction heat transfer through the structure to the anchor as the major mode of heat transfer and neglected convection, conduction and radiation heat transfer to the surrounding. Lee and Hsu [29] proposed a new topology for microactuator which can be considered to be a combination of that proposed by Guckel et. al. [11] and Pan et. al. [28]. In this topology the actuator has two beams with different lengths and variable cross sectional areas. They performed optimization on the proposed design. It was found from the finite element analysis and experimental results that the proposed design perform better than that of [11] and [28]. When the air gap below the structure is small (2 microns), conduction heat transfer through the air to the substrate was considered. On the other hand convection transfer was considered when the air gap was considerably high (300 microns).

Mankame and Ananthasuresh [30 and 31] conducted a comprehensive analysis on a bulk micromachined silicon electro thermal actuator. They showed the importance of selecting appropriate thermal boundary conditions like radiation, convection and thermal grounding of the anchor which are specific to different fabrication process. They considered convection as dominant mode of heat transfer which was validated with experimental results and this can be attributed to the fact that their devices were suspended 20 microns above a silicon substrate. They also studied the effect of variation of heat transfer co-efficient. Their analysis included the effect of variation of thermo-physical property.

Lin and Chiao [32] performed electro-thermal analysis on polysilicon line shaped microstructure fabricated by surface micromachining. According to them, it is very important to properly model the heat transfer from the structure to the environment. They determined an empirical relationship for a shape factor, which accounts for the heat conduction from the line shaped microstructure to the silicon substrate. They assumed that at low operating temperature, convection and radiation heat terms can be neglected. They also concluded that shape factors are to be found on a case by case basis and that there is no general expression for different shape of structures and different surrounding fluids.

Hickey [33] performed extensive analysis on a surface micro machined and conventional U shaped electro thermal actuator in varying ambient conditions. He performed CFD analysis to determine the major heat transfer modes involved in the operation of a typical thermal microactuator fabricated by surface micromachining. His findings conformed with Lin and Chiao [32] establishing that lateral conduction through the structure to anchor and vertical conduction through the low air gap (2 microns) to the substrate are the major modes of heat transfer. He provided analytical model for the electro thermal and deflection analysis of the microactuator. He used a convective heat transfer coefficient to account for the conduction heat transfer through the air to the substrate. He also performed finite element modeling on the actuator and suggested in having air volume around the structure. He has outlined guidelines for design optimization with a trial and error approach. He also conducted dynamic testing and simulation of the actuator to characterize its response frequency. Hickey et. al. [34] presented the modeling

of U shaped and chevron actuators along with the equations for thermal time constants and frequency responses.

Huang and Lee [35] developed an analytical model to characterize temperature and deflection of an actuator made of two beams with same cross sectional area but different lengths. They only considered conduction through the structure and neglected the other modes of heat transfer. As an extension of their previous work, Huang and Lee [36] developed an analytical model to characterize temperature and deflection of a conventional micro electro thermal actuator consisting of two beams with same length but variable cross sectional area. The actuator was fabricated by polysilicon surface micromachining. The model assumes one dimensional heat transfer analysis with due consideration of heat lost to the substrate incorporating the shape factor. Heat conduction through the structure to the anchor was assumed to be the major heat transfer in the model. Convection was considered to be negligible and for the safe mode of operation of the thermal actuator radiation heat transfer to the ambient was neglected. It was also shown that the radiation heat transfer could be significant at higher operating power. The model can not incorporate temperature dependent properties except for resistivity. Huang and Lee [37] provided analytical model for computing the driving force for a polysilicon lateral electro thermal actuator.

Lott et. al. [38 & 39] conducted electro-thermo-mechanical analysis on a chevron shaped surface micromachined in plane microactuator and developed a finite difference model for doing so. This model can incorporate temperature dependent properties for analysis

purpose and the model was used for simulation of performance of the device in both air and vacuum. Validating the deflection data with that of the finite difference model, they suggested that temperature dependency of thermal conductivity of polysilicon and air, should be taken into consideration for better modeling.

Yan et. al. [40] used a lumped model for predicting the behavior of a two-hot arm thermal actuator and validated the model from the results obtained from finite element analysis and experiments. They considered lateral and vertical conduction are the major heat transfer modes involved in the operation of the actuator. Yan et. al. [41] designed a new thermal actuator which provides bidirectional vertical motion. This design concept eliminates the need of wider cold arm by interconnecting two U shaped beams located in different planes. This design thus eliminates parasitic resistance associated with cold arm and provides improved electrical efficiency because of the active current return path. For the analysis of the actuator they adopted the lumped model of their previous work [40].

Li et. al. [42] conducted a study on the impact of hot arm geometry on the temperature distribution and a dimensionless thermal parameter which determines the temperature distribution. Based on this finding they improved performance of a conventional U shaped electro thermal actuator by changing the dimension for a section located in the middle of the hot arm. Increased width of this section has proved to help in achieving a higher average temperature of the hot arm while maintaining a lower peak temperature. Increased average temperature results in more deflection while the lower peak

temperature reduces the possibility of thermal failure (melting down) and increases operation limit of a microactuator.

Luo et. al. [43] performed a comprehensive analysis on the advantages of a metal based actuator over the Si based actuator. They found that a lateral actuator made of Ni provides about 60% more deflection than Si based actuator. They modeled the thermal and deflection behavior of actuator and from the model showed that the deflection of a typical microactuator solely depends on the material properties. Properties of metal enable a metallic actuator to provide relatively large deflection and force for a low operating temperature and power consumption.

As evident from literature review, electro thermal actuators have attracted a lot of interest among micro system researchers. However, the focus so far has been towards linear actuators. Same concept can be applied to rotary actuation with many potential applications. The present research is thus directed towards realizing rotary motion actuator based on electro thermal concept.

1.7 Thesis Objective

The objective of this thesis is to design an electro thermal actuator that provides rotary motion of the cold disc. This thesis aims at examining the effects of various design topologies on rotational behavior. The thesis also aims at providing various models i.e, analytical, finite difference and finite element, for the electro thermal and rotational analysis of the actuator. Results obtained through the simulation of various models help

in designing actuator for required rotation. Finally this thesis presents the feasibility of the rotary type actuator through experiment.

1.8 Thesis Contribution

This thesis makes the following contributions-

1. Provides various design topologies for rotary type micro thermal actuator. The thesis also provides various models i.e., Analytical, Finite Difference Method (FDM) and Finite Element for the purpose of analyzing this actuator. All these models can be used for predicting steady state behavior of the actuator. In addition, FDM can be used for transient analysis of the actuator. This method can be used to include temperature dependency of various parameters like thermal conductivity, resistivity and specific heat of polysilicon and thermal conductivity of the air. The results obtained from the various models are found to be close and the results help in choosing dimensions of the actuator for required rotation. They also help in determining the operating voltage range for the actuator.
2. The thesis determined the effect of various design topologies on the rotary motion of the cold disc. It also determined the effect of beam and disc dimensions on the performance of the actuator.
3. Finally the thesis provided a scheme for the experimental procedures and of results. The experimental results establish the feasibility of the novel actuator for various optical applications.

1.9 Thesis Overview

Chapter 1: justifies the motivation of this thesis work and introduces previous research works on various electro thermal actuators. Also included are introduction to MEMS, challenges in MEMS device realization, market demand for MEMS products and a brief discussion about other actuation mechanisms in micro level.

Chapter 2: gives a brief description on various micromachining techniques and working principle of a typical micro electro thermal actuator. This chapter shows variation in the topology that effects the behavior of an actuator. Also included are the proposed design topologies for novel rotary type micro thermal actuators.

Chapter 3: details analytical, finite difference and finite element modeling of the proposed actuator for the purpose of its characterization and performance studies. The models are compared for the purpose of validation. A parametric analysis is also included.

Chapter 4: details the setup used for the purpose of experimentation of the novel rotary actuator. This chapter compares the experiment results with that from the models detailed in Chapter 3.

Chapter 5: provides conclusion and highlights the findings of this thesis. Also given is recommendation for future work.

Chapter 2

Micromachining and Proposed Design for Rotary Type Micro Thermal Actuator

2.1 Micromachining Techniques

The MEMS devices are realized on wafer level through microfabrication. Factors that determine the applicability of any microfabrication process are: its capability to miniaturize, desired electro-mechanical properties of the structural layer, compatibility with IC fabrication technology and cost effectiveness. The most popular micro machining methods are: bulk micromachining, surface micromachining, LIGA etc.

2.1.1 Bulk Micromachining

The bulk micromachining is one of the most popular micromachining techniques. In this method, selective etching is done on the silicon substrate to realize MEMS devices. Since, this method allows removal of significant amount of material, high aspect ratio for micromechanical components can be achieved. Direction of etching is determined by the crystallographic orientation of the wafer. Some of the popular anisotropic etchants are Potassium Hydroxide (KOH), Tetramethyl-Ammonium Hydroxide (TMAH) and Ethylenediamine–Pyrocatechol (EDP). Figure 2.1 shows cross section of a bulk micromachined membrane that is integrated with bipolar electronics [46].

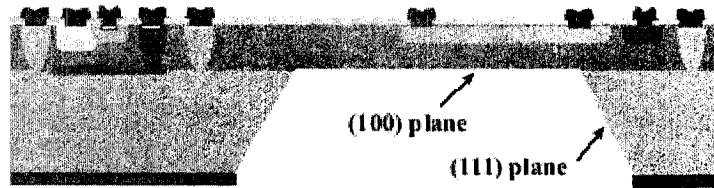


Figure 2.1: Cross section of bulk micromachined membrane integrated with bipolar electronics [46]

2.1.2 Surface Micromachining

Figure 2.2 in the following shows schematic diagram of processes involved in surface micromachining [46].

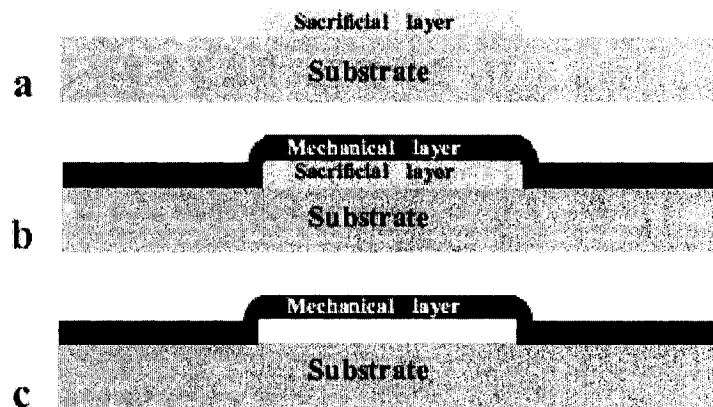


Figure 2.2: Schematic diagram of processes involved in surface micromachining [46]

Surface micromachining can also be called sacrificial micromachining. In this process, thin layers are deposited on to silicon substrate and structures are realized in selective layers. Layers could be of two type, namely structural layer and sacrificial layer. Structural layer is used for making mechanical structures, etching is done on this layer and sacrificial layer is used as handle in between structural layers. At the end of the process, sacrificial layer is removed and the MEMS structure is released. Lift-off Process is an another example of surface micromachining used to pattern metallic films. In this

method, metals are allowed to adhere to the substrate only in the desired region. Using a negative mask metal of the desired region is exposed. The edges of the mask are undercut which facilitates discontinuous metal region on the substrate and on the mask to be formed. The unwanted metal is lifted off when the sacrificial mask is dissolved away. Multi User MEMS Process (MUMPS) [47] is a highly popular yet cost effective surface micromachining processes developed by Cronos Integrated Microsystems. This method is used to manufacture the prototype rotary thermal actuators in this investigation, and is described in Appendix [A].

2.2 Working Principle of Electro Thermal Actuator

The operating principle of a lateral/ in plane thermal actuator is the asymmetrical thermal expansion of the actuator with variable cross sectional area. While designing a micro thermal actuator, a suitable fabrication process is selected which uses resistive material for structure. Narrower section has higher resistance to current flow than wider section. Upon application of potential difference, the narrower section is heated more due to more dissipation of power in narrower section than the wider section and thus expands more than the wider section. This causes a typical thermal actuator to move. The narrower section is called hot arm and the wider section is called cold arm. A schematic of traditional in plane micro electro mechanical thermal actuator is shown in Figure 2.3.

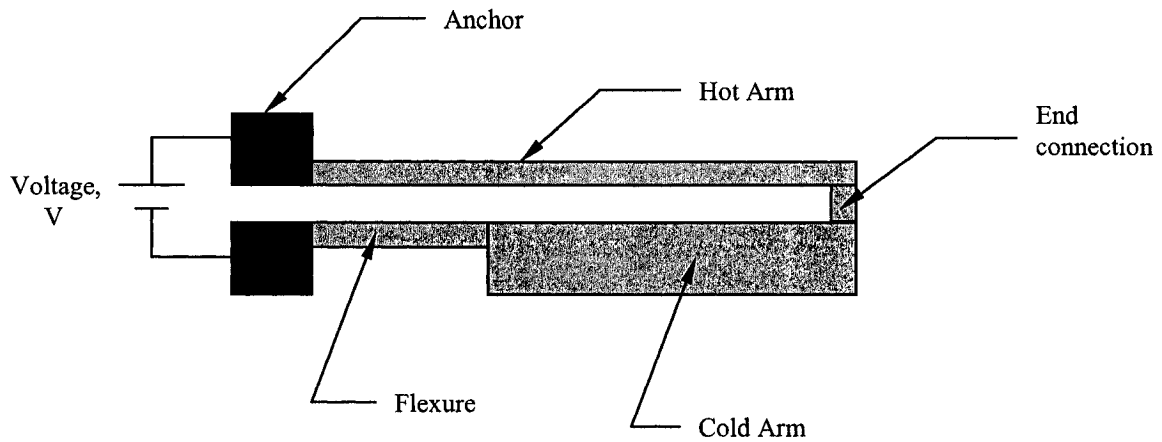


Figure 2.3: A schematic of traditional in plane micro electro thermal actuator

2.3 Design Variations in Electro Thermal Actuator

Behavior of a micro electro thermal actuator depends largely on its structural topology. Relative arrangements of various sections of an asymmetrical thermal actuator, namely, hotter section and colder section determine the direction of motion and the amount of deflection and force that will be produced. For designing a new actuator, it is of importance to study the effect of existing structural topologies on the behavior of actuators.

Dong Yan et. al. [40] showed that by having another narrow beam, more force and deflection can be produced by traditional lateral electro thermal actuator. This topology is shown in Figure 2.4.



Figure 2.4: Two arm horizontal micro thermal actuator [40]

Comtois et. al. [15] proposed a new vertical electro-thermal actuator shown in Figure 2.5. In this topology, the hot arm is arranged to be on top of the cold arm. As a result it deflects downward when current passes through it.

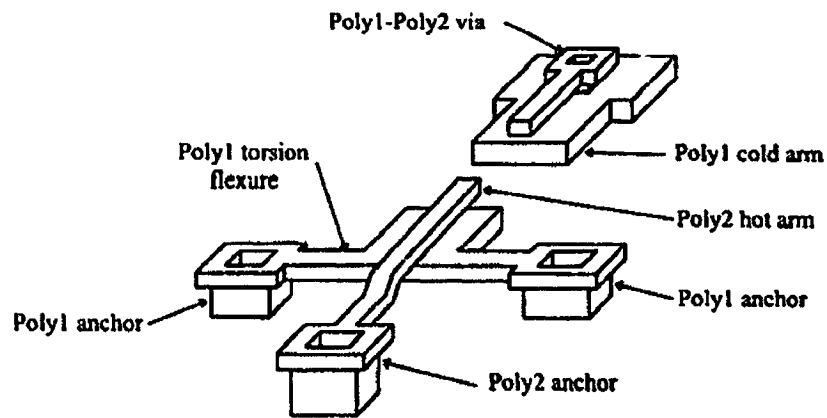


Figure 2.5: Vertical electro-thermal actuator [15]

Yan et. al. [41] proposed another topology for electro thermal actuator for vertical motions. The design as shown in Figure 2.6 is realized by using two U-shaped beam attached to its separate anchors and are in two different planes. This eliminates the need for wider cold arm, and can be made to bend upward and downward by simply selecting the layer to be changed.

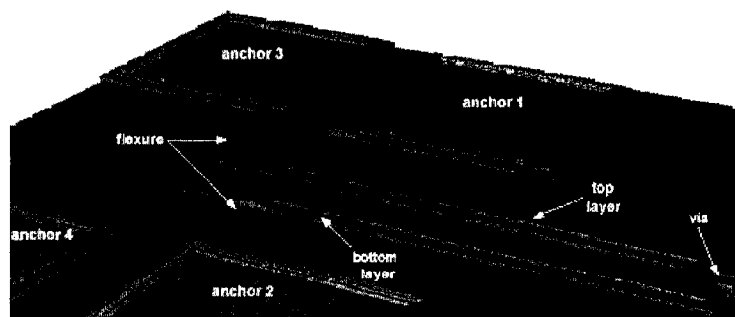


Figure 2.6: Vertical electro-thermal actuator [41]

Having longer hot arm gives more deflection but this is limited by the fact that the increased length also increases electrical resistance and chance of device failure due to stiction. Comtois et. al. [14] showed that arranging thermal actuators in array by means of flexible yoke gives magnified force and motion in one direction. Arrays of thermal actuator in this design are shown in Figure 2.7.

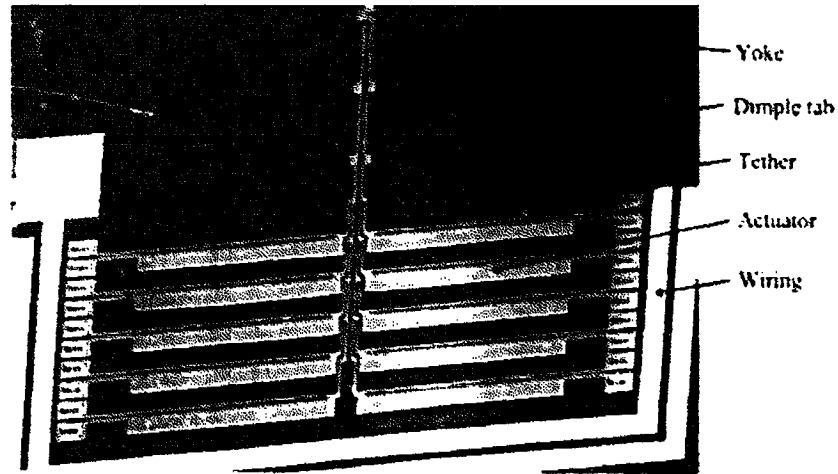


Figure 2.7: Arrays of thermal actuators tethered with a flexible yoke [14]

By arranging two opposite hot arms at a small angle with respect to each other, Chevron type of thermal actuators can be designed [34, 38 and 39]. Chevron Actuators produce less deflection, but more force. A typical Chevron actuator is shown in Figure 2.8, which was an array of arms in order to increase the magnitude of the force produced.

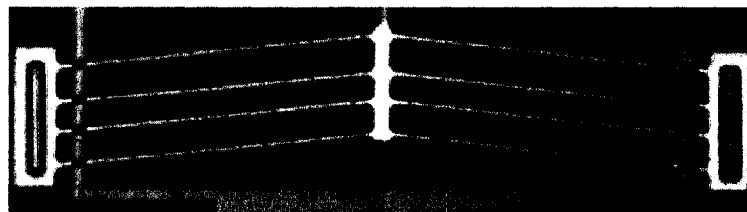


Figure 2.8: Chevron type micro thermal actuator [34]

2.4 Proposed Design for Rotary Type Micro Electro Thermal Actuator

For a micro electro thermal actuator, property of the material which is used for fabricating structure is very important. For the proposed design, Multi User MEMS Process (MUMPS) fabrication technology is chosen because of its high reliability and the fact that the technology is well established. Furthermore, material property of Polysilicon structural layers offers advantage for the operation of electro thermal actuator.

This thesis presents a novel rotary type micro electro thermal actuator with new structural topology. This actuator too has variable cross sectional area therefore it operates on asymmetrical thermal expansion. The proposed actuator presented in Figure 2.9 has a wider section called cold disc at the center which acts as a sink or cold segment. The disc is attached to the anchors through highly flexural curved beams, called hot arms or hot segments.

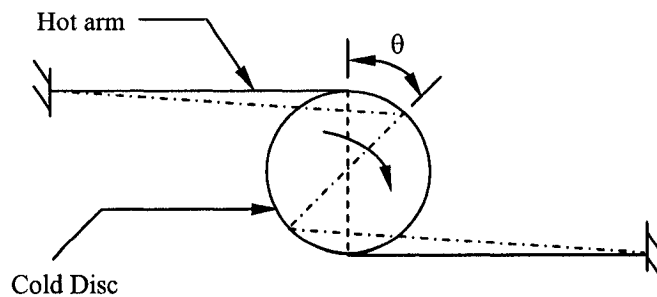


Figure 2.9: Schematic of rotary type micro thermal actuator. Various segments of the actuator are represented by line shape.

In this design, hot arms are arranged around the cold disc in such a way that the cold disc acts as moment arm for the expansion in the hot arms. This unique arrangement causes rotary motion of the disc upon application of voltage. Furthermore, the symmetric

distribution of hot arms around the cold disc, makes the device structurally stable and stronger. Both the hot arms and cold disc can be made from the same polysilicon layer of MUMPS process.

Both square and circular shaped cold disc have been used in the proposed design. Square shaped actuator features straight beams. In the circular disc shaped actuator, use of both straight and curved beam have also been proposed. Based on topology the designs can be categorized into the followings:

- Design (1): contains square disc and straight beams. Both two arm and four arm Designs are considered. Their schematics are shown in Figure 2.10. Two arm actuator is called as Design (1a) and four arm actuator is called as Design (1b). Although two arm as shown in Figure 2.10(a) can provide the functionality for rotary actuator, four arm as shown in Figure 2.10(b) is expected to provide improved structural stability.

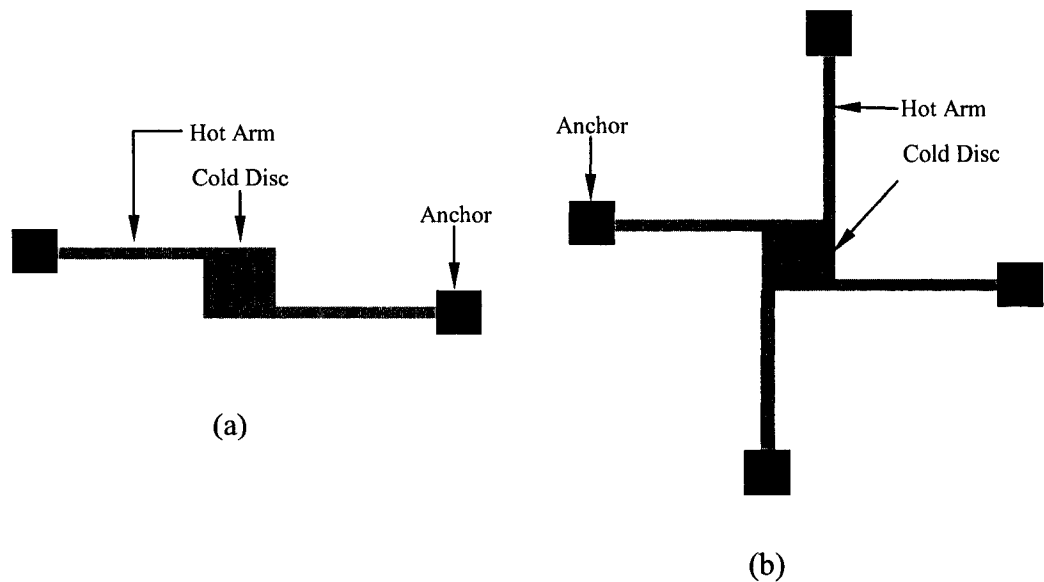


Figure 2.10: Schematics of square disc rotary actuator with: (a) two arms; (b) four arms

- Design (2): Utilizes a circular disc and four straight beams for arms as shown in Figure 2.11 (a). This design considers smaller disc in order to incorporate larger arm lengths.

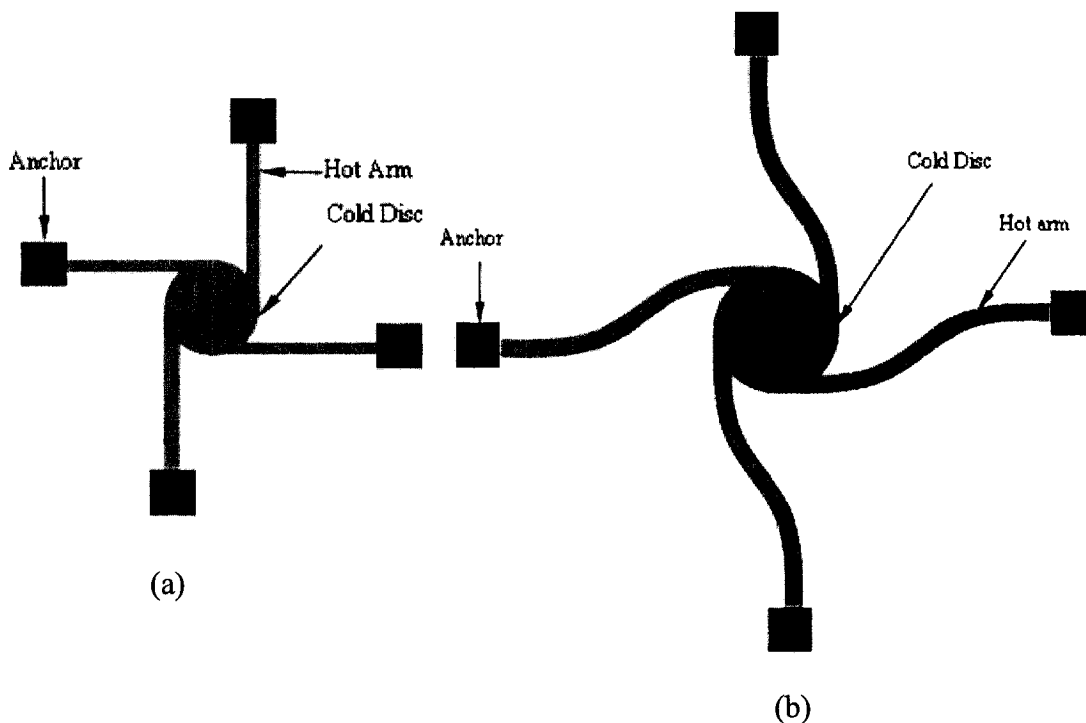


Figure 2.11: Schematics of circular disc rotary actuator with: (a) straight arm; (b) curved arms

- Design (3): Contains larger circular disc with four arms designed as curved beams. As shown in Figure 2.11 (b), this design can accommodate significantly larger arms length in a given foot-print in order to realize larger rotational motion.

Each of these designs are modeled and simulated to examine their temperature and motion performances. Detailed modeling and parametric analysis are presented in

Chapter 3. Based on the analysis and previous experiences, dimensional for each of these designs were selected as presented in Table 2.1.

Table 2.1: Dimensional parameters for the proposed designs

Dimension type	Design (1a) and (1b)	Design (2)	Design (3)
Length of each beam (μm)	250	250	732*
Width of each beam (μm)	3	3	3
Length of square disc (μm)	40	-	-
Radius of circular disc (μm)	-	25	250

* It should be noted that in case of Design (3), the length of the beam represents arc length of the curved beams.

Based on the proposed design and dimensions, a layout was formulated to accommodate several of these actuators on a $4750 \times 4750 \mu\text{m}$ chip dimension. The final layout for fabrication is carried out using MEMS design packages, and MEMS Pro and CADENCE. Figure 2.12 presents an enlarged view of the layout with several rotary type micro thermal actuators.

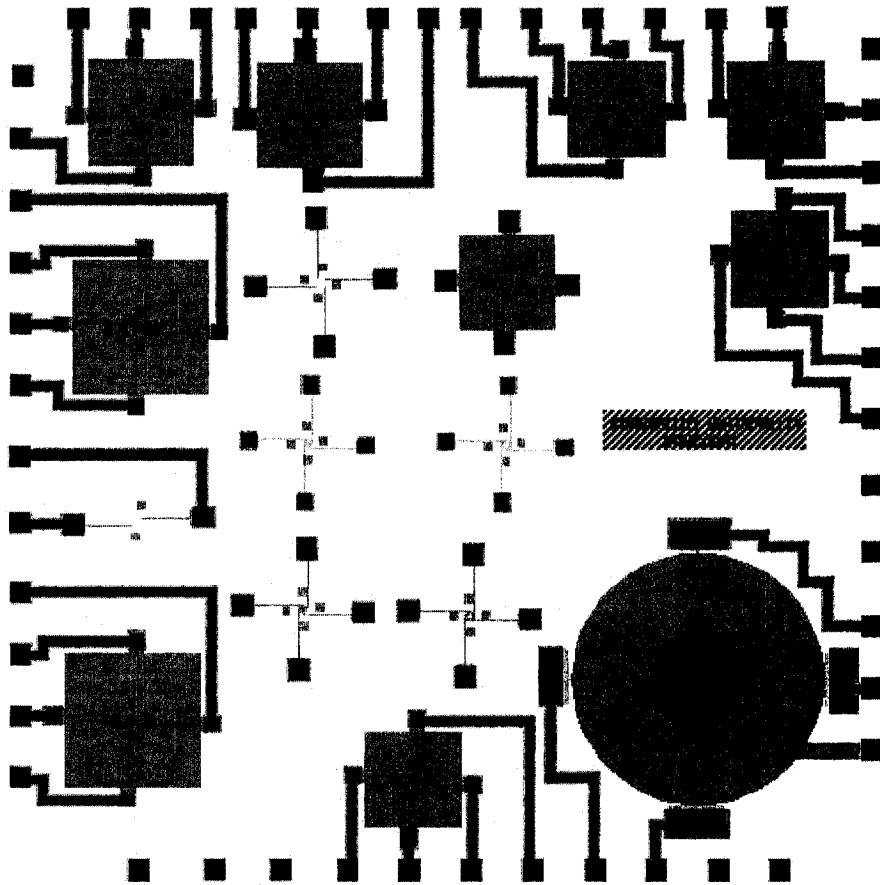
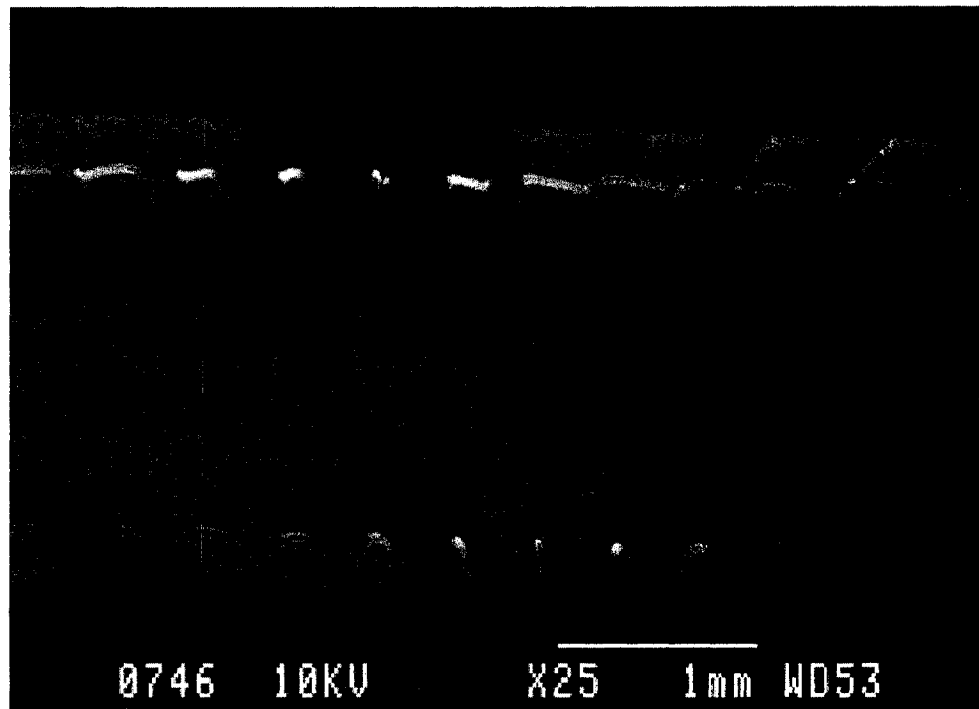


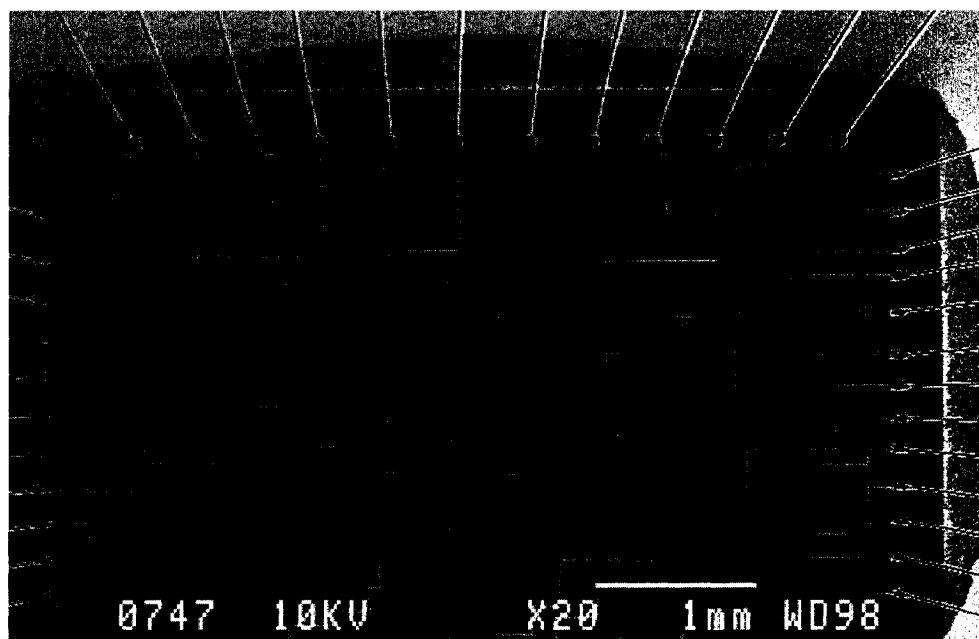
Figure 2.12: Layout diagram of the chip containing rotary type micro thermal actuator

As discussed earlier, the chip was fabricated in MUMPS technology. The fabrication was carried out by Canadian Microelectronics Corporation (CMC). Scanning Electron Micrograph (SEM) of the fabricated chip is shown in Figure 2.13.

Scanning Electron Micrograph (SEM) of the chip containing novel rotary type micro thermal actuators is shown in the following-



(a)



(b)

Figure 2.13: (a) & (b) Scanning Electron Micrograph (SEM) of the chip containing rotary type micro thermal actuator fabricated in MUMPS technology

All the devices are fabricated from single layer, Polysilicon1 by MUMPS technology. The process is described in more details in the Appendix A. Close up views of Design (1a) by SEM is shown in Figure 2.14. The fabricated square actuator with four arm (Design (1b)) is shown in Figure 2.15. It should be noted that the square disc in these views do not appear square due to their perspective from an angle.

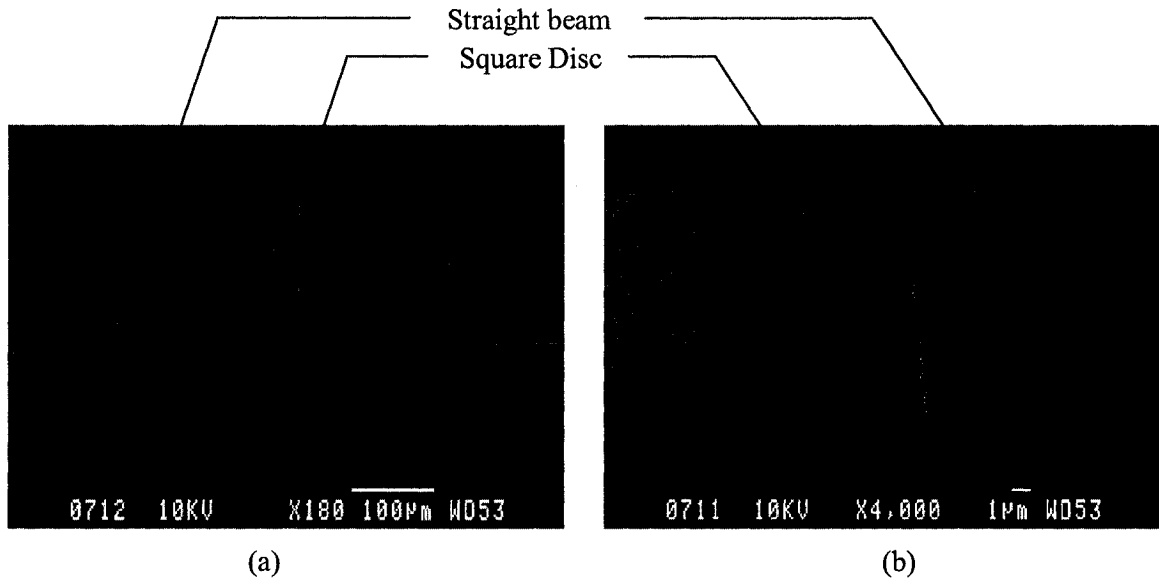


Figure 2.14: (a) Scanning Electron Micrograph (SEM) of Design (1a) & (b): Close up SEM of the square cold disc of Design (1a)

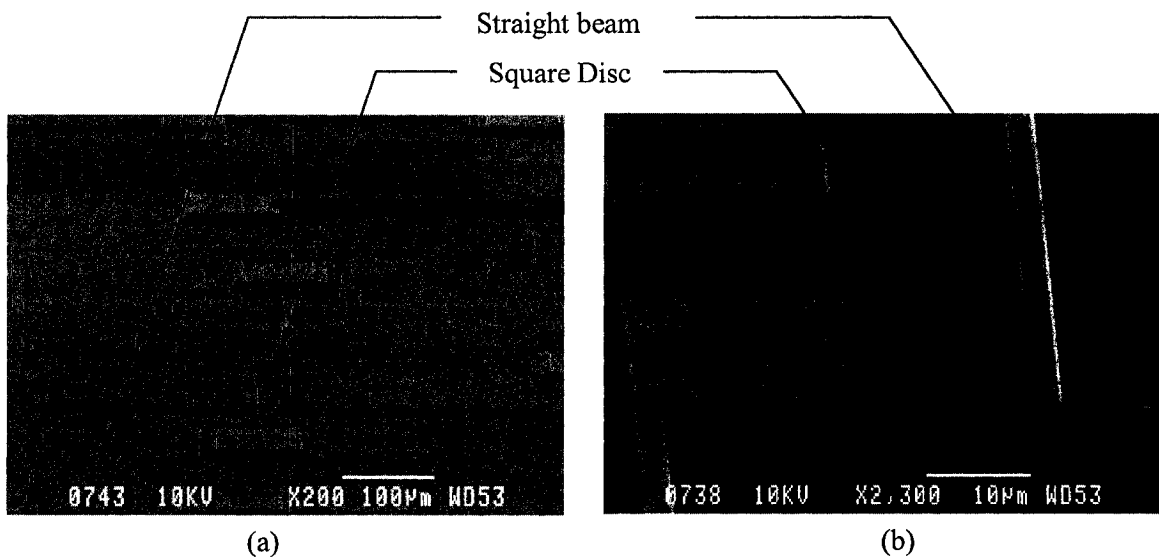


Figure 2.15: (a) Scanning Electron Micrograph (SEM) of Design (1b) & (b): Close up SEM of the square cold disc of Design (1b)

The SEMS of circular designs fabricated in MUMPS technology is shown in Figures 2.16 and 2.17. Design (2) containing straight beam arms, is shown in Figure 2.16 with x180 and x2300 magnifications.

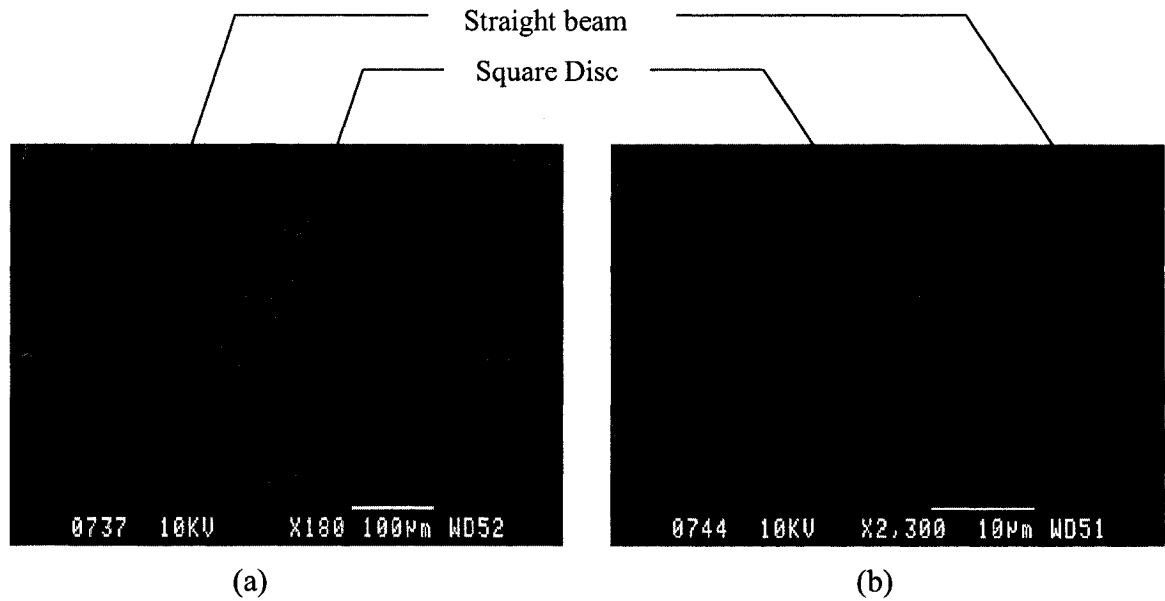


Figure 2.16: (a) Scanning Electron Micrograph (SEM) of Design (2) & (b): Close up SEM of the cold disc of Design (2)

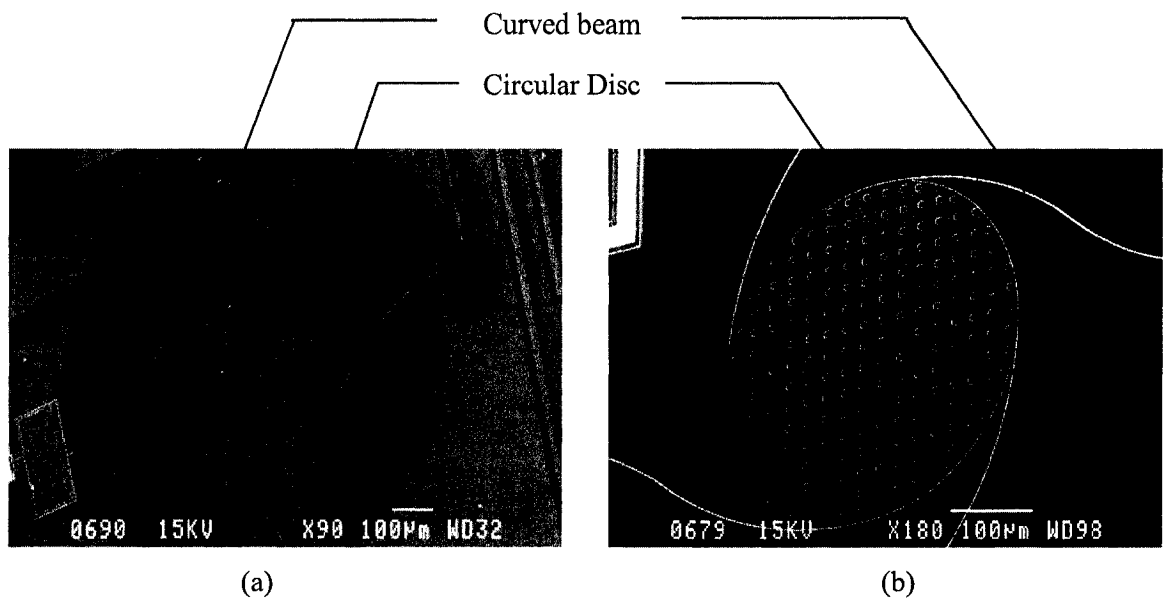


Figure 2.17: (a) Scanning Electron Micrograph (SEM) of Design (3) & (b): Close up SEM of the cold disc of Design (3)

2.5 Summary

Different micromachining techniques used in fabrication of MEMS devices are discussed. The Multi-User MEMS Processes (MUMPS) adapted for this investigation is the most cost effective and widely used process for micromachining. The chapter also discussed working principle of electro thermal actuators. Some design variations used in the past are outlined. Some possible designs of rotary type micro thermal actuators are presented in detail. A layout of the chip was designed for fabrication of the proposed actuators. The fabricated actuators and their close up views are also presented in this chapter. The geometric dimensions for these designs were based on the detailed analysis presented in the following chapter.

Chapter 3

Modeling of Rotary Type Micro Thermal Actuator and Parametric Analysis

3.1 Electro Thermal Analysis

In order to evaluate each of the designs presented in this investigation to realize rotary thermal actuators, it is necessary to develop accurate models for the device. It is important to simulate the response in term of its thermal and actuating performance with appropriate analytical method. For the present investigation, simplified analytical method along with finite difference and finite element methods are utilized to examine the actuator performance as well as validity of each method used. Besides the method, the thermal boundary conditions will play a vital role in the accuracy of the responses. This chapter presents the thermal boundary conditions, each of the methods used for analysis, the results of simulations as well as detailed parametric study. The response predicted by each method is compared and discussed. The simulated results are validated with experiments on fabricated actuators and are presented in Chapter 4.

3.1.1 Thermal boundary conditions

It is very important to set proper thermal boundary conditions for electro thermal analysis of a thermal actuator. Thermal boundary conditions may be different for various fabrication technologies. For a micro thermal actuator fabricated in Multi-User MEMS Processes (MUMPS) and operated in ambient condition, the dominant modes of heat

transfer are: lateral conduction through the structure and vertical conduction through the low gap between the structure and the substrate [29, 30, 33, 37]. Convection from the top surface of a thermal actuator is usually negligible and radiation becomes significant at high operating temperatures [29, 30, 33, 37], which is avoided for the safe operation of a thermal actuator. Therefore, convection and radiation are neglected in the modeling. Due to the bulk heat capacity of the substrate, anchor pads can be considered as fixed at room temperature, 20°C.

A simplified one dimensional heat transfer analysis [29, 30, 31, 33, 35, 36, 37] is generally employed for electro thermal analysis of a micro thermal actuator. Such analysis for linear motion actuators has been shown to provide good simulation results where temperature is considered to be constant along the width and thickness.

The rotary thermal actuators fabricated using MUMPS technique can also be analyzed using some thermal boundary conditions. A one dimensional analysis is carried out using analytical and finite difference methods. The models are also simulated using 3-D FEM.

3.1.2 Analytical Method

In various four arm designs, among the four anchor pads of the thermal actuator, two are used to apply voltage and the other two are used as ground. Because of symmetry in hot beams, in the analytical modeling a pair of beams along with the cold disc is considered and one dimensional heat transfer analysis is employed. This model can also be used for

two arm design, Design (1a) with appropriate consideration. This method provides a quick computation for the analysis of thermal actuators.

The schematic one dimensional model of the actuator is shown in Figure 3.1(a) and (b), respectively. As shown, l_h represents the length of each hot arm, ϕ is the diameter of the disc which is represented by length l_c in the following model. Figure 3.1(c) shows the heat transfer modes for a section along the length of hot arm.

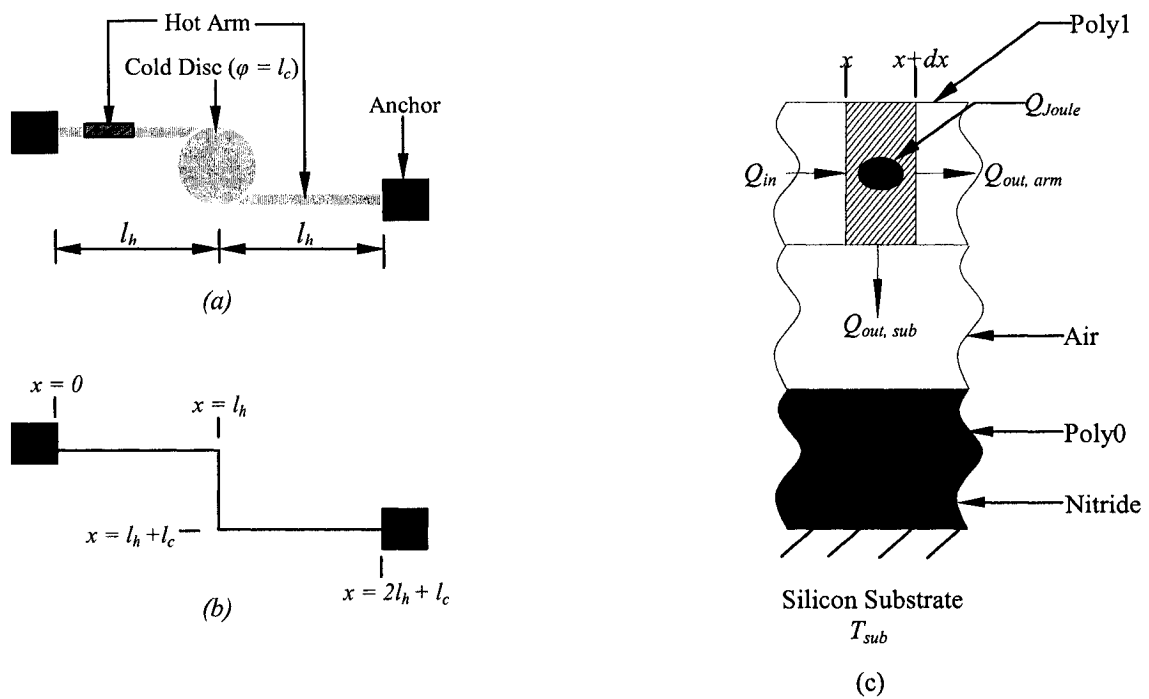


Figure 3.1: (a) Schematic rotary type polysilicon thermal actuator, (b) One dimensional coordinate system for the analysis of thermal actuator and (c) Heat transfer modes involved in a section of a micro thermal actuator

Under steady state condition, the rate of heat input to an element is equal to the rate of heat going out. For any given element of length dx , width w and thickness t_p in the

polysilicon structure (Figure 3.1(c)), the heat transfer balance under steady state condition yields the following algebraic relation,

$$Q_{in} + Q_{Joule} = Q_{out,arm} + Q_{out,sub} \quad (3.1)$$

where Q_{in} is the net rate of heat conduction into the element, Q_{joule} is the rate of heat generated inside the element due to Joule heating, $Q_{out, arm}$ is the rate of heat conducted out to the arm and $Q_{out, sub}$ is the rate of heat conducted out to the substrate. Equation (3.1) can be quantified as follows:

$$-k_p w t_p \left[\frac{dT}{dx} \right]_x + J^2 \rho_r w t_p dx = -k_p w t_p \left[\frac{dT}{dx} \right]_{x+dx} + S dx w \frac{T - T_{sub}}{R_T} \quad (3.2)$$

where T is the temperature at any given location, T_{sub} is the substrate temperature, ρ_r is the resistivity of polysilicon, k_p is the thermal conductivity of polysilicon, J is the current density of hot arm or cold disc, S is the shape factor which accounts for vertical heat conduction to the substrate based on the element shape, R_T is the thermal resistance between the structure and the substrate and it is given by,

$$R_T = \frac{t_a}{k_a} + \frac{t_{p0}}{k_{p0}} + \frac{t_n}{k_n} \quad (3.3)$$

where t_a , t_{p0} and t_n are the elevation of the element above the Poly0 layer, thickness of Poly0 layer and thickness of Silicon Nitride (Si_3N_4) layer and k_a , k_{p0} and k_n are the thermal conductivity of air, Poly0 and Si_3N_4 respectively.

Current density of hot arm and cold disc are calculated from,

$$J_h = \frac{I}{w_h t_p}, \quad J_c = \frac{2I}{w_c t_p} \quad (3.4)$$

where subscripts h and c refer to hot arm and cold disc. I is the current that passes through any section. For calculating current density of the cold disc in four arm designs,

$2I$ is considered because the additional current will pass through cold disc from the other pair of hot arms. In case of two arm design, Design (1a), the amount of current is I . And width of the cold disc is approximated from the length of a side of an equivalent square area.

A significant amount of heat is conducted vertically through the surrounding to the substrate. Amount of $Q_{out, sub}$ is dependent on the geometry of the element [32] and hence a shape factor, S is used. Shape factor for the hot arm is given by [32]

$$S = \frac{t_p}{w_h} \left(\frac{2t_a}{t_p} + 1 \right) + 1 \quad (3.5)$$

and shape factor for the disc is found latter by matching the temperature distribution of cold disc obtained from the method with that from Finite Element Analysis (FEA).

For polysilicon micro-thermal actuator, resistivity is an important property and is a strong function of temperature. Resistivity is assumed to have a linear temperature coefficient, ξ . Hence, the relationship can be expressed in the form,

$$\rho_r(T) = \rho_0[1 + \xi(T - T_{sub})] \quad (3.6)$$

After taking the limit as $dx \rightarrow 0$ and simplifying the Equation (3.2), the following is obtained,

$$\frac{d^2T(x)}{dx^2} = \frac{S(T(x) - T_{sub})}{k_p t_p R_T} - \frac{J^2 \rho_r}{k_p} \quad (3.7)$$

changing variable for Equation (3.7) with Equation (3.6) yields,

$$\frac{d^2\Theta(x)}{dx^2} - m^2\Theta(x) = 0 \quad (3.8)$$

with for any given element, $\Theta(x) = T(x) - T_{\Theta}$ (3.9a)

$$T_{\Theta} = T_{sub} + \frac{J^2 \rho_0}{k_p m^2} \quad (3.9b)$$

$$m^2 = \frac{S}{k_p t_p R_T} - \frac{J^2 \rho_0 \xi}{k_p} \quad (3.9c)$$

Solving Equation (3.8) for hot arm and cold arm the following solution is obtained

$$T_{h1}(x) = T_{H1} + c_1 e^{m_{h1}x} + c_2 e^{-m_{h1}x} \quad (3.10)$$

$$T_c(x) = T_C + c_3 e^{m_c x} + c_4 e^{-m_c x} \quad (3.11)$$

$$T_{h2}(x) = T_{H2} + c_5 e^{m_{h2}x} + c_6 e^{-m_{h2}x} \quad (3.12)$$

where the subscripts θ represents h, H for hot arms and c, C for cold disc respectively and subscripts 1 and 2 stand for first and second hot arm respectively. Since both the hot arms are symmetric, T_{H1} & T_{H2} and m_{h1} & m_{h2} will be expressed by T_H and m_h .

Since the substrate has bulk heat capacity, it can be considered to be at room temperature of 20°C, same as the anchor pad. Applying temperature boundary conditions: at $x = 0$, $T_{sub} = 20^\circ\text{C}$; at $x = (2l_h + l_c)$, $T_{sub} = 20^\circ\text{C}$ and applying the condition of continuity of both the temperature ($T_{i,hot} = T_{i,cold}$) and heat conduction ($q_{i,hot} = q_{i,cold}$) at joint points of the hot arms and cold disc, the following equation is obtained in matrix form:

$$\bar{A} \times \bar{C} = \bar{B} \quad (3.13)$$

$$\text{where, } \bar{A} = \begin{bmatrix} 1 & 1 & 0 & 0 & 0 & 0 \\ e^{m_h l_h} & e^{-m_h l_h} & -e^{m_c l_h} & -e^{-m_c l_h} & 0 & 0 \\ w_h m_h e^{m_h l_h} & -w_h m_h e^{-m_h l_h} & -w_c m_c e^{m_c l_h} & w_c m_c e^{-m_c l_h} & 0 & 0 \\ 0 & 0 & e^{m_c (l_h + l_c)} & e^{-m_c (l_h + l_c)} & -e^{m_h (l_h + l_c)} & -e^{-m_h (l_h + l_c)} \\ 0 & 0 & w_c m_c e^{m_c (l_h + l_c)} & -w_c m_c e^{-m_c (l_h + l_c)} & -w_h m_h e^{m_h (l_h + l_c)} & w_h m_h e^{-m_h (l_h + l_c)} \\ 0 & 0 & 0 & 0 & e^{m_h (2l_h + l_c)} & e^{-m_h (2l_h + l_c)} \end{bmatrix},$$

$$\bar{C} = \begin{bmatrix} c_1 \\ c_2 \\ c_3 \\ c_4 \\ c_5 \\ c_6 \end{bmatrix} \quad \text{and} \quad \bar{B} = \begin{bmatrix} T_{sub} - T_H \\ T_C - T_H \\ 0 \\ T_H - T_C \\ 0 \\ T_{sub} - T_H \end{bmatrix}$$

Solving Equation (3.13) for co-efficient C_i ($i = 1$ to 6) and substituting them back in Equations (3.10), (3.11) and (3.12) temperature profile can be obtained.

The linear thermal expansion of hot arm and cold disc can be calculated as following,

$$\Delta L_h = \alpha \int_0^{l_h} (T_h(x) - T_{sub}) dx = \alpha l_h (\bar{T}_h - T_{sub}) \quad (3.14)$$

$$\Delta L_c = \alpha \int_{l_h}^{l_h+l_c} (T_c(x) - T_{sub}) dx = \alpha l_c (\bar{T}_c - T_{sub}) \quad (3.15)$$

where, α is the co-efficient of thermal expansion and assumed to be independent of temperature, \bar{T}_h and \bar{T}_c are the average temperature of the hot arm and cold disc respectively and they can be approximated as follows:

$$\bar{T}_h = T_H + \frac{c_1}{m_h l_h} (e^{m_h l_h} - 1) - \frac{c_2}{m_h l_h} (e^{-m_h l_h} - 1) \quad (3.16)$$

$$\bar{T}_c = T_C + \frac{c_3}{m_c l_c} (e^{m_c (l_h+l_c)} - e^{m_c l_h}) - \frac{c_4}{m_c l_c} (e^{-m_c (l_h+l_c)} - e^{-m_c l_h}) \quad (3.17)$$

As the both hot arms are symmetric, \bar{T}_h is assumed to be same for both.

3.1.3 Finite Difference Method

A Finite Difference Method (FDM) analysis is presented that considers one dimensional heat transfer and this method can also provide transient temperature distribution of the thermal actuator until it reaches steady state. The model is same as that presented in Figure 3.1 and repeated in Figure 3.2. In the FDM method, the device along its length is, however, divided into discrete nodes spaced by equal distance Δx as shown in Figure 3.2(c) and each node is assigned an elemental volume of Δu . Properties of a specific element is represented by the corresponding node. In this analysis, curved beams were modeled with length equal to the arc length of the curved beam.

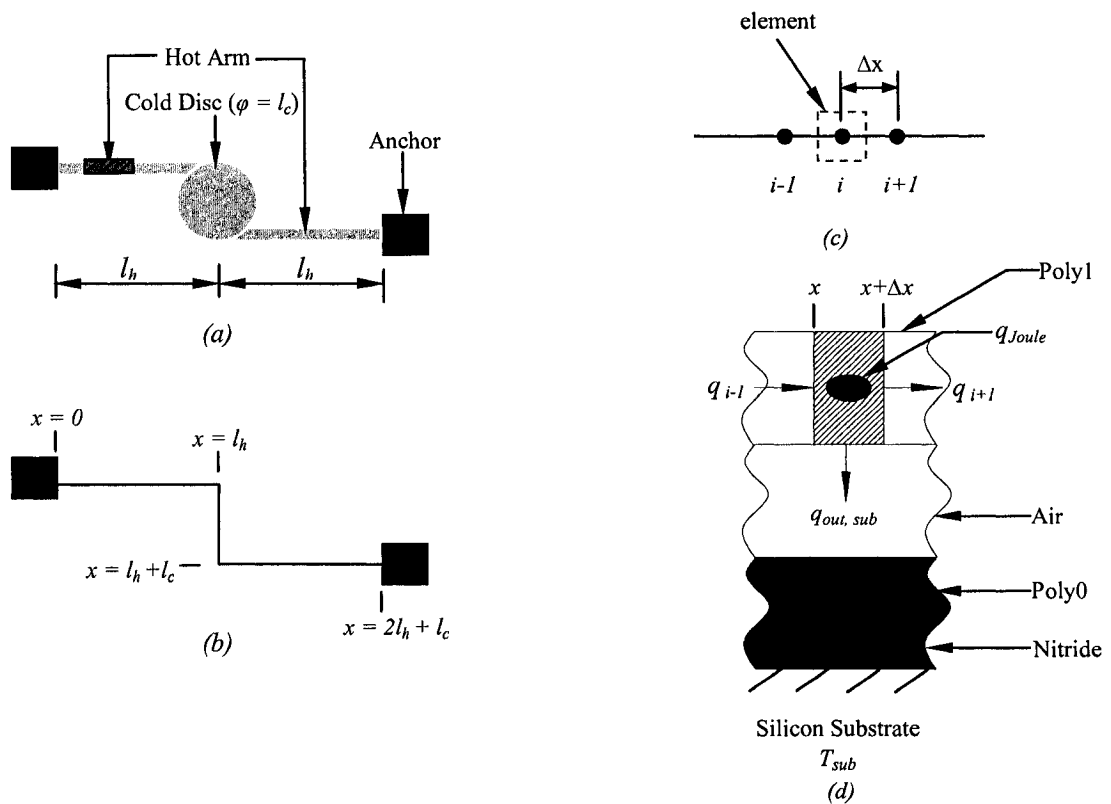


Figure 3.2: (a) Scheme of rotary type micro thermal actuator, (b) simplified coordinate system, (c) representation of FDM nodal system along the length of the actuator and (d) Heat transfer modes involved in i th element of micro thermal actuator

Energy balance for i th node yields following algebraic relation:

$$q_{joule} + q_{i-1} - q_{i+1} - q_{out, sub} = q \quad (3.18)$$

where, q_{joule} is the rate of energy generated in i th element by joule heating, q_{i-1} is the rate of heat input to the i th element from $i-1$ th element, q_{i+1} is the rate of heat output from i th element to the next element, $q_{out, sub}$ accounts for heat transferred to the surrounding from i th element and q is the rate of heat accumulation in the element. Solving this equation for all the nodes in the structure yields nodal temperatures.

Rate of heat generation due to joule heating can be approximated as,

$$q_{joule} = J^2 \rho_r \Delta u_i \quad (3.19)$$

where, J is the current density in a given element, ρ_r is the temperature dependent resistivity and Δu_i is the element volume. Current density can be approximated as,

$$J_h = \frac{I}{w_h t_p} \quad \text{and} \quad J_c = \frac{2I}{w_c t_p} \quad (3.20)$$

where, the subscripts h and c stand for hot arm and cold disc respectively, w is the width of any given element and t_p is the thickness. I is the current passing through any given element. For calculating current density of cold disc in four arm designs, $2I$ is considered in order to account for the presence of another pair of hot arms. In case of two arm design, Design (1a) the current through cold disc is I . Width of cold disc is approximated from the length of a side of an equivalent square area.

Lateral conduction rate between nodes, $i-1$ and i is given by,

$$q_{i-1} = \frac{k_p A_c}{\Delta x} [T_{i-1}(k) - T_i(k)] \quad (3.21)$$

where, A_c is cross sectional area at any i th node, k_p is thermal conductivity of polysilicon and Δx is the distance between the nodes. In this literature, $T_i(k)$ will represent the temperature of i th node at k th time. There is a time increment of Δt between each time step.

A significant amount of heat is conducted vertically through the surrounding to the substrate. Rate of vertical heat conduction to the surrounding can be quantified as,

$$q_{out,sub} = \frac{SA_s}{R_T} [T_i(k) - T_{sub}] \quad (3.22)$$

where, T_{sub} is the temperature of the substrate, A_s represents surface area of the element which is in parallel to the substrate, R_T is the thermal resistance between the structure and the substrate and amount of $q_{out,sub}$ is dependent on the geometry of the element [32] and hence a shape factor, S is used. Shape factor for hot arm is given by [32]:

$$S = \frac{t_p}{w_h} \left(\frac{2t_a}{t_p} + 1 \right) + 1 \quad (3.23)$$

and shape factor for the disc is found latter by matching the temperature distribution of cold disc obtained from ensuing method with that from Finite Element Analysis (FEA).

Thermal resistance, R_T is given by,

$$R_T = \frac{t_a}{k_a} + \frac{t_{p0}}{k_{p0}} + \frac{t_n}{k_n} \quad (3.24)$$

where, t_a , t_{p0} and t_n are the thickness of air, thickness of Poly0 layer and thickness of Silicon Nitride (Si_3N_4) layer and k_a , k_{p0} and k_n are the thermal conductivity of air, Poly0 and Si_3N_4 , respectively.

Rate of heat accumulation in the node is calculated from,

$$q = \frac{\rho c_p \Delta u_i}{\Delta t} [T_i(k+1) - T_i(k)] \quad (3.25)$$

where, ρ and c_p are the density and specific heat of polysilicon respectively.

Resistivity is assumed as a function of temperature and can be expressed as,

$$\rho_r = \rho_o [1 + \xi(T_i(k-1) - T_{sub})] \quad (3.26)$$

where, ξ is linear temperature co-efficient of resistivity.

Substituting Eqn (3.19)-(3.26) into Eqn (3.18), an explicit expression for the temperature at time $k+1$, in terms of temperatures at time k , the input and the boundary conditions can be formed as,

$$T_i(k+1) = \frac{\Delta t}{\rho c_p \Delta u_i} \left[J^2(k) \rho \Delta u_i + \frac{SA}{R_f} (T_{sub} - T_i(k)) + \frac{k_p A_c}{\Delta x} (T_{i-1}(k) - T_i(k)) + \frac{k_p A_c}{\Delta x} (T_{i+1}(k) - T_i(k)) \right] + T_i(k) \quad (3.27)$$

Solving Equation (3.27) with proper initial and boundary conditions, the temperature of any element at any given time step can be found through out the structure. As per the initial condition, room temperature will prevail through out the structure at 20°C. For the subsequent thermal boundary conditions, anchors are assumed to be constrained at room temperature of 20°C, due to the bulk heat capacity of substrate.

When the steady state is reached, average temperature of a hot arm can be measured and used to measure the thermal expansion of the free end of the beam as follows:

$$\Delta L_h = \alpha l_h (T_{avg} - T_{sub}) \quad (3.28)$$

where, α is the co-efficient of thermal expansion and T_{avg} is the average temperature of a hot arm.

Though the Analytical and FDM methods shown above were used for specific actuator geometry, Design 2 (as specified in Chapter 2), but they can also be used for Design 1 and 3 (as specified in Chapter 2) with proper length parameter consideration. Schematic of Design 1 along with one dimensional coordinate system used is shown below-

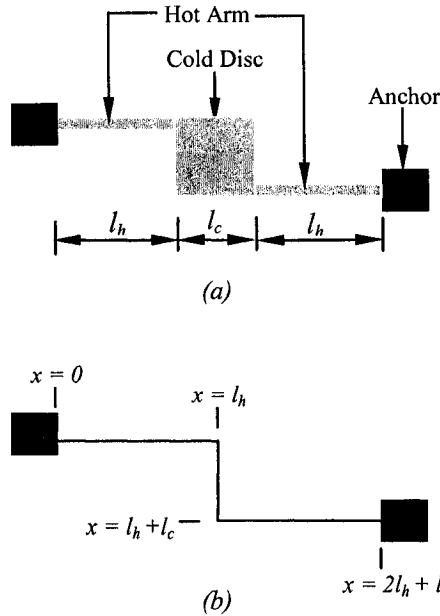


Figure 3.3: (a) Schematic rotary type polysilicon thermal actuator with square disc and (b) One dimensional coordinate system for the analysis of thermal actuator

Similarly, the schematic of the model and one dimensional coordinate system used for Design 3 is presented in Figure 3.4-

S

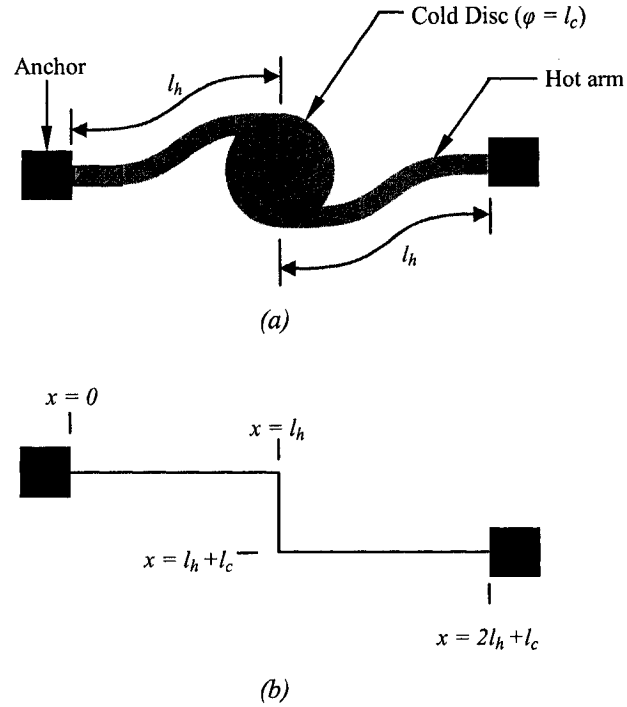


Figure 3.4: (a) Schematic rotary type polysilicon thermal actuator with square disc and (b) One dimensional coordinate system for the analysis of thermal actuator

It might be noted that for Design 3, length of beam, l_h is approximated from the arc length of the curved beam.

3.2 Rotational Analysis

The flexural longitudinal stiffness of the hot arms is very much dependent on the boundary support conditions. If one end of the hot arm is free, then one would expect maximum longitudinal expansion at the free end. But the presence of the rigid cold disc at the end introduces compressive load on the arms leading to transverse motion of the beam in addition to the longitudinal expansion. The ratio of the longitudinal expansion to the lateral or transverse motion is dependent on the size of the disc. As the purpose of this

thesis is to demonstrate the feasibility of the novel actuator, free expansion is assumed for hot arms, for simplicity.

For rotational analysis, a cantilever analogy is used i.e., one end is free to move. Rotation angle δ is approximated from the linear thermal expansion of a hot arm using the following simplified formula,

$$\Delta L_h = R\delta \quad (3.29)$$

where R is the radius of the disc, ΔL_h is the total expansion of the free end and δ is the angle of rotation. Here the thermal expansion of the cold disc is neglected because it is negligible.

3.3 Finite Element Analysis

Finite element analysis of the actuator was carried out using ANSYS 8.1. In the FEA model, an air volume was defined from the level of top surface of the structure followed with Poly0 layer and nitride layer. Since convection heat transfer is negligible and radiation is significant only at high temperature, the air layer on top of the structure was not defined. 3-D models of actuator in ANSYS are shown in Fig. 3.5 through Fig. 3.8 for each of the design considered. A coupled field element, Solid98 was used for meshing the structure and thermal element, Solid87 was used for meshing the surrounding layers.

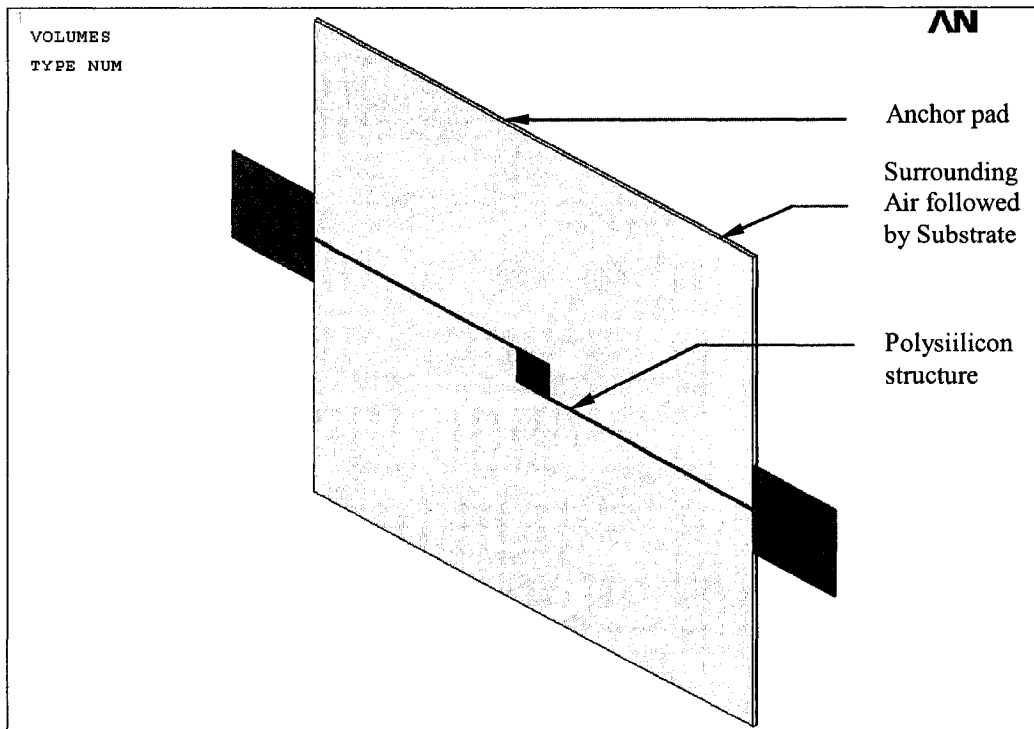


Figure 3.5: A 3-D model of Actuator Design (1a) in ANSYS

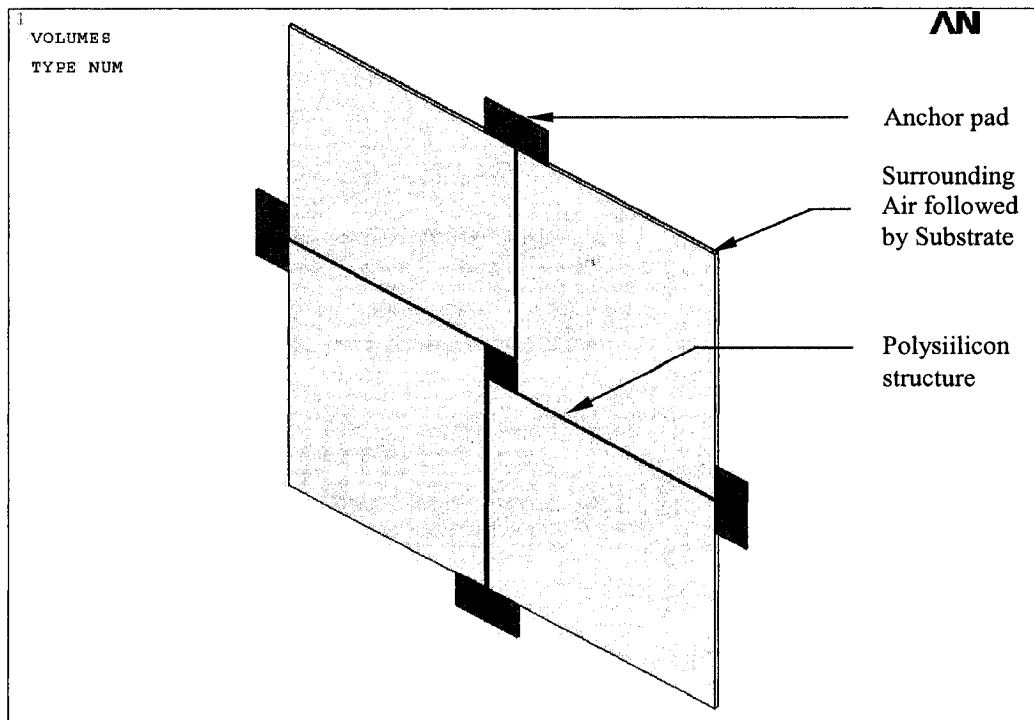


Figure 3.6: A 3-D model of Actuator Design (1b) in ANSYS

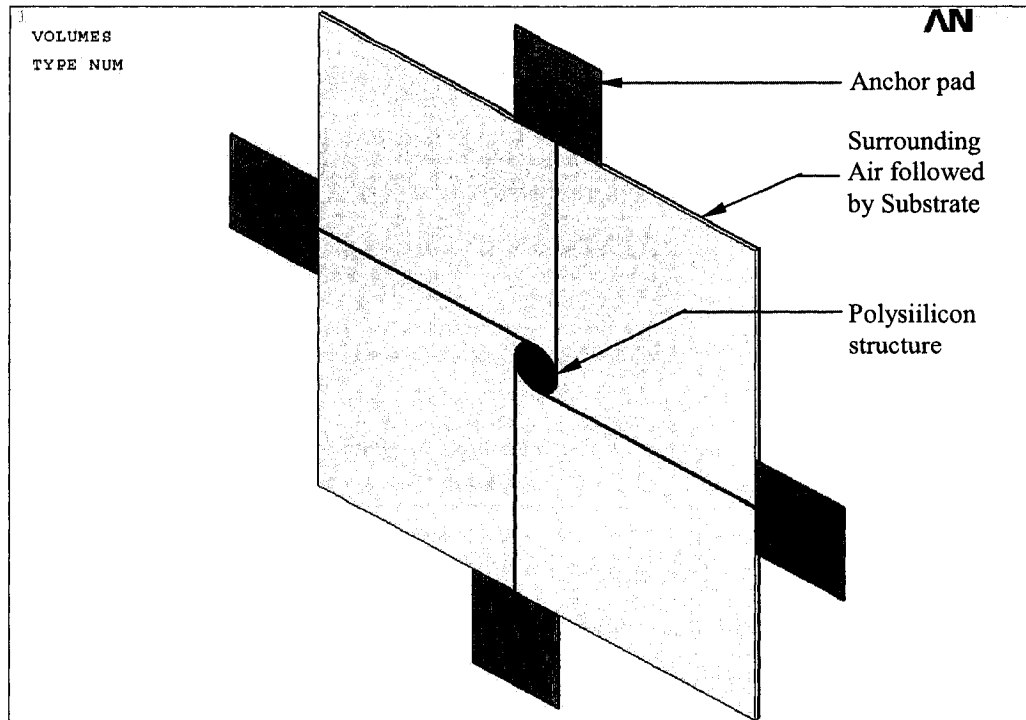


Figure 3.7: A 3-D model of Actuator Design (2) in ANSYS

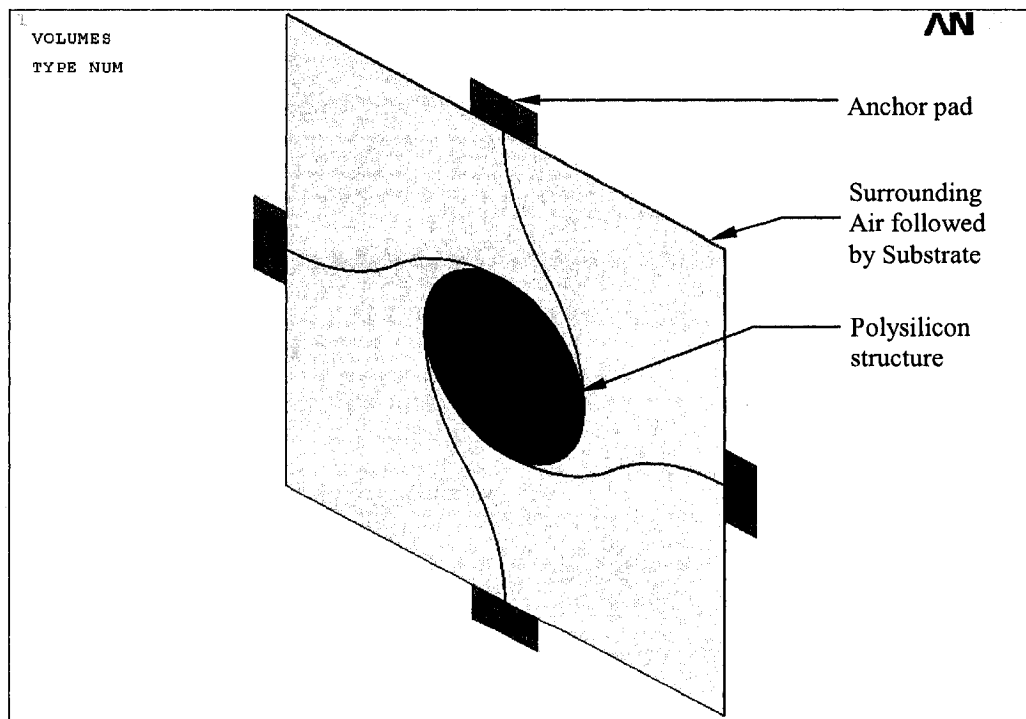


Figure 3.8: A 3-D model of Actuator Design (3) in ANSYS

Dimension of FEA models for various actuator designs are given in Table 3.1. In the Table 3.1, FEA models (1a), (1b), and (3) corresponds to actuator design (1a), (1b) and (3) respectively. Dimensions of hot arm and cold disc influence the performance of the actuator greatly. To facilitate the study this effect, a parametric analysis with different dimensions were considered on Design (2). Hence, Models (2a), (2b), (2c) and (2d) correspond to actuator basic Design (2).

Table 3.1: Dimensions of various models

Model	l_h (μm)	l_c or R (μm)
1(a)	250	40
1(b)	250	40
2(a)	250	20
2(b)	250	25
2(c)	350	25
2(d)	350	30
3	732	250

In FEA simulation, the anchor pads were constrained from motions in all directions and were assumed to be at room temperature of 20°C . The bottom surface of nitride layer was constrained at room temperature of 20°C . Electrical potential was applied between two anchor pads and the other two anchor pads were treated as ground. For safe operation of the actuator due to material property limitation, simulations on actuators were done for different voltages which yield temperature of the actuator under 950°C . For rotation measurement of the disc, slope of an imaginary line connecting two diametrically opposite nodes, before and after applying loads, were used.

Actuator Model (1a) was simulated with 12V in ANSYS as this voltage yields the maximum temperature lower than 950°C which is considered as the limit for simulation. Figure 3.9 shows temperature solution of Model (1a) at this voltage and the red color legend represents the hottest zone while blue legend represents the coldest region. It was found that the maximum temperature of 872.5 °C occurs in the middle of the beam at this voltage. Figure 3.10 shows the vector summation of the motion of actuator at this application voltage. It is evident that the buckling happens in the beam and the disc rotates about its center.

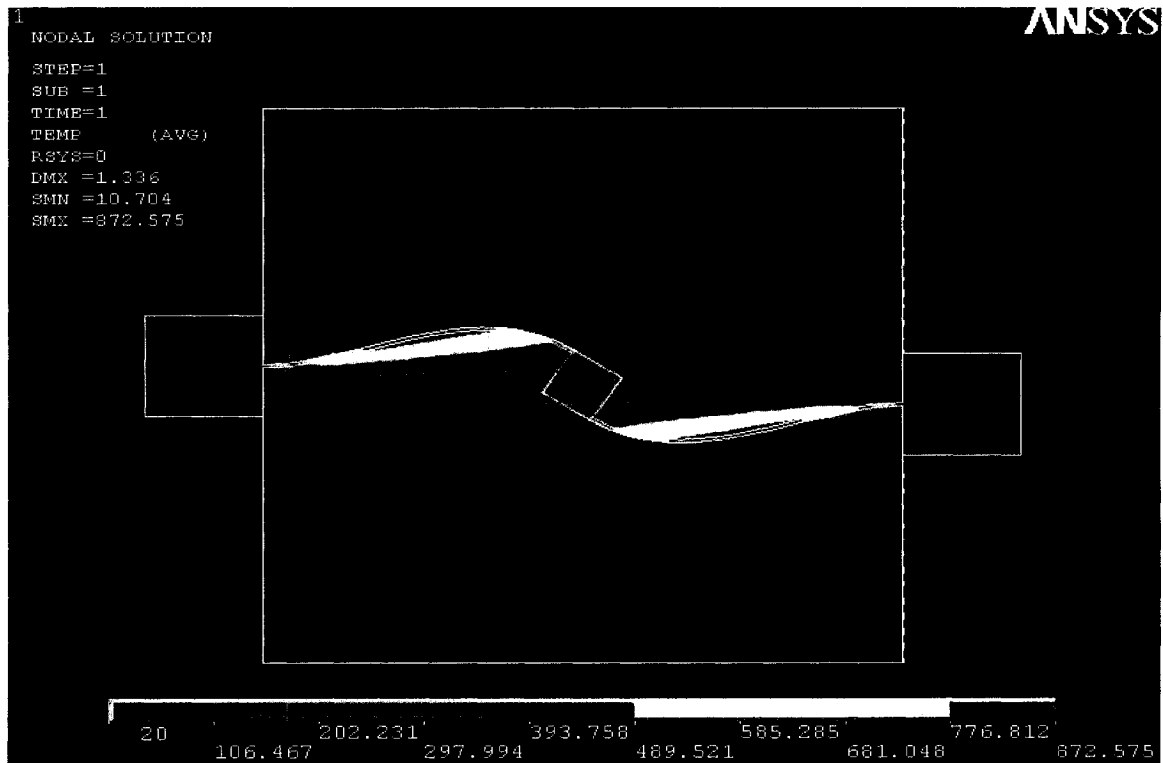


Figure 3.9: Temperature solution for Model (1a) in ANSYS, under the application of 12V or 3.9606mA

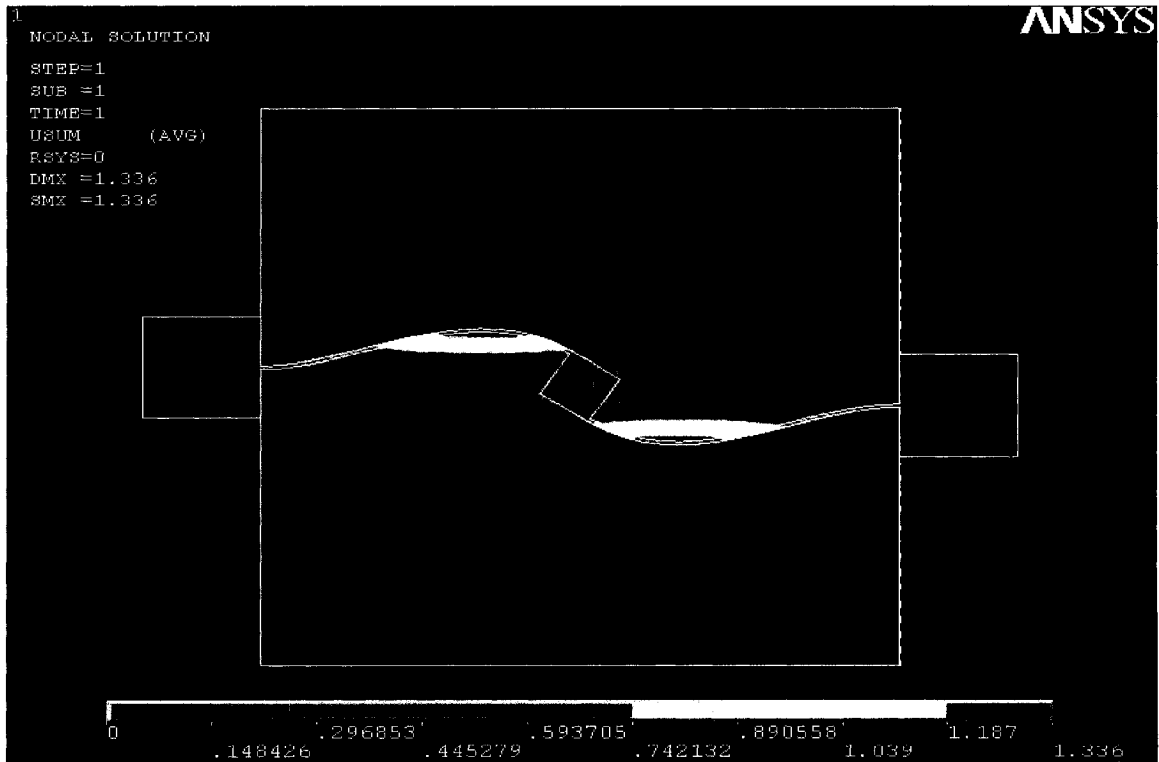


Figure 3.10: Vector Summation of displacement for Model (1a) in ANSYS, under the application of 12V or 3.9606mA

Similarly, actuator Model (1b) was simulated for 12V. Figure 3.11 shows temperature solution of Model (1b) at this voltage. It was found that the maximum temperature of 862.2°C occurs in the middle of the beam at this voltage. Figure 3.12 shows the vector summation of the motion of actuator at this voltage. It is evident that the buckling happens in the beam and the disc rotates about its center.

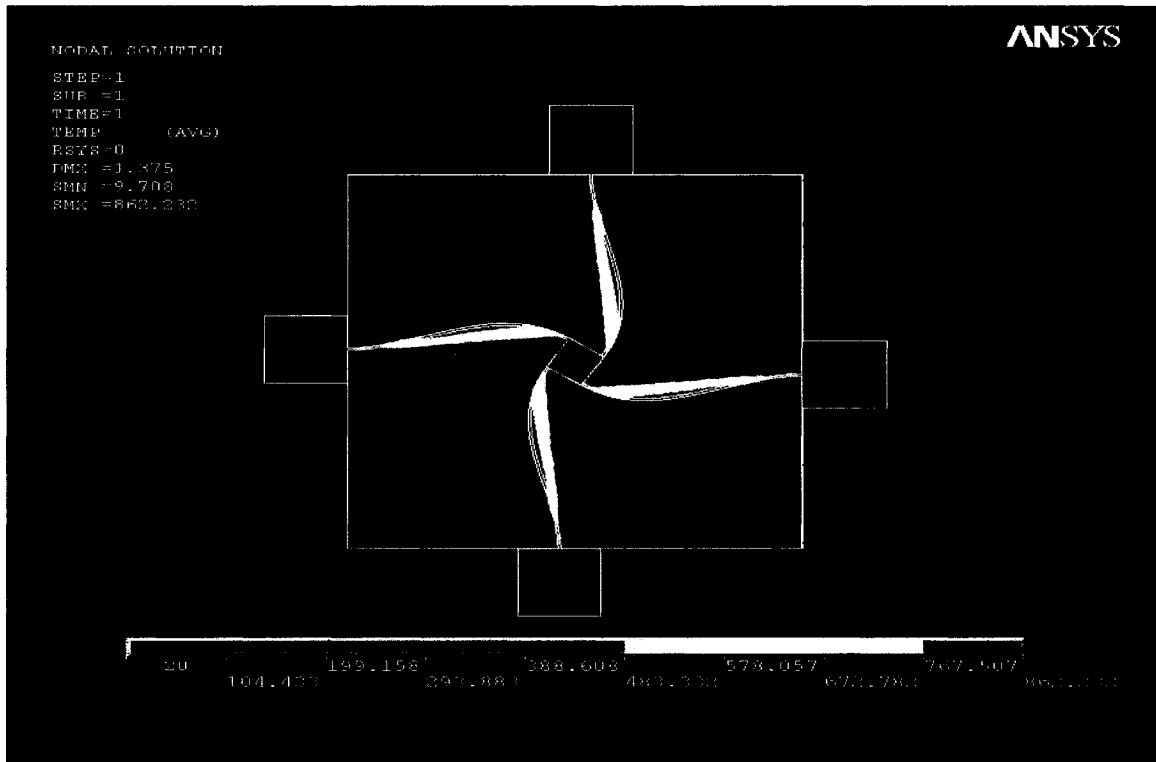


Figure 3.11: Temperature solution for Model (1b) in ANSYS, under the application of 12V or 3.9263mA

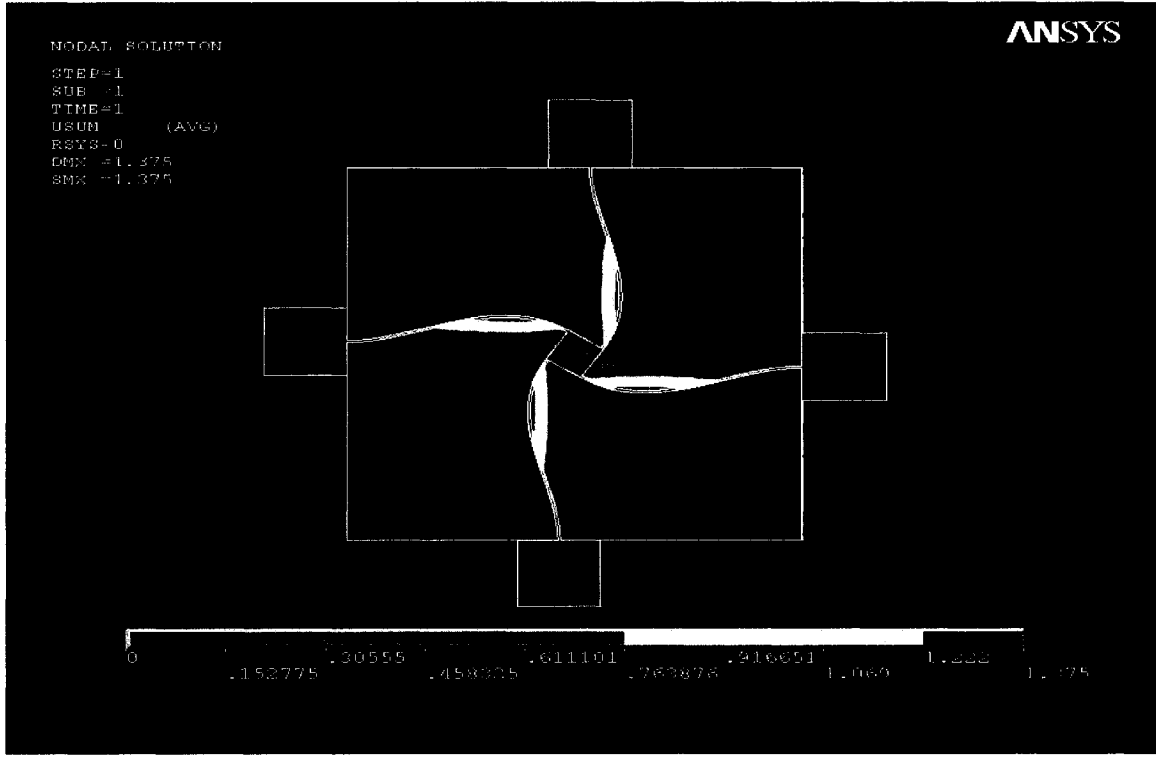


Figure 3.12: Vector Summation of displacement for Model (1b) in ANSYS, under the application of 12V or 3.9263mA

Similarly, actuator Models (2a) and (2b) were also simulated for 12V. Figures 3.13 and 3.15 show temperature solutions for Models (2a) and (2b) respectively at this voltage. Similar to previous simulations, maximum temperature of 914.5°C and 920.9°C occurs for Models (2a) and (2b) respectively in the middle of the beam. Figures 3.14 and 3.16 show the vector summation of motion for Models (2a) and (2b) respectively at 12V. It is evident for both the models that the buckling happens in the beam and the disc rotates about its center.

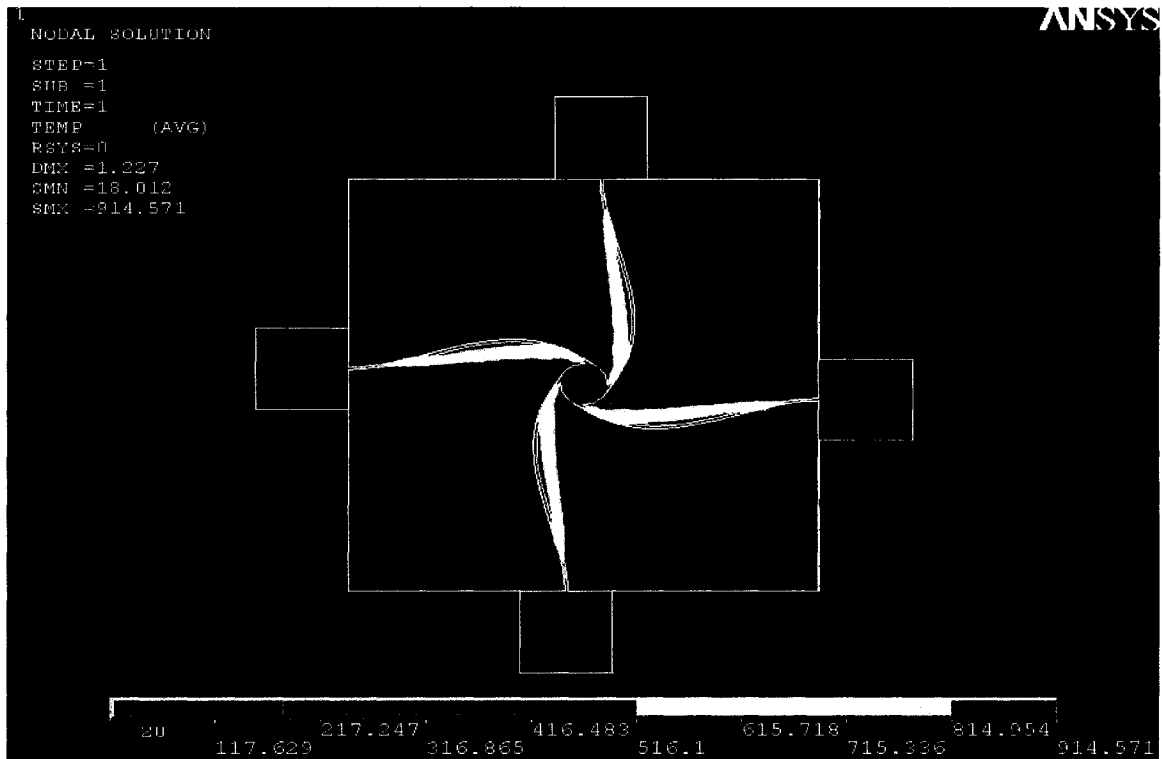


Figure 3.13: Temperature solution for Model (2a) in ANSYS, under the application of 12V or 4.0439mA

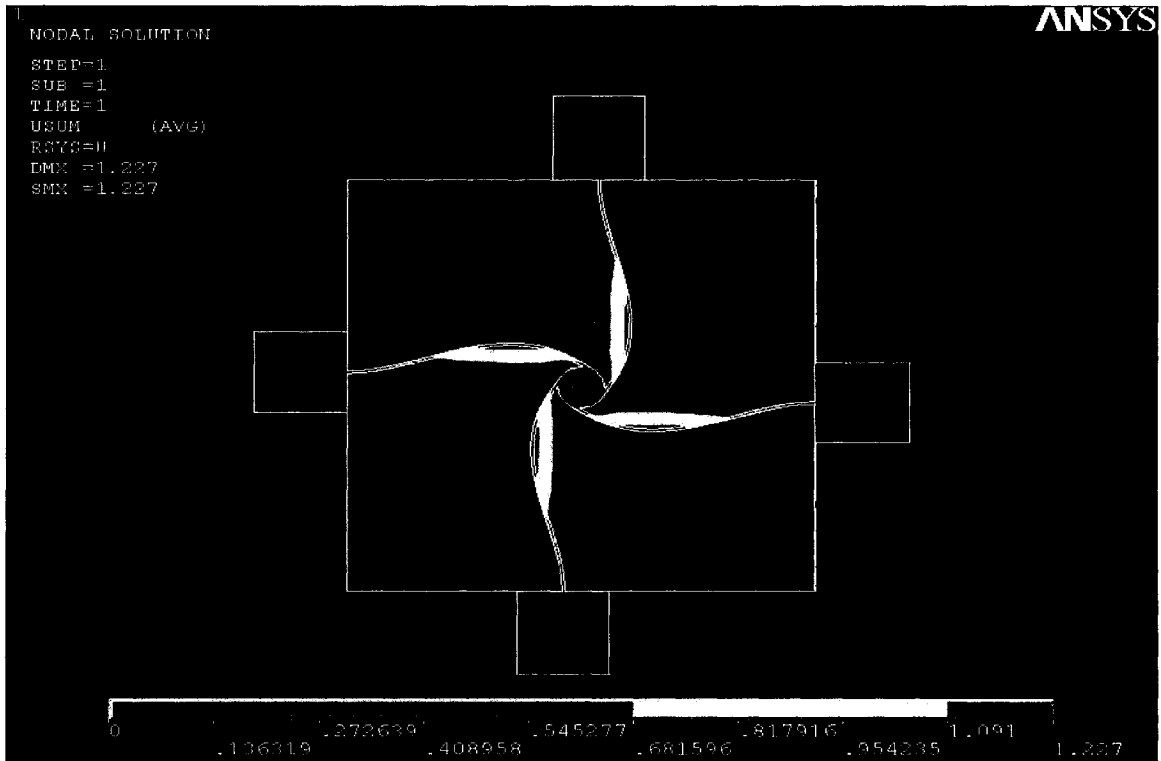


Figure 3.14: Vector Summation of displacement for Model (2a) in ANSYS, under the application of 12V or 4.0439mA

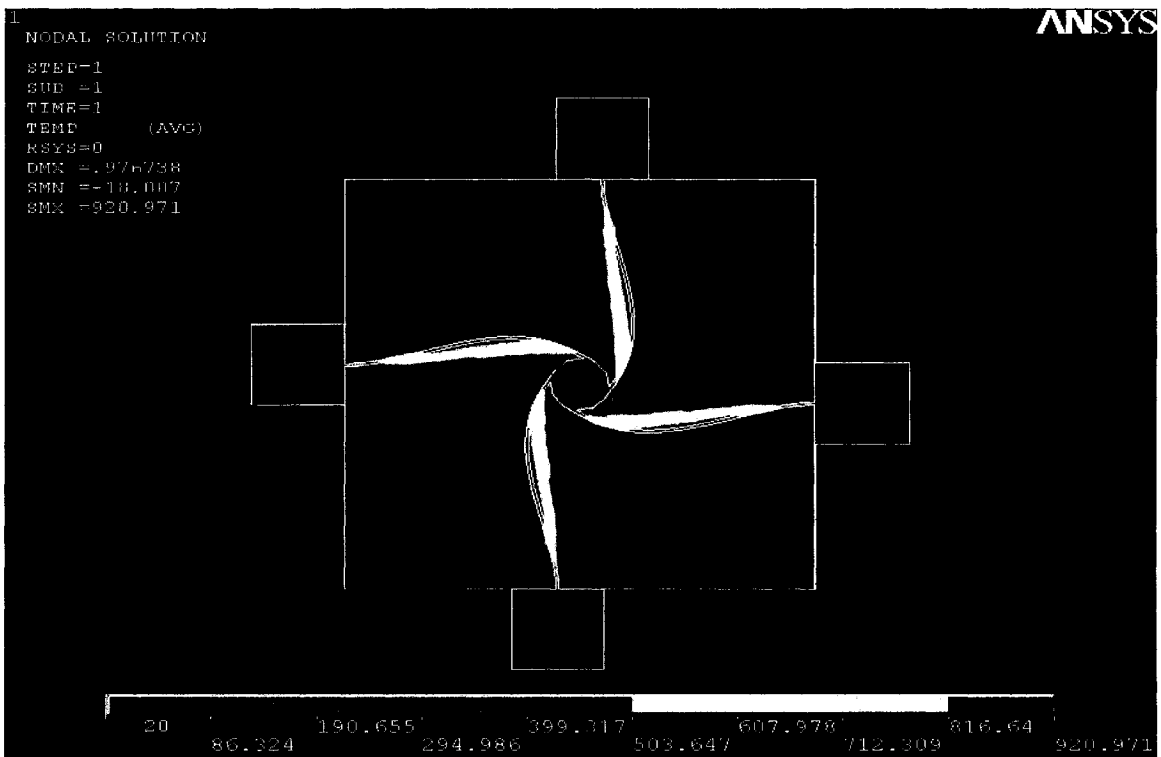


Figure 3.15: Temperature solution for Model (2b) in ANSYS, under the application of 12V or 4.0949mA

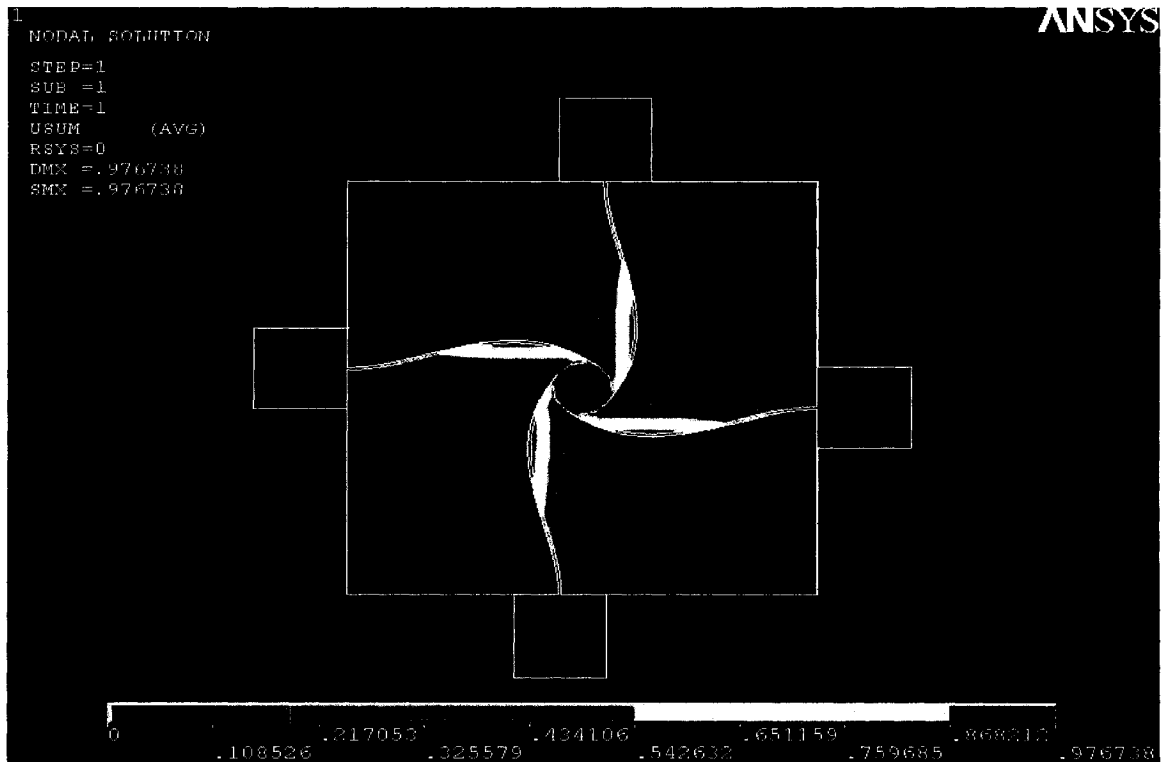


Figure 3.16: Vector Summation of displacement for Model (2b) in ANSYS, under the application of 12V or 4.0949mA

Similarly, actuator Models (2c) and (2d) were also simulated for 16.5V respectively. Following Figures 3.17 and 3.19 show temperature solution for Models (2c) and (2d) respectively at 16.5V. Similar to previous simulations, maximum temperature occurs in the middle of the beam length. Following Figures 3.18 and 3.20 show the vector summation of motion for the Models (2c) and (2d) respectively at 16.5V. As discussed earlier, it is evident that the buckling happens in the beam in Models (2c) and (2d), and the disc rotates about its center.

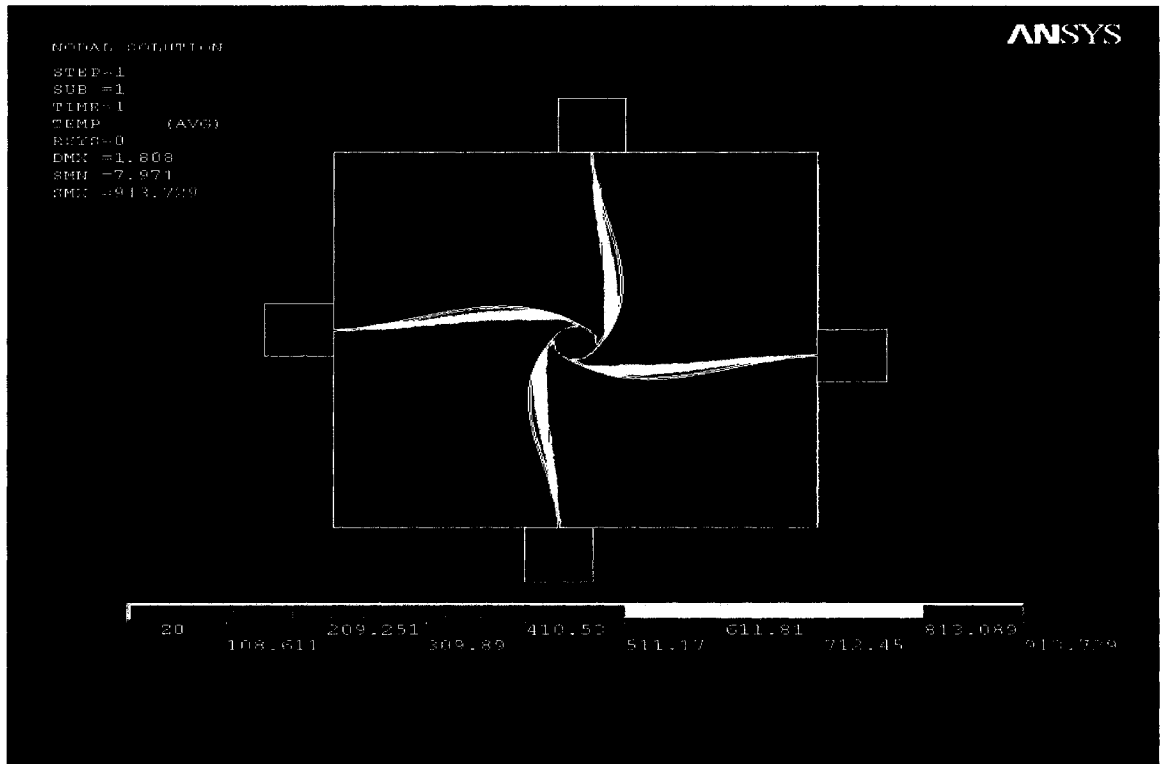


Figure 3.17: Temperature solution for Model (2c) in ANSYS, under the application of 16.5V or 3.9309 mA



Figure 3.18: Vector Summation of displacement for Model (2c) in ANSYS, under the application of 16.5V or 3.9309 mA

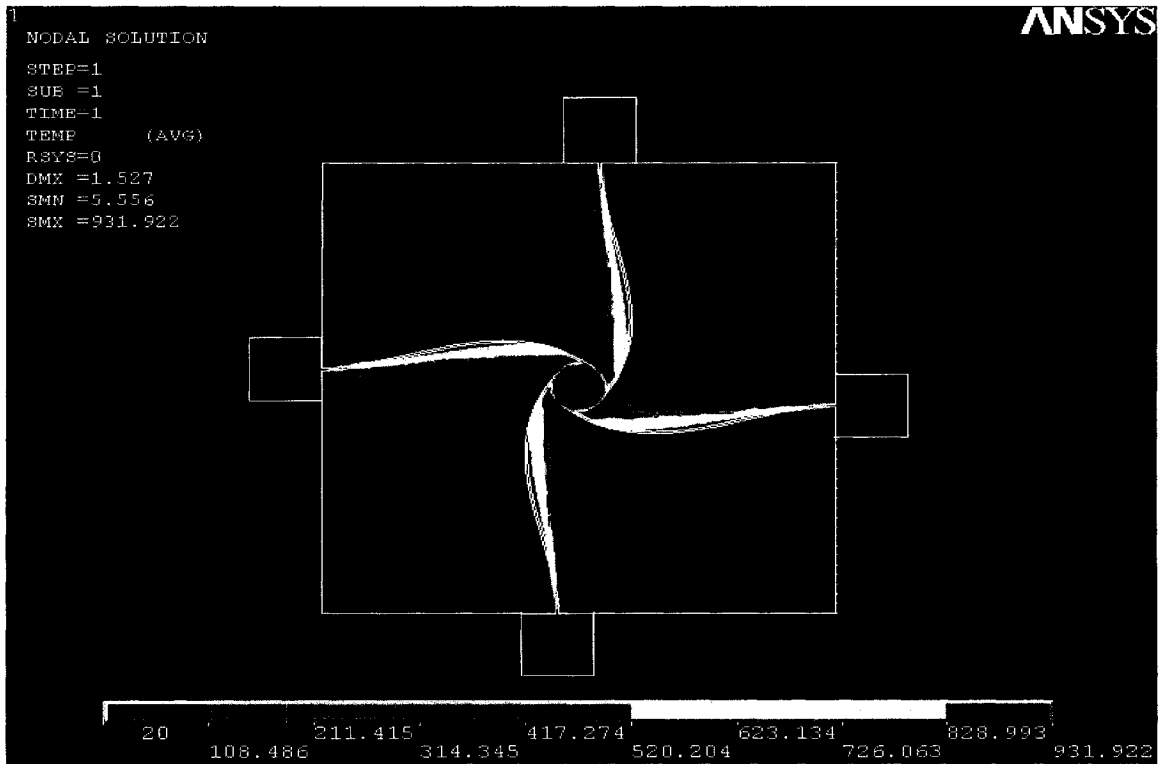


Figure 3.19: Temperature solution for Model (2d) in ANSYS, under the application of 16.5V or 3.9495mA

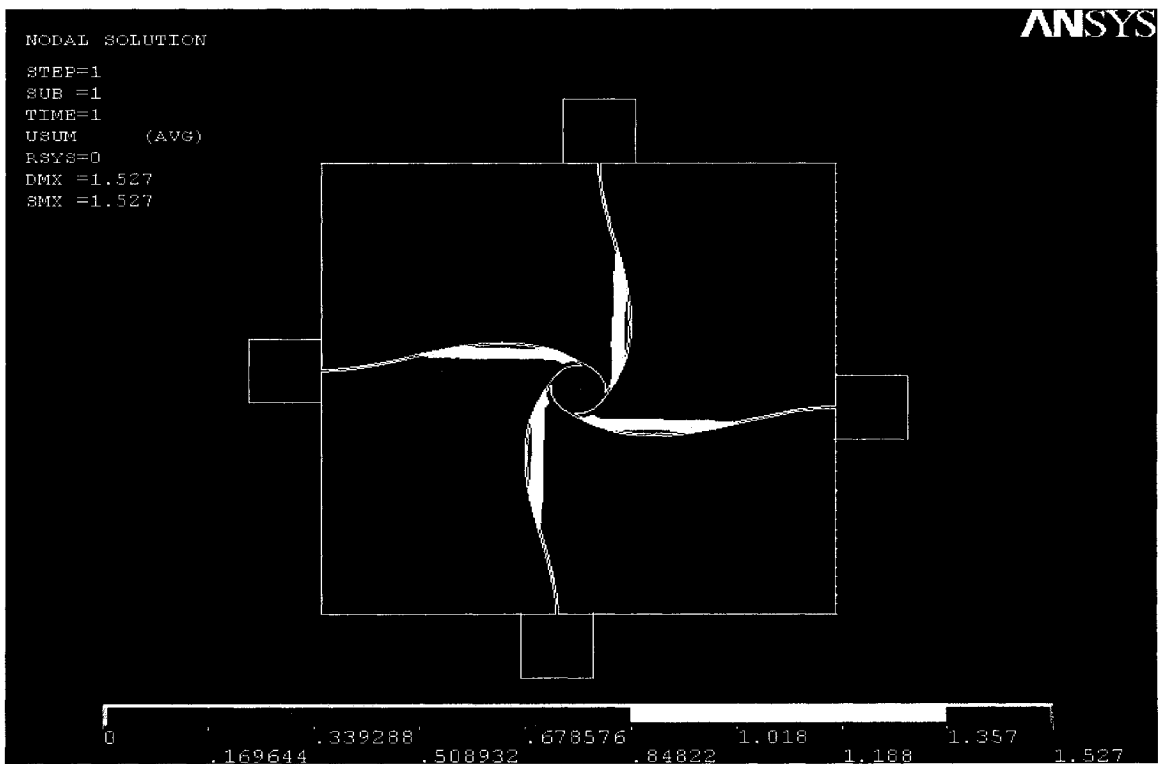


Figure 3.20: Vector Summation of displacement for Model (2d) in ANSYS, under the application of 16.5V or 3.9495mA

Similarly, actuator Model (3) was also simulated for 20V. The Figure 3.21 shows temperature solution for Model (3) at 20V. As expected maximum temperature occurs in the middle of the beam length and the disc sustains the minimum temperature in the actuator structure. It should be noted that inspite of higher application voltage than previous simulations the maximum temperature generated in the structure is 404.5°C which is considerably lower than that of previous simulation. Figure 3.22 shows the vector summation of the motion of actuator at 20V. In this case the beam does not go through significant buckling and the maximum of vector summation is significantly lower even at higher voltage of 20V.

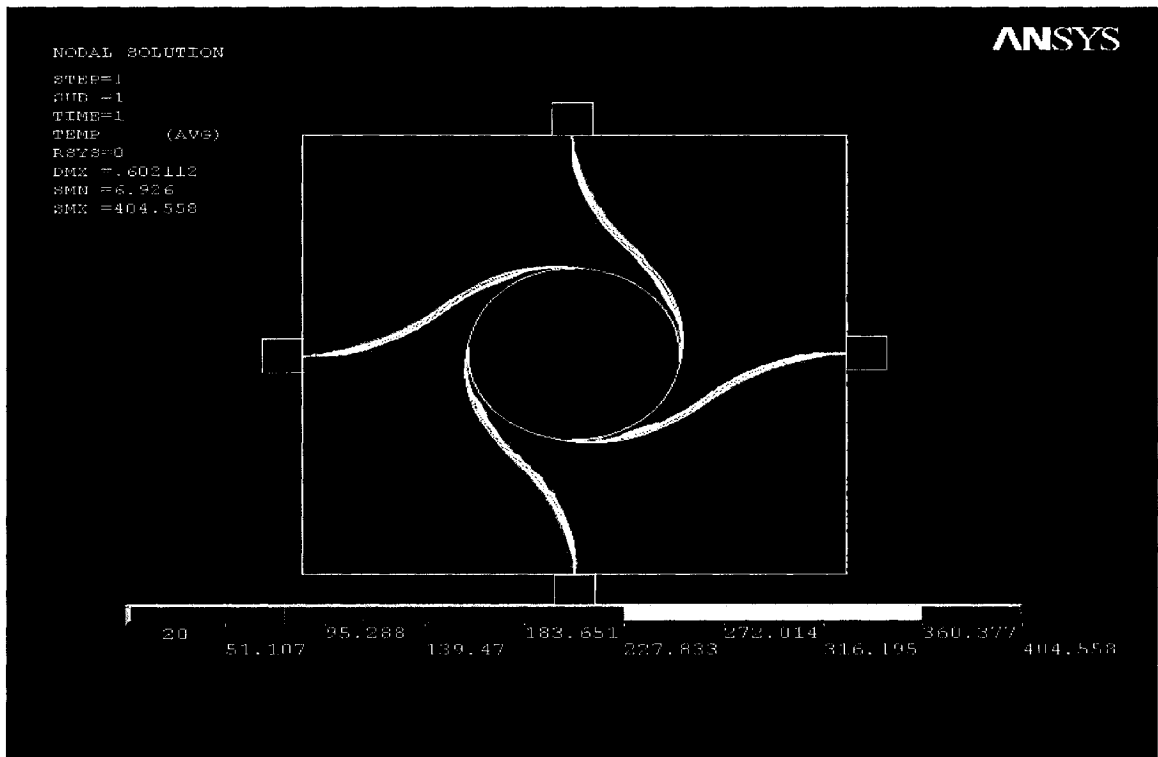


Figure 3.21: Temperature solution for Model (3) in ANSYS, under the application of 20V or 3.1004 mA

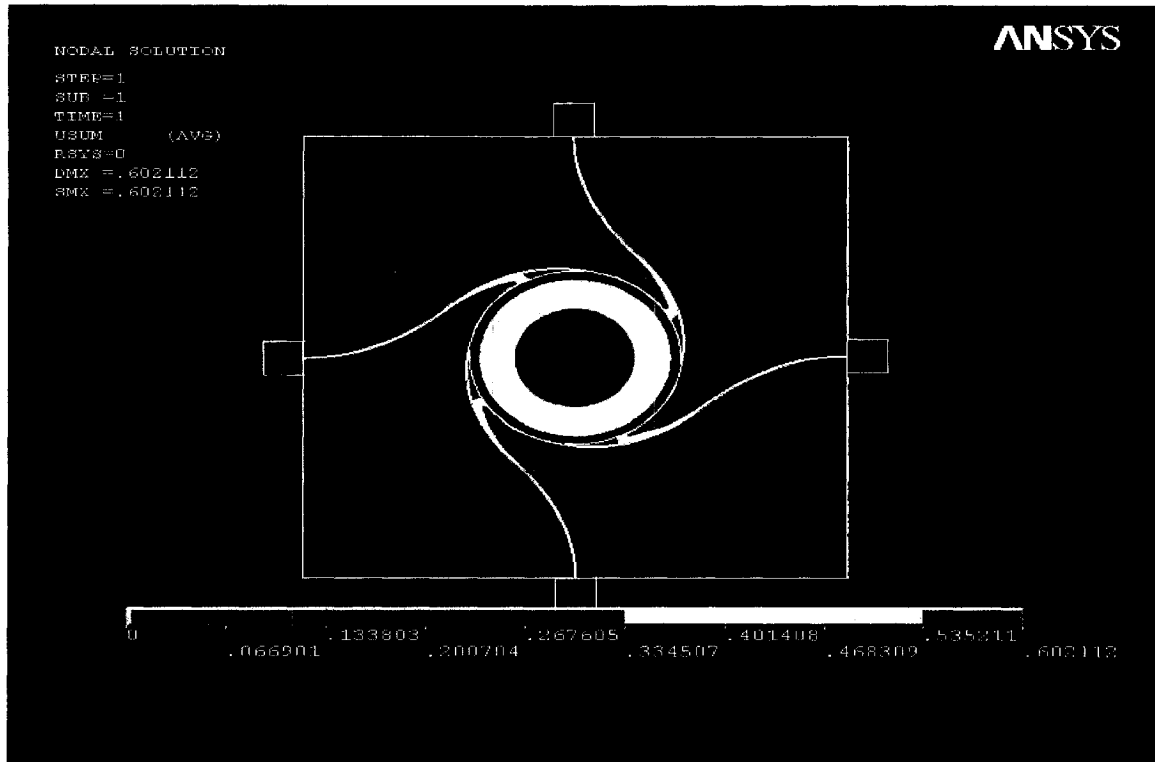


Figure 3.22: Vector Summation of displacement for Model (3) in ANSYS, under the application of 20V or 3.1004mA

The parameters used for the simulation are obtained from Reference [44] and are presented in table 3.2.

Table 3.2: Properties used for simulations [38, 39 and 44]

Parameter	Value
Elastic Modulus of polysilicon (E)	169 GPa
Poisson's ratio polysilicon (ν)	0.22
Coefficient of thermal expansion of polysilicon (α)	$2.7 \times 10^{-6} \text{K}^{-1}$
Electrical resistivity of polysilicon at room temperature (ρ_0)	$2 \times 10^{-3} \Omega\text{-cm}$
Resistivity co-efficient of polysilicon (ξ)	$1.25 \times 10^{-3} \text{K}^{-1}$
Thermal conductivity of Poly1 (k_p)	$32 \text{ W}\cdot\text{m}^{-1}\cdot\text{K}^{-1}$
Thermal conductivity of Poly0 (k_{p0})	$32 \text{ W}\cdot\text{m}^{-1}\cdot\text{K}^{-1}$
Thermal conductivity of air (k_a)	$0.026 \text{ W}\cdot\text{m}^{-1}\cdot\text{K}^{-1}$
Thermal conductivity of nitride (k_n)	$2.25 \text{ W}\cdot\text{m}^{-1}\cdot\text{K}^{-1}$
Specific heat of Polysilicon1	$705 \text{ JKg}^{-1}\text{K}^{-1}$
Thickness of Poly1, t_p	$2 \mu\text{m}$
Thickness of air, t_a	$2 \mu\text{m}$
Thickness of Poly0, t_{p0}	$0.5 \mu\text{m}$
Thickness of Nitride, t_n	$0.6 \mu\text{m}$

3.4 Shape factors

Temperature distribution of cold disc obtained from analytical method and FDM was compared with that of FEA. From the best match for temperature distribution, shape factor for disc was found for various designs as given in Table 3.3.

Table 3.3: Shape factor for cold disc of various models

Model	S_c
1(a)	1.125
1(b)	0.625
2(a)	0.625
2(b)	0.6
2(c)	0.6
2(d)	0.575
3	0.35

3.5 Results and Discussions

Steady state temperature profile is important in determining safe operation limit of the actuator. Using the shape factor for cold disc in analytical method, steady state thermal profile of the actuator Model (1a) at 12V was found and when compared to that of FEA in Figure 3.23, they show close agreement, although the temperature of the beam obtained from FEA is little higher than that of analytical method approximately in the half way of beam length. It is also evident from Figure 3.23 that maximum temperature of the actuator occurs in the half way of the beam length. When average temperature for Model (1a) obtained from analytical method, FDM and FEA at different application voltages is compared in Figure 3.24, they show close agreement.

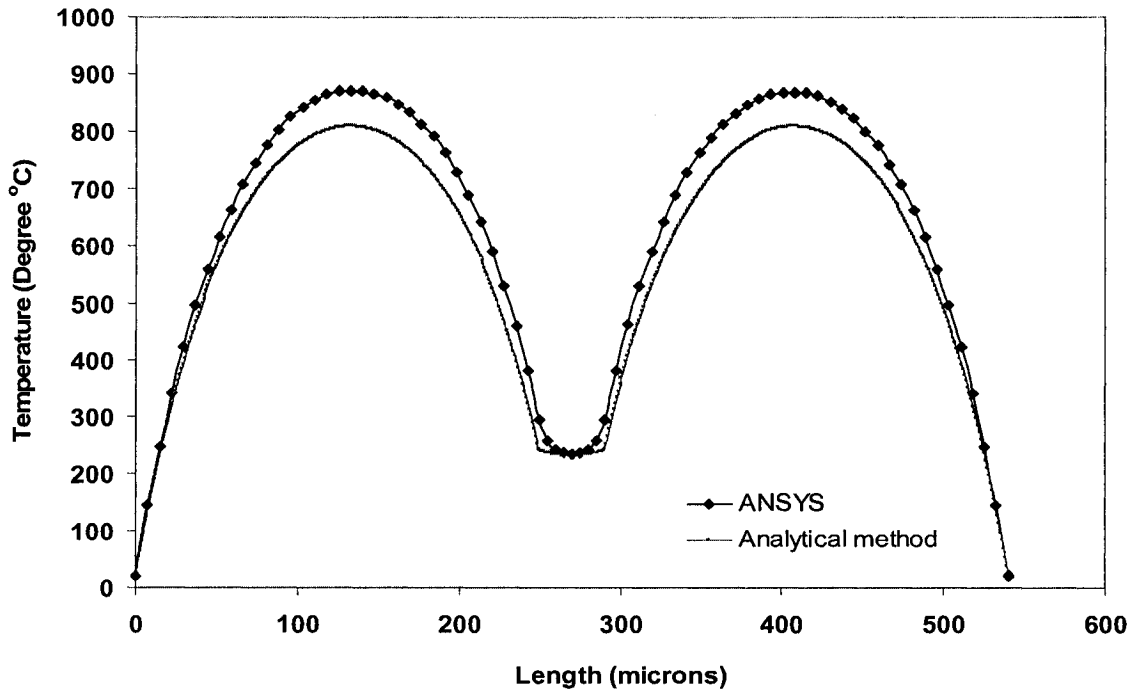


Figure 3.23: Temperature distribution of Model (1a) under the application of 12V or 3.9606mA

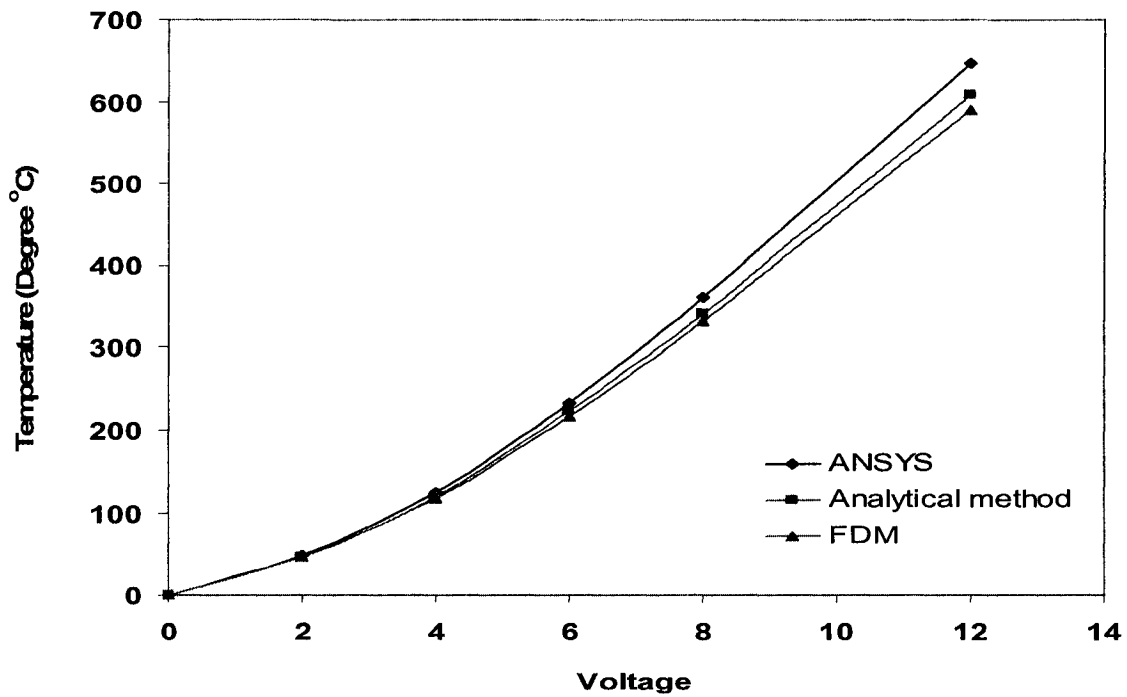


Figure 3.24: Average temperature of one hot arm of Model (1a) at different applied voltages

Average temperature of a hot arm determines the amount of thermal expansion and hence plays important role in the rotation of the disc. Using the average temperature in

analytical method and FDM, rotation of the disc of Model (1a) is calculated at different application voltages and when compared to that from FEA in Figure 3.25, they show close agreement with some variation. As the purpose of this thesis is to demonstrate the feasibility of the rotary actuator, hence this variation can be considered acceptable. The main reason for the deviation can be due to inclusion of buckling in ANSYS, while the analytical method was focused on the thermal behavior.

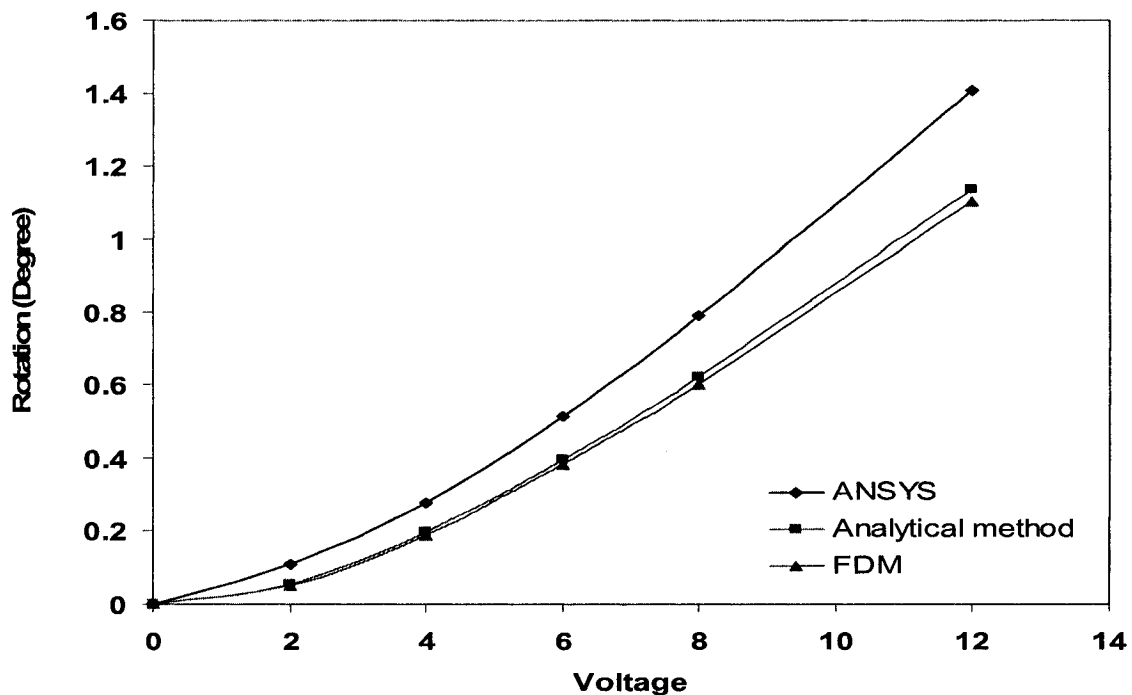


Figure 3.25: Rotation (in degrees) of the cold disc of Model (1a) at different applied voltages

Similarly, comparison of steady state temperature profile of Model (1b) at 12V obtained from analytical method and FEA in Figure 3.26, shows close agreement. As expected the maximum temperature of the beam of Model (1b) occurs approximately in the half way of the beam length. Average temperature of a hot arm of Model (1b) was obtained from

analytical method, FDM and FEA at different application voltages and when compared in Figure 3.27, shows fairly close agreement.

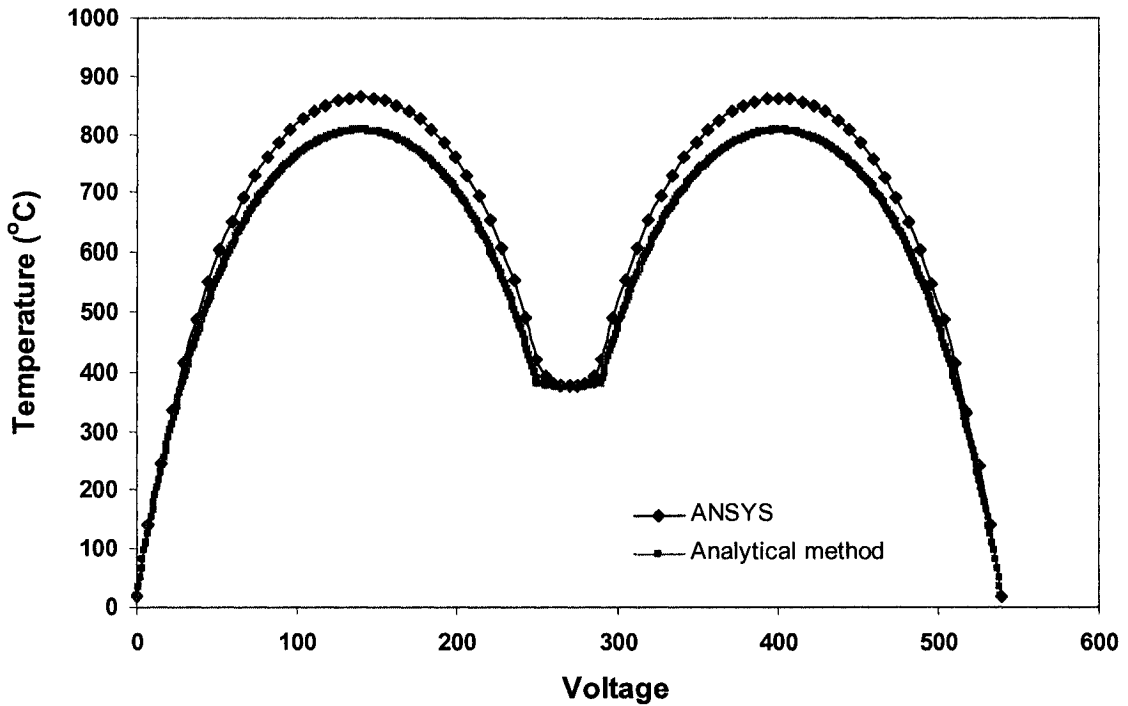


Figure 3.26: Temperature distribution of Model (1b) under the application of 12V or 3.9263mA

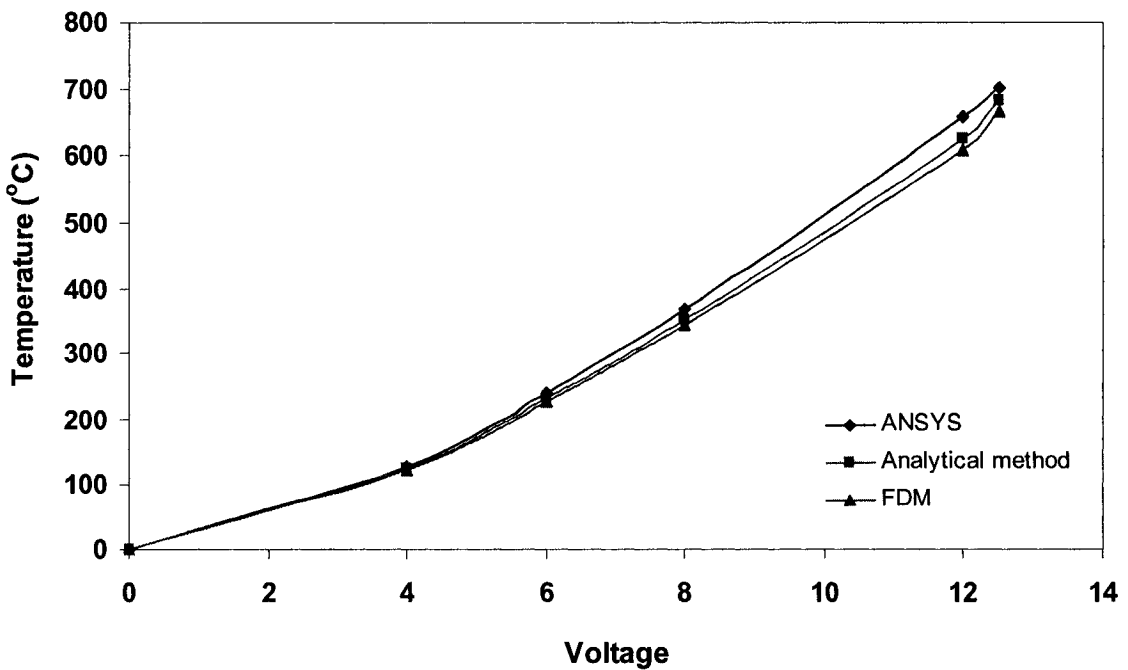


Figure 3.27: Average temperature of one hot arm of Model (1b) at different applied voltages

Rotation of the disc of Model (1b) was obtained from analytical method and FDM at different application voltages and when compared with that from FEA in Figure 3.28 shows close agreement. As the purpose of this thesis is to demonstrate the feasibility of the rotary actuator, hence this variation can be considered to be acceptable.

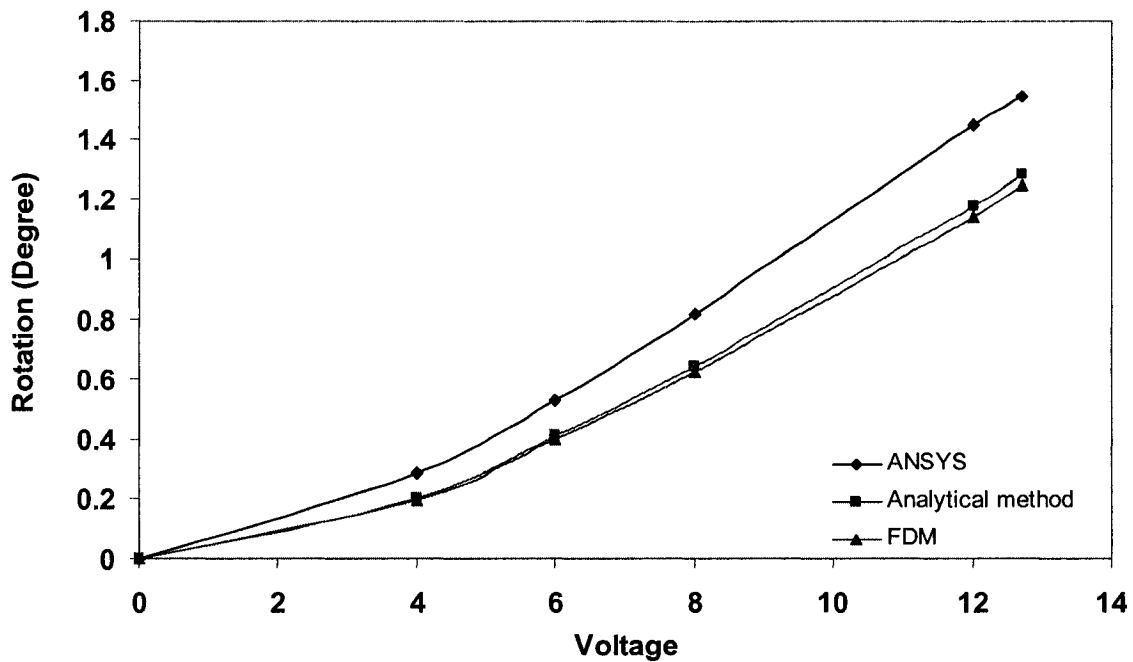


Figure 3.28: Rotation (in degrees) of the cold disc of Model (1b) at different applied voltages

Similarly, steady state temperature profile for Models (2a) and (2b) at 12V obtained from analytical method and FEA are compared in Figures 3.29 and 3.32 respectively and they show fairly close agreement. As discussed for Model (2a) and Model (2b) in Section 3.3, it is evident from Figures 3.29 and 3.32 that the maximum temperature of the beam in both the models, occur approximately in the half way of the beam length. Average temperature of a hot arm for Models (2a) and (2b) were obtained from analytical method, FDM and FEA at different application voltages and when compared in Figures 3.30 and 3.33 respectively, show fairly close agreement.

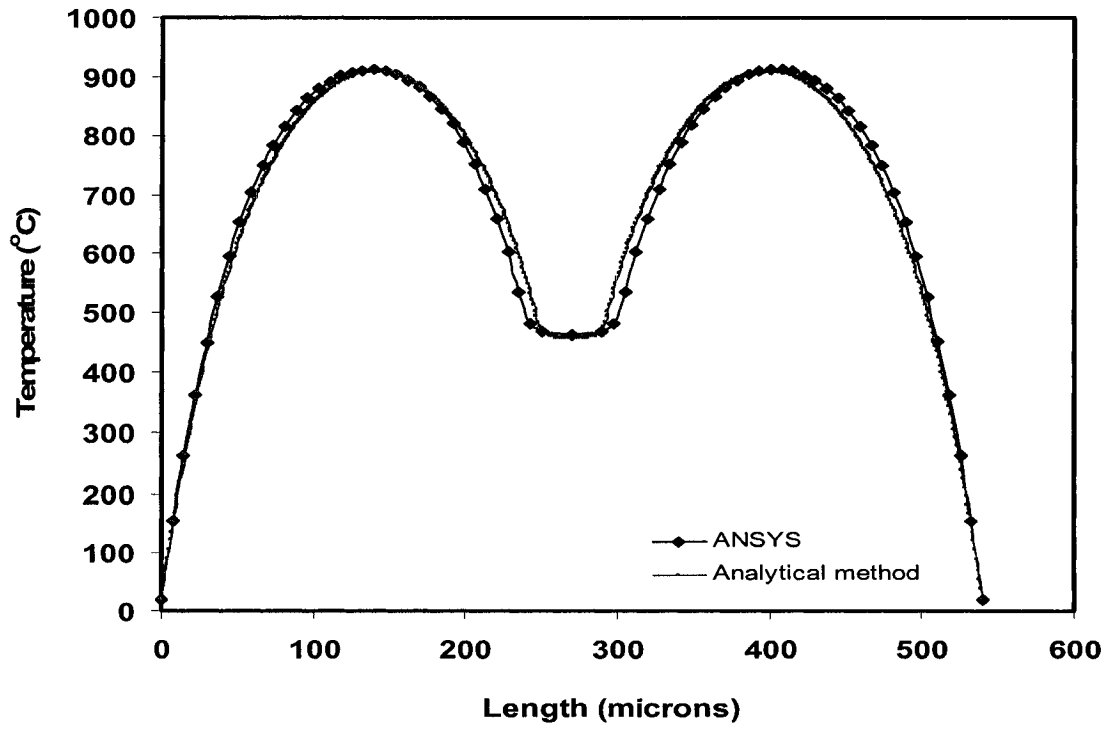


Figure 3.29: Temperature distribution of Model (2a) under the application of 12V or 4.0439mA

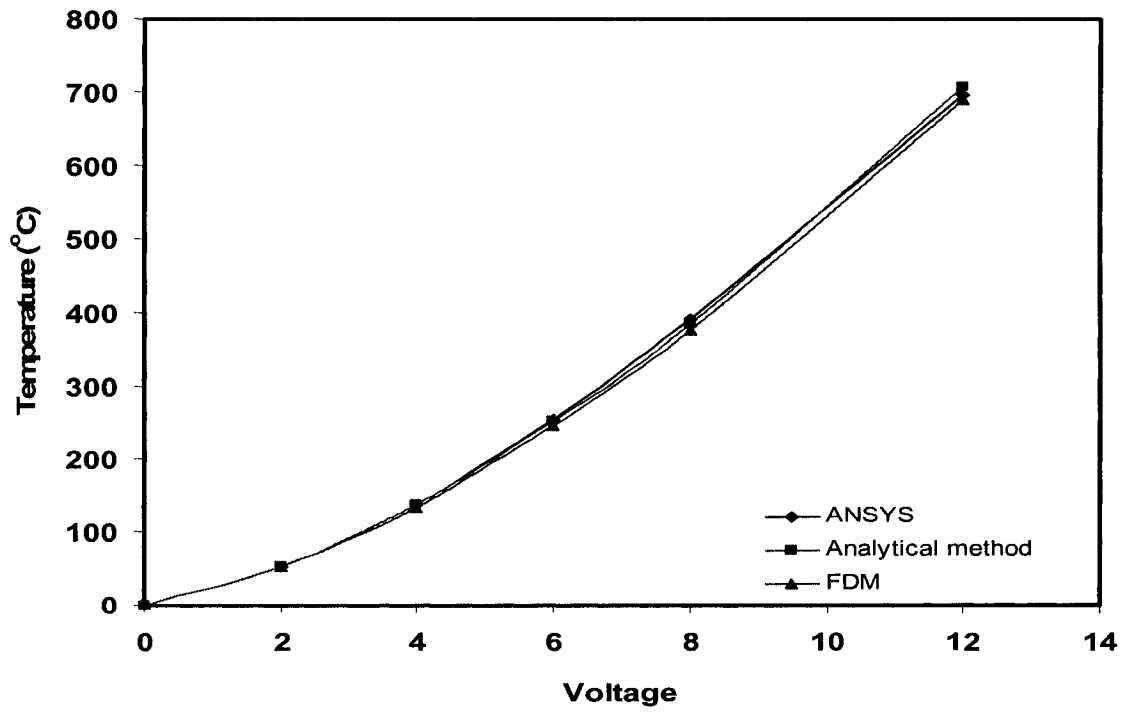


Figure 3.30: Average temperature of one hot arm of Model (2a) at different applied voltages

Rotation of the disc for Models (2a) and (2b) were obtained from analytical method and FDM at different application voltages and when compared with that from FEA in Figures 3.31 and 3.34 respectively, show close agreement.

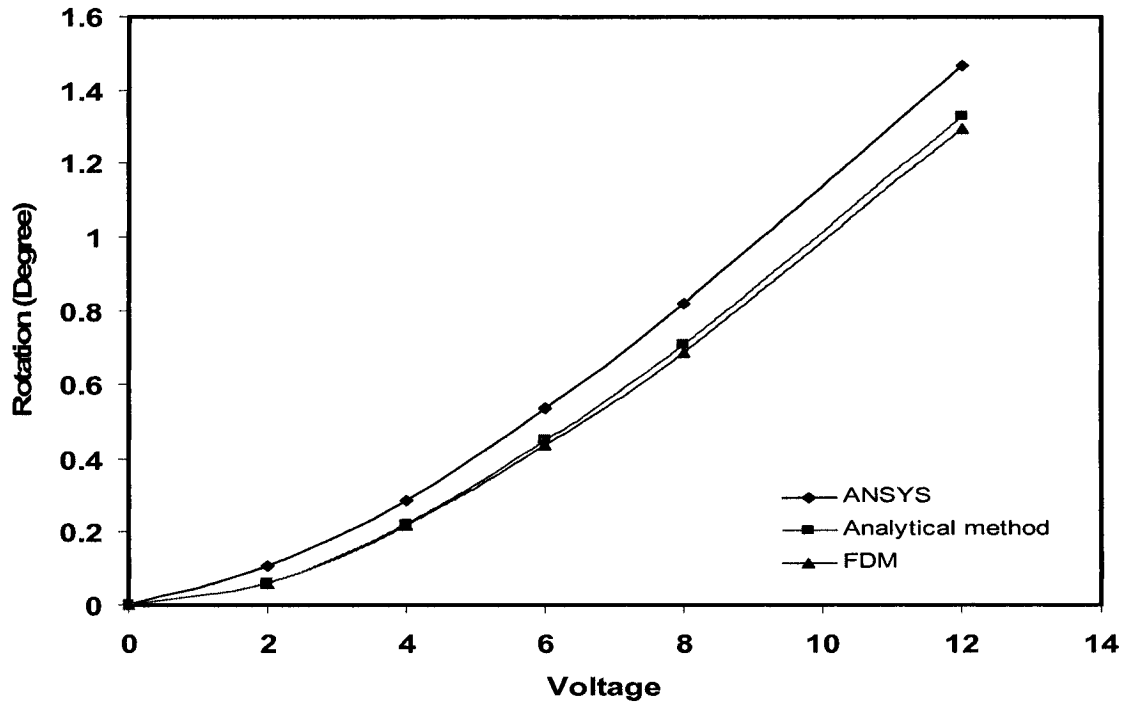


Figure 3.31: Rotation (in degrees) of the cold disc of Model (2a) at different applied voltages

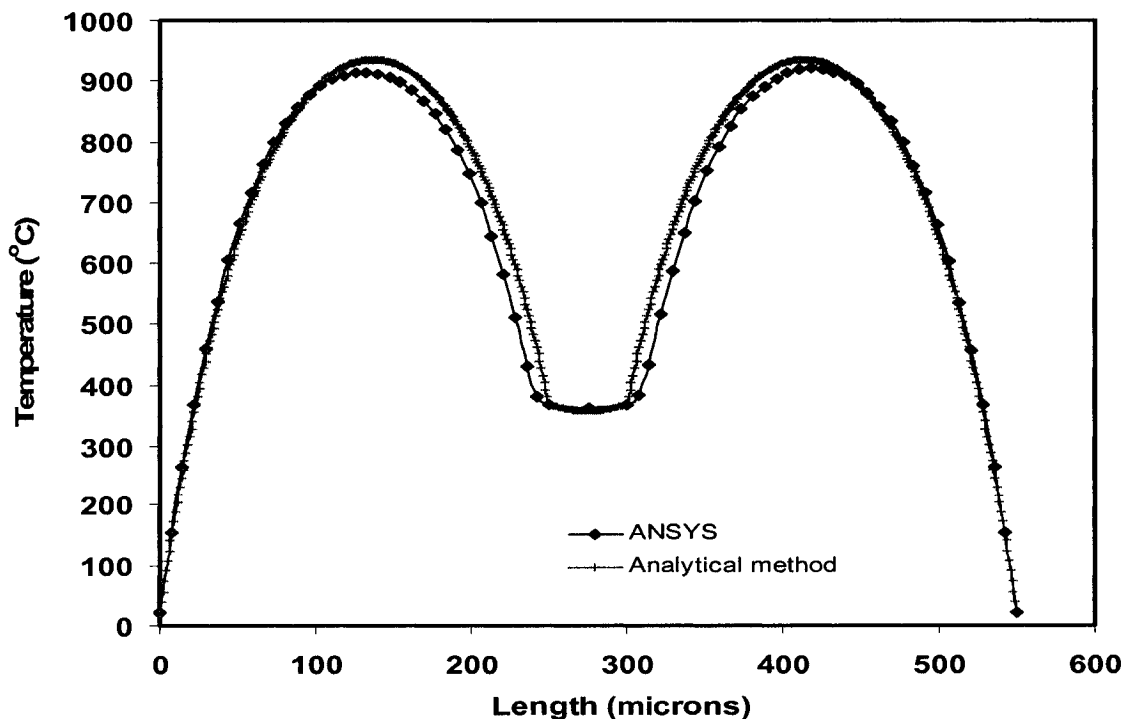


Figure 3.32: Temperature distribution of Model (2b) under the application of 12V or 4.0949mA

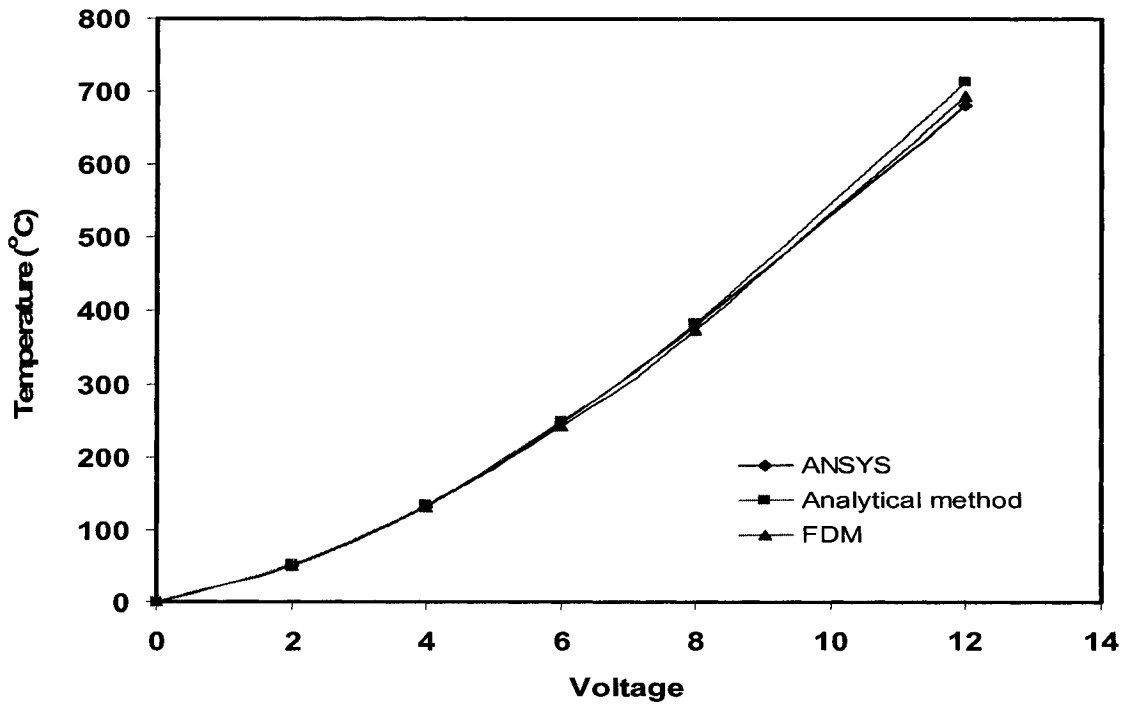


Figure 3.33: Average temperature of one hot arm of Model (2b) at different applied voltages

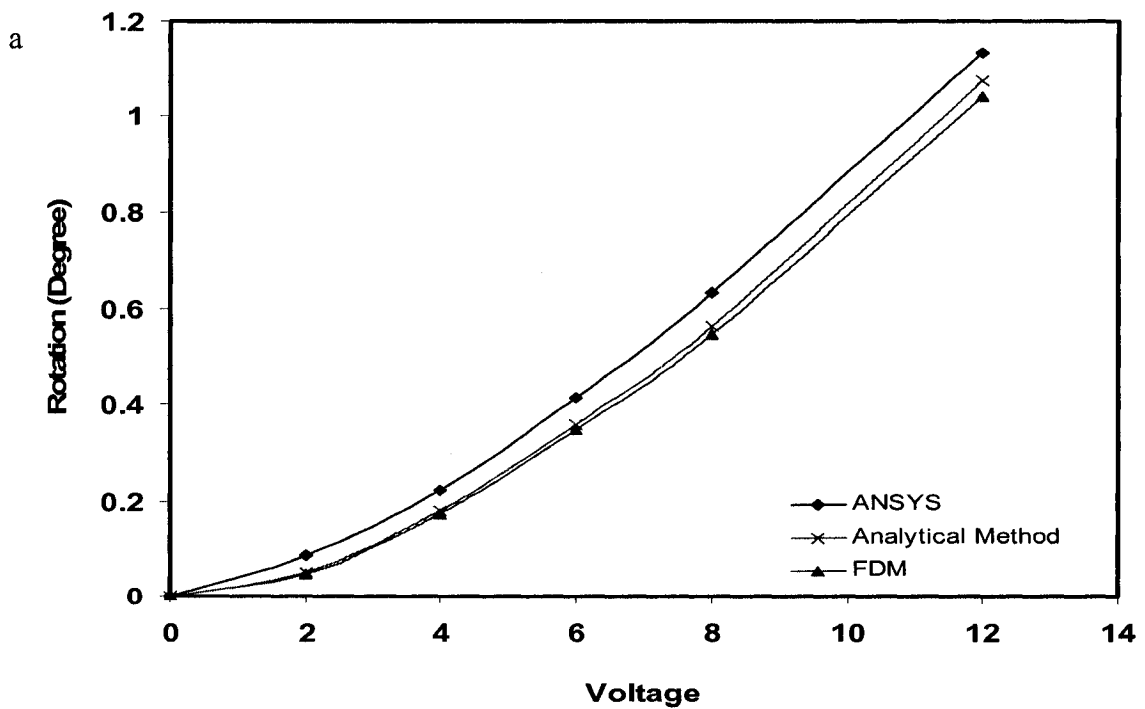


Figure 3.34: Rotation (in degrees) of the cold disc of Model (2b) at different applied voltages

Similarly, steady state temperature profile for Models (2c) and (2d) are obtained from analytical method at 16.5V and when compared with that from FEA in Figures 3.35 and 3.38 respectively, they show fairly close agreement. As expected maximum temperature of the beam for Models (2c) and (2d) occurs approximately in the half of the beam length. Average temperature of a hot arm of Models (2c) and (2d) were obtained from analytical method, FDM and FEA at different application voltages and when compared in Figures 3.36 and 3.39 respectively, they show fairly close agreement. Rotation of the disc of Models (2c) and (2d) were obtained from analytical method and FDM at different application voltages and when compared with that from FEA in Figures 3.37 and 3.40, show close agreement with some variation.

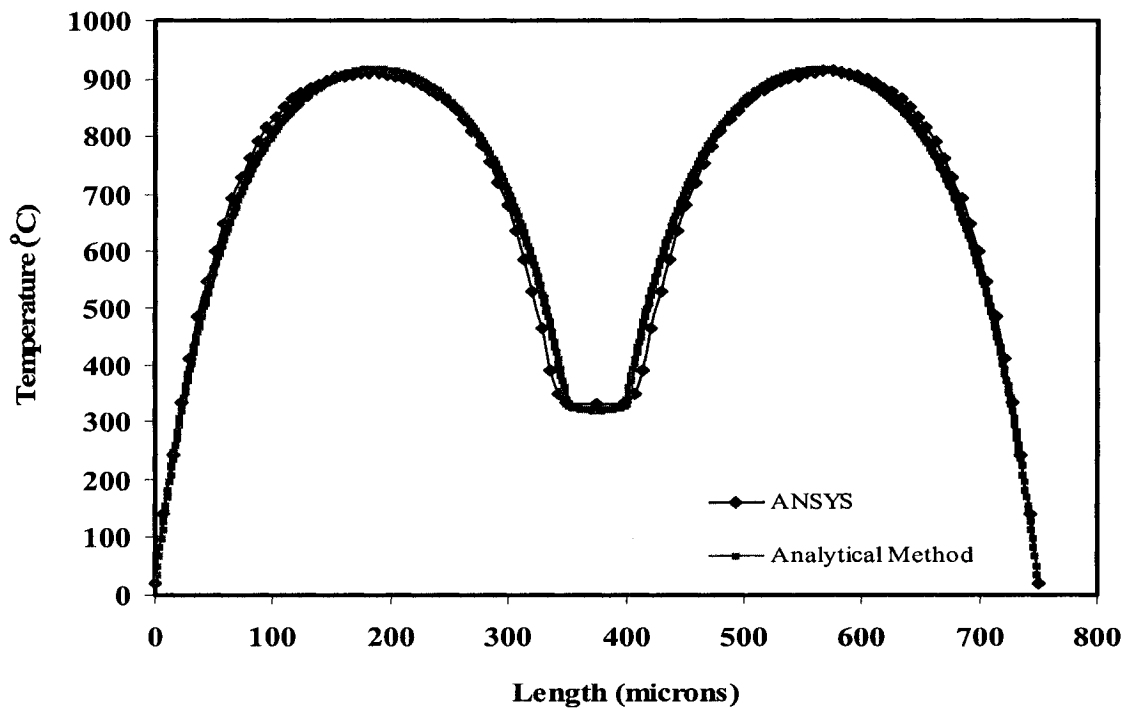


Figure 3.35: Temperature distribution of Model (2c) under the application of 16.5V or 3.93 mA

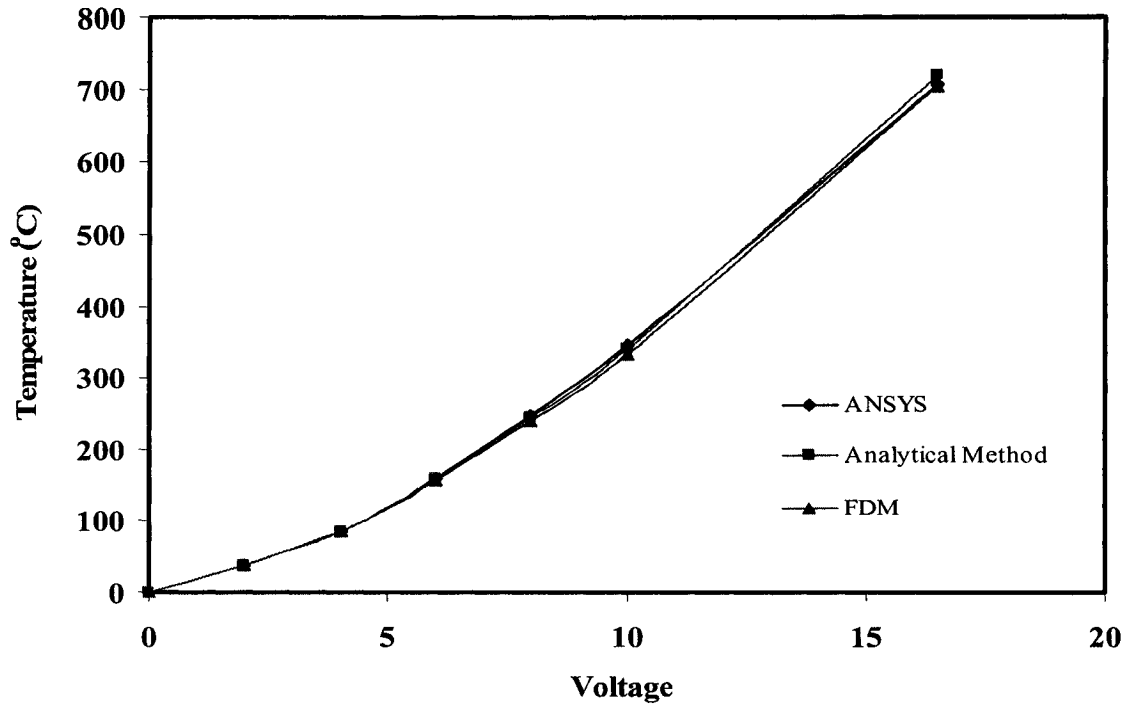


Figure 3.36: Average temperature of one hot arm of Model (2c) at different applied voltages

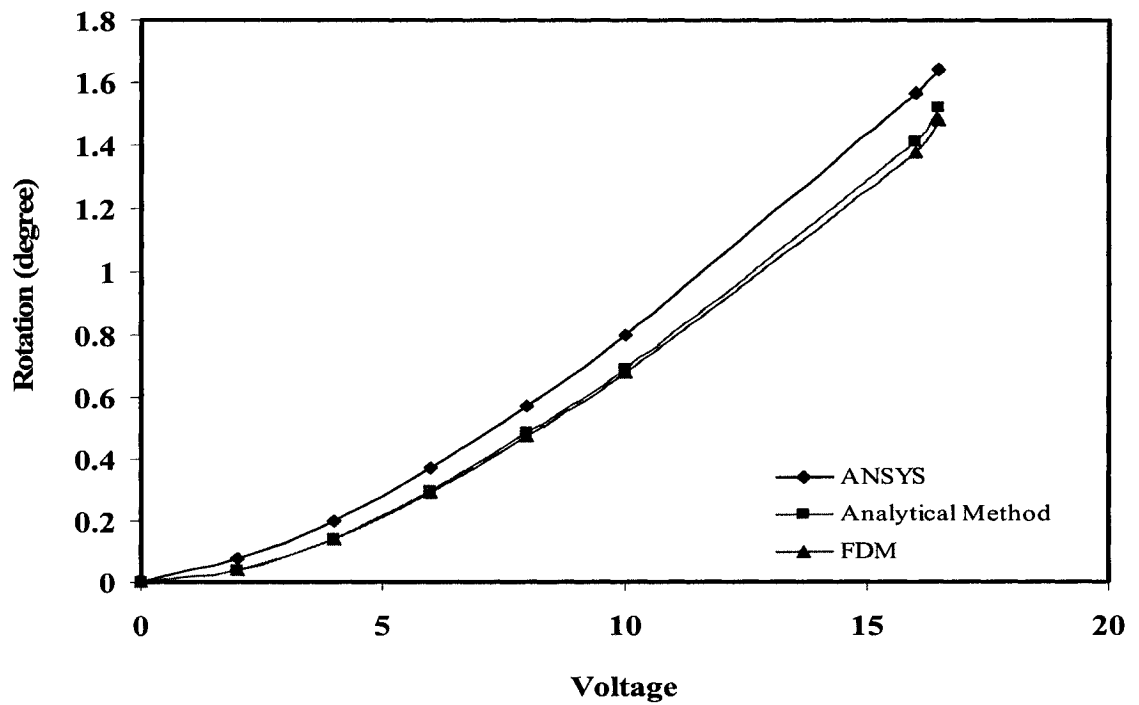


Figure 3.37: Rotation (in degrees) of the cold disc of Model (2c) at different applied voltages

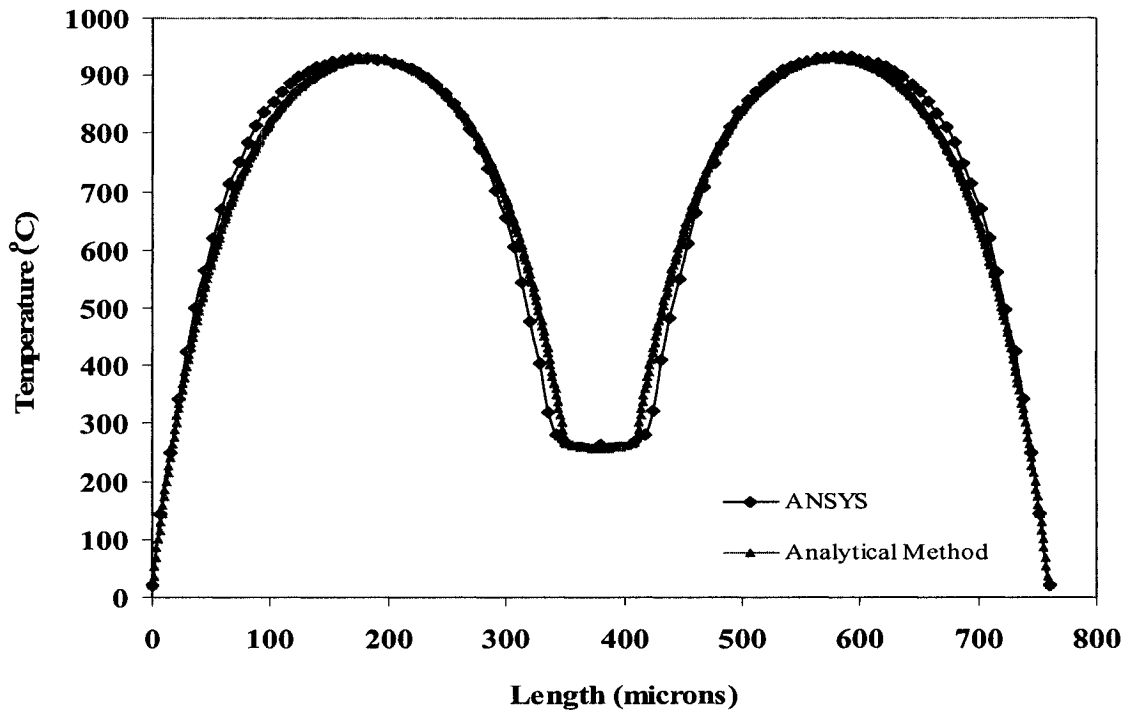


Figure 3.38: Temperature distribution of Model (2d) under the application of 16.5V or 3.9495 mA

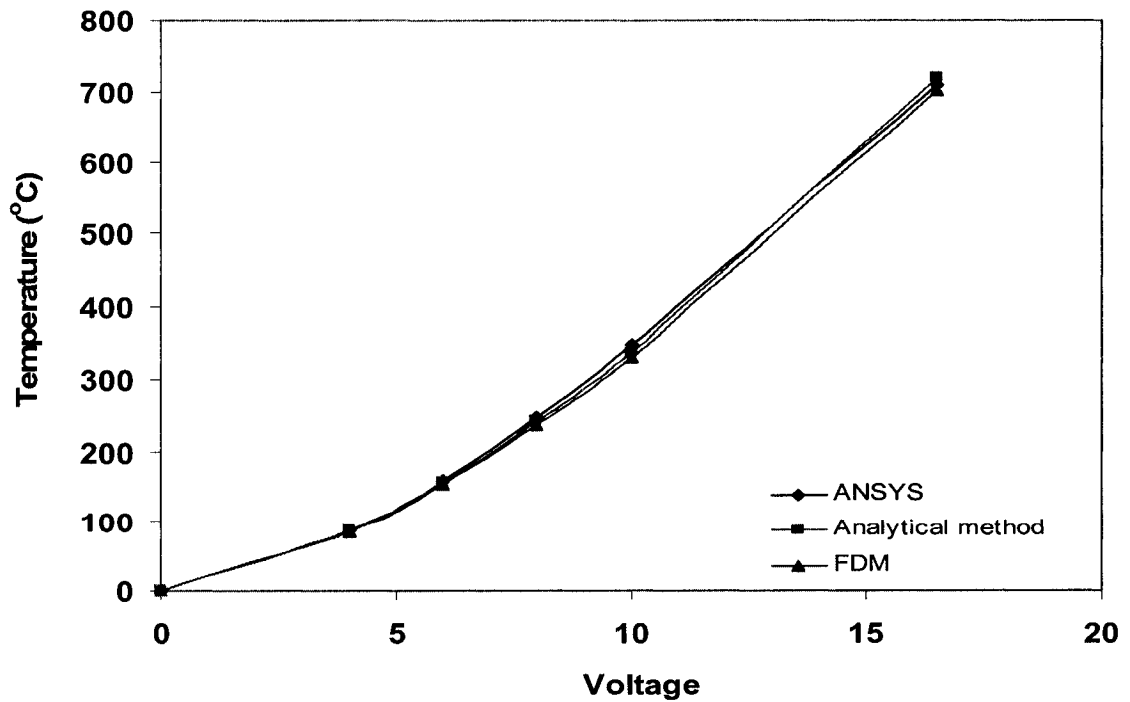


Figure 3.39: Average temperature of one hot arm of Model (2d) at different applied voltages

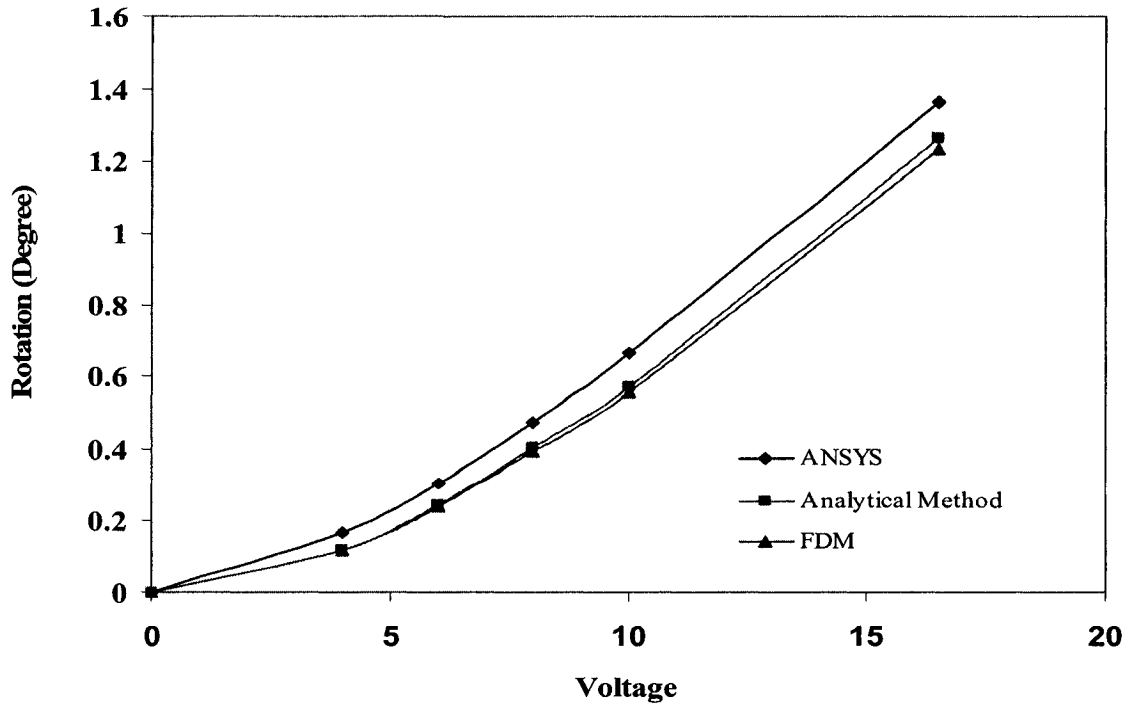


Figure 3.40: Rotation (in degrees) of the cold disc of Model (2d) at different applied voltages

Similarly, steady state temperature profile of Model (3) was obtained from analytical method at 20V and when compared with that of FEA in Figure 3.41, shows fairly close agreement. As expected the maximum temperature of the beam occurs approximately in the half way of the beam length. It may be noted that the disc temperature remains close to the room temperature of 20°C. This is due to the fact that Model (3) has a large disc which in turn works as heat sink in addition to the surrounding. For this same reason the maximum temperature of a hot arm even at higher application voltage than used for previous models, is fairly low compared to previous models even though Model (3) has larger beam length. Average temperature of a hot arm of Model (3) was obtained from analytical method, FDM and FEA at different application voltages and when compared in Figure 3.42, shows fairly close agreement.

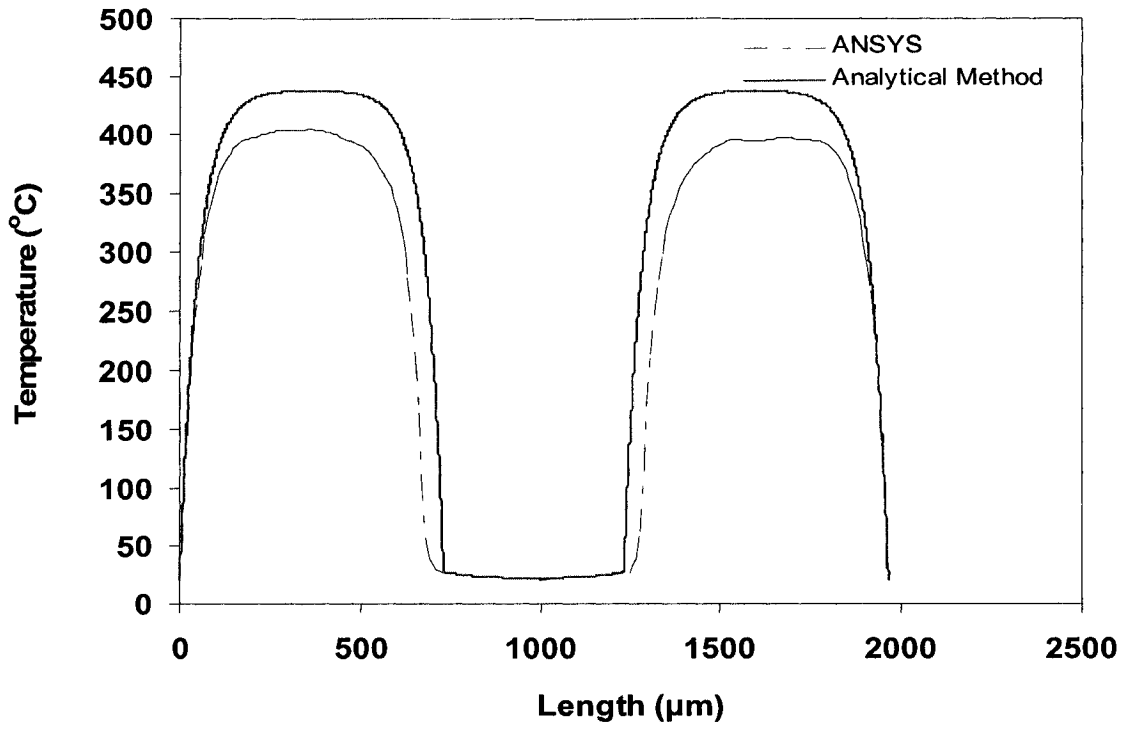


Figure 3.41: Temperature distribution of Model (3) under the application of 20V or 3.1004mA.

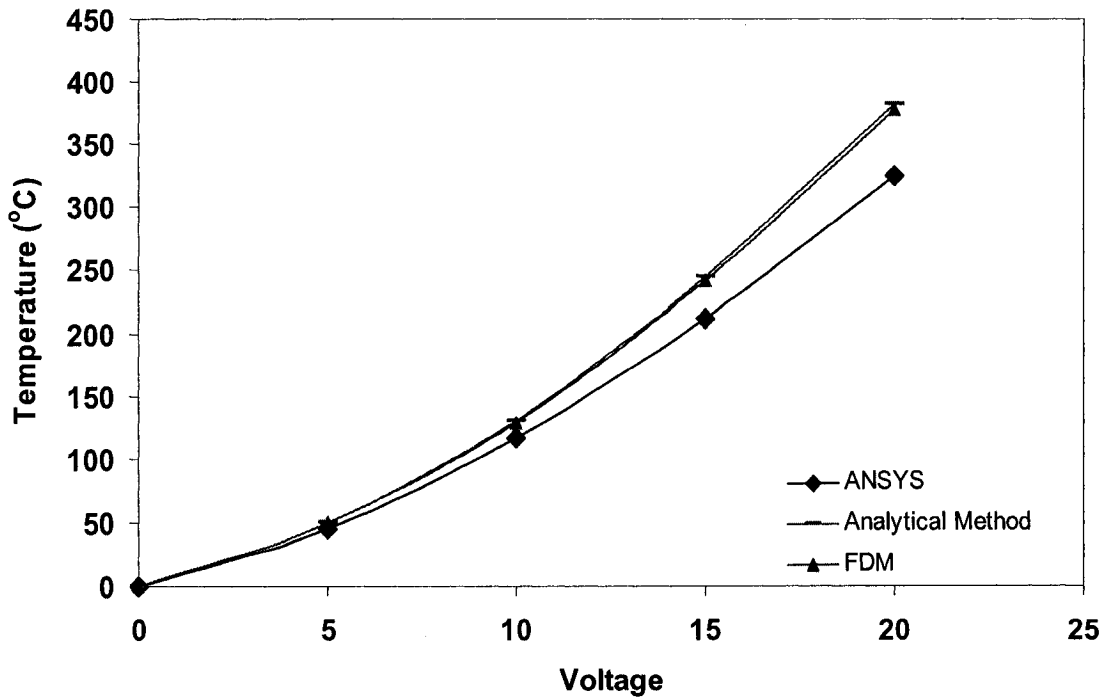


Figure 3.42: Average temperature of one hot arm of Model (3) at different applied voltages

Rotation of the disc of Model (3) was obtained from analytical method and FDM at different application voltages and when compared with that from FEA in Figure 3.43 shows close agreement.

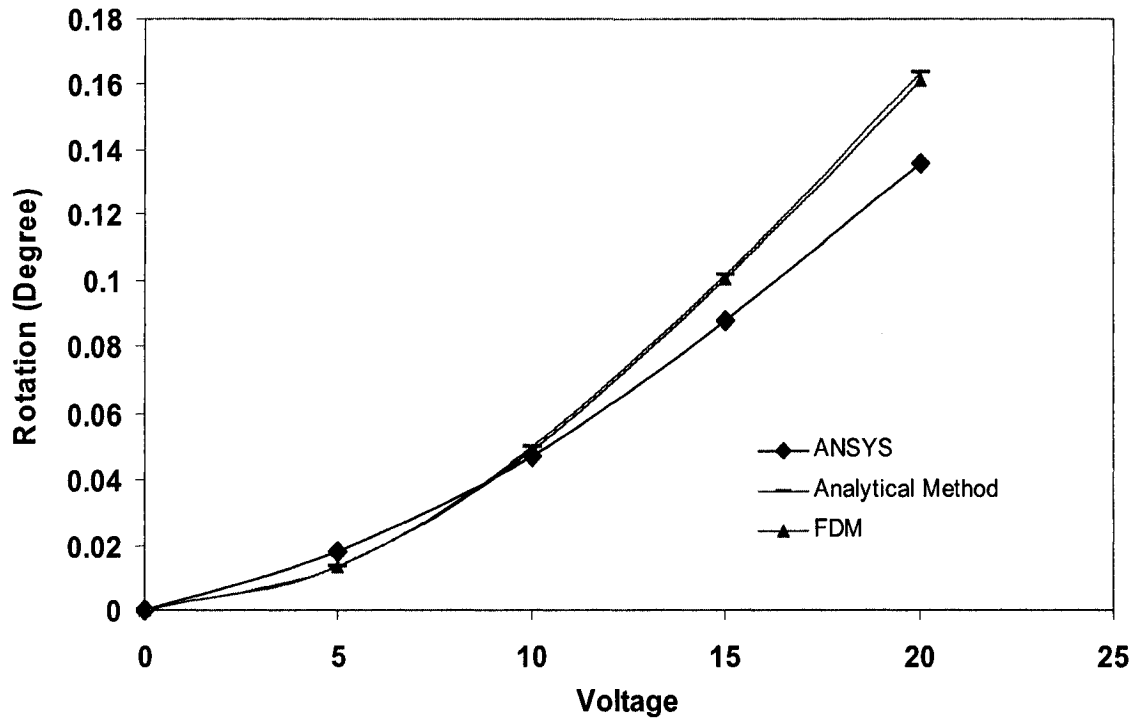


Figure 3.43: Rotation (in degrees) of the cold disc of Model (3) at different applied voltages

3.6 Parametric Analysis

Dimensional variations of topology configurations and different loading conditions effect the behavior of a thermal actuator. So, parametric analysis is very important to determine the conditions that yield desired rotation. Hence, various design methodologies are presented below:

Number of arms effects rotational behavior of the actuator. Rotational behavior of the disc obtained in ANSYS for Model (1a) and Model (1b) is compared in Fig. 3.44 and it is

found that an additional pair of arms in Model (1b) than Model (1a) slightly increases rotation of the disc.

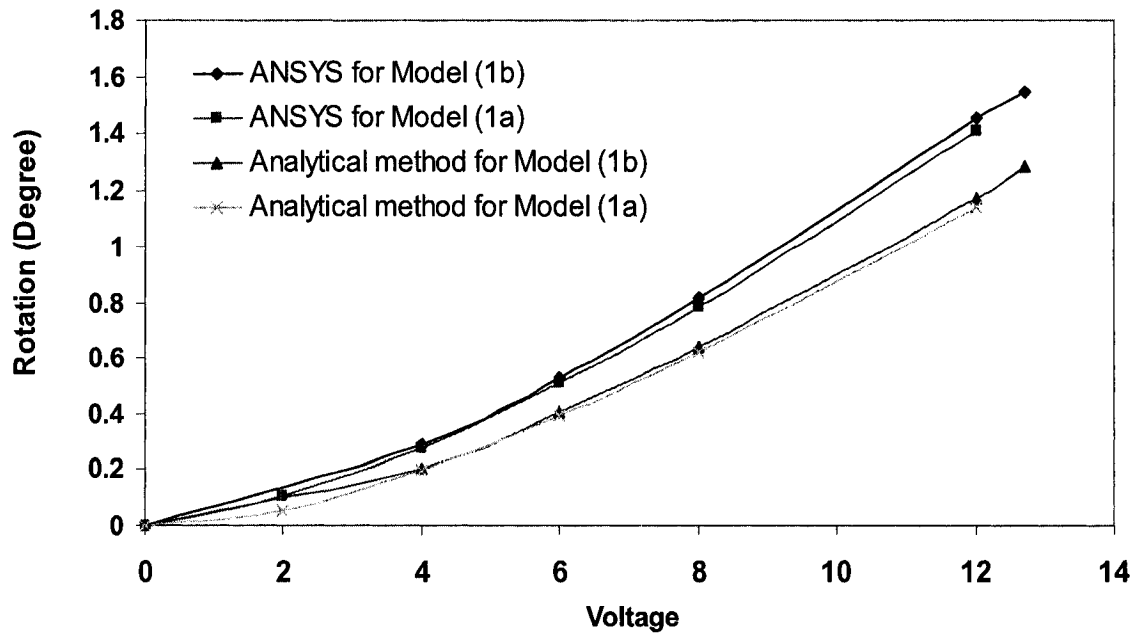
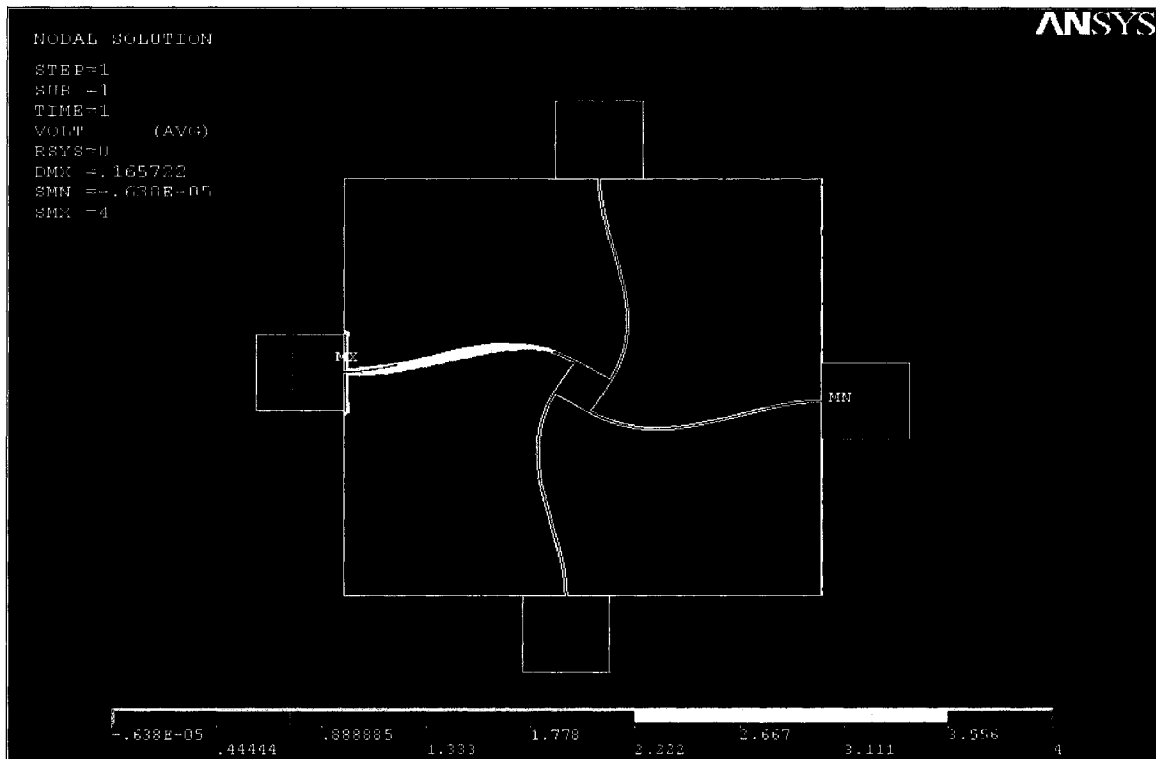


Figure 3.44: Effect of omission of a pair of arms in Model (1)

Also, different loading conditions in a given design topology effect rotational behavior of the actuator. In a 4-arms actuator design, following two different loading conditions are considered:

1. Condition (1): all the pair of arms are loaded with potential difference i.e. voltage is applied on two anchor pads and another two pads are made as ground. Analysis and results presented so far for 4-arms actuator design, are based on this loading condition.

- Condition (2): only a pair of arms is loaded with potential difference i.e. voltage is applied on a single anchor pad and another single pad is made as ground. Other two anchor pads are kept as open circuit. Following Figure 3.45 shows such a loading condition.



It is found that Condition (1) provides more rotation of the disc than the Condition (2) as shown in Figure 3.46. This is due to the fact that in the latter case the left pair of arms introduces resistance to the motion of the disc. Model (1b) is considered for this study and the result is shown in the following Figure 3.46.

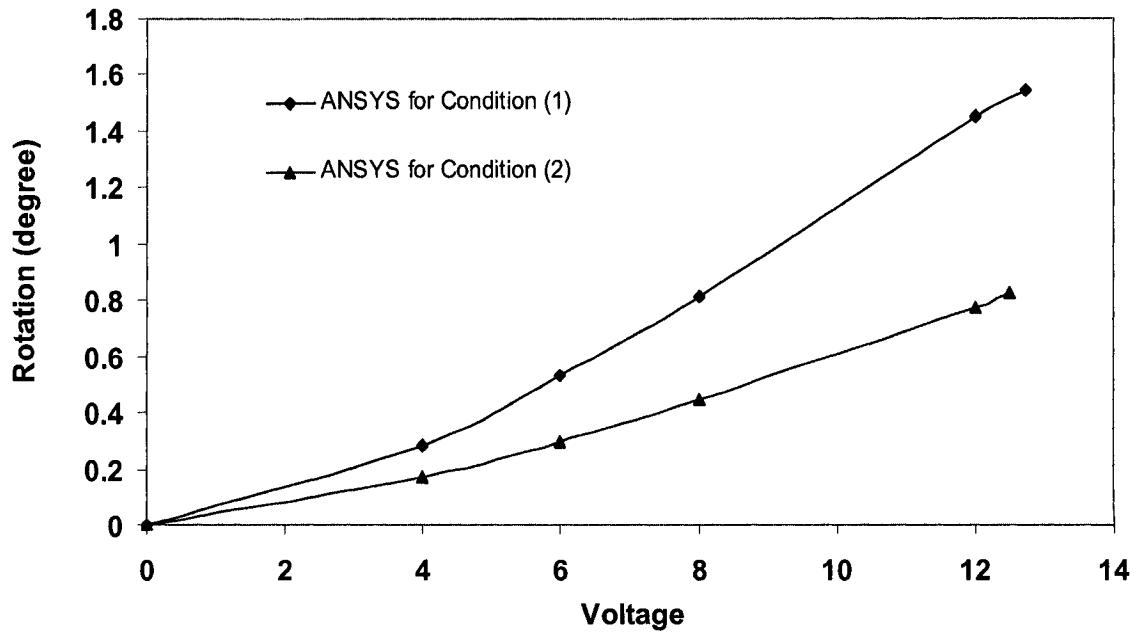


Figure 3.46: Effect of loading 2 arms in Model (1b) with different potentials

Dimension also has significant effect on the rotational behavior of the actuator and thus needs to be optimized for maximum rotation. For the same beam length and input current, rotation of the disc increases inversely with radius of the disc. This is due to the fact that the smaller the radius the more heat is contained in the structure which results in increased rotation. Comparison of rotational behavior of Model (2a) and (2b) in Figure 3.47, shows close agreement

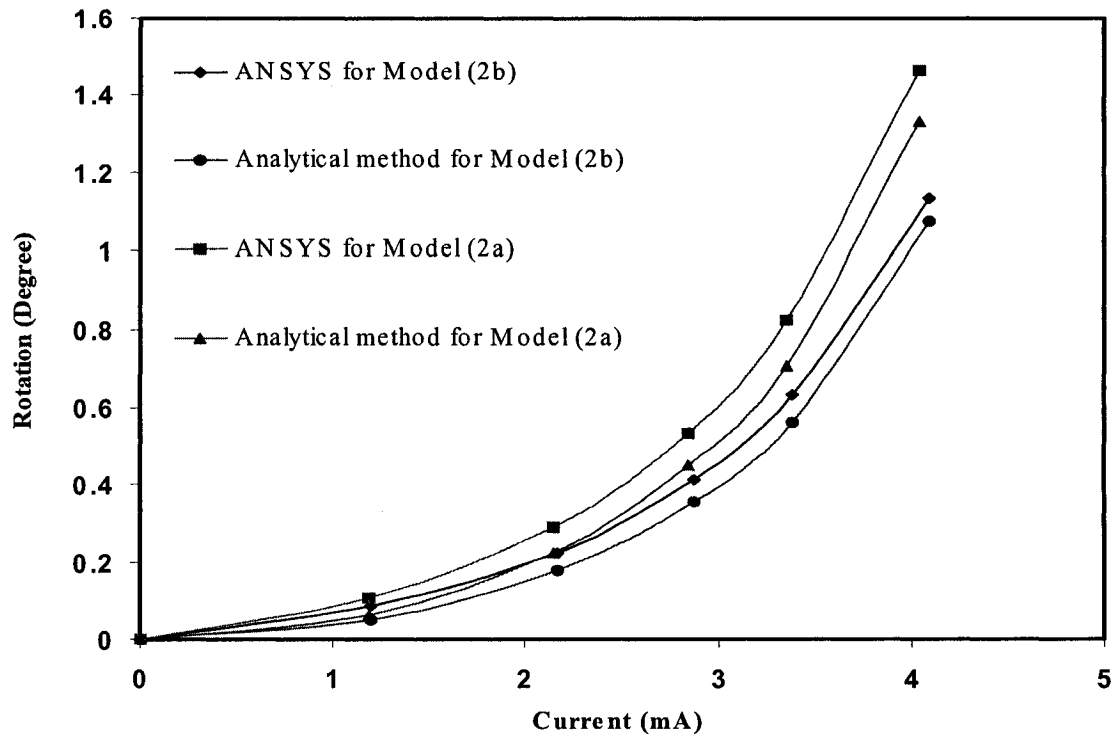


Figure 3.47: Effect of radius on the rotational behavior of the disc

On the other hand, with the same disc radius and input current, rotation of the disc increases proportionally with the beam length. Increasing beam length generates more heat in the structure which results in increasing rotation. Comparison of rotational behavior of Model (2a) and (2b) in Fig. 3.48, shows this.

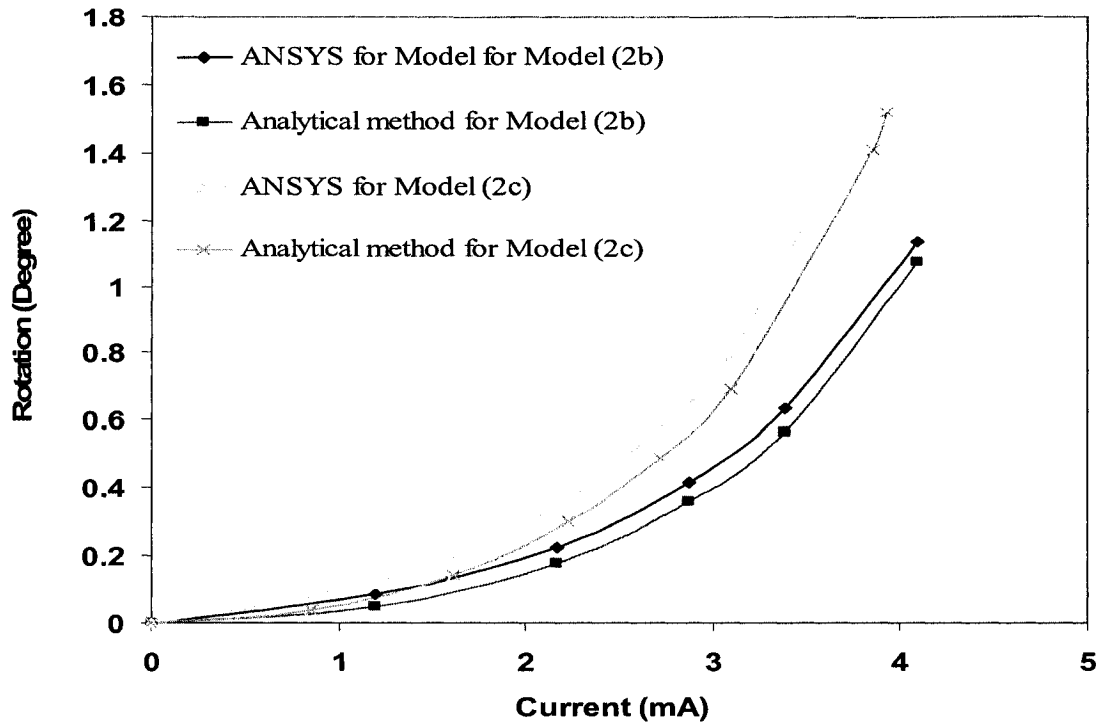


Figure 3.48: Effect of beam dimension on the rotational behavior of the disc

Design trials based on the dimensional adjustment has limitations. Fabrication technologies could have restrictions for minimum and maximum allowable feature size. Big features supported by narrow large beams could cause sagging on the substrate due to weight. Gap between the structure and substrate is very important for the operation of micro electro thermal actuator fabricated by MUMPS. Besides, designing a large beam is also restricted by the melting point of the structure material.

When space is limited a curved beam topology could be solution because this offers smaller foot-print of the device. As a result this topology could be the choice for a fully integrated physical system. For the same foot-print curved beam topology can provide larger rotation than that of straight beam which is shown in the following. For the curved

beam topology Model (3) of Chapter 3, along with its associated results are considered.

Dimensions of the straight beam topology of same foot-print, Model (2e) is given below.

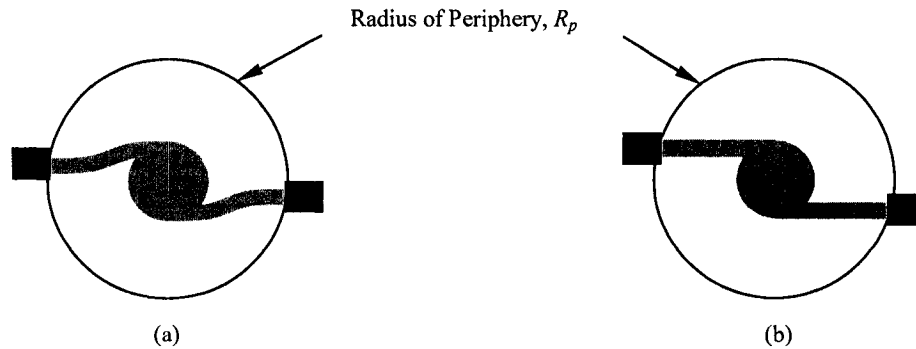


Figure 3.49: (a) Model (3), Schematic of rotary type micro thermal actuator with curved beam, (b) Model (2e), Schematic of rotary type micro thermal actuator with straight beams

Table 3.4: Models used for a given foot-print analysis

Model	l_h (μm)	R (μm)	R_p (μm)
3	732	250	673
2e	625	250	673

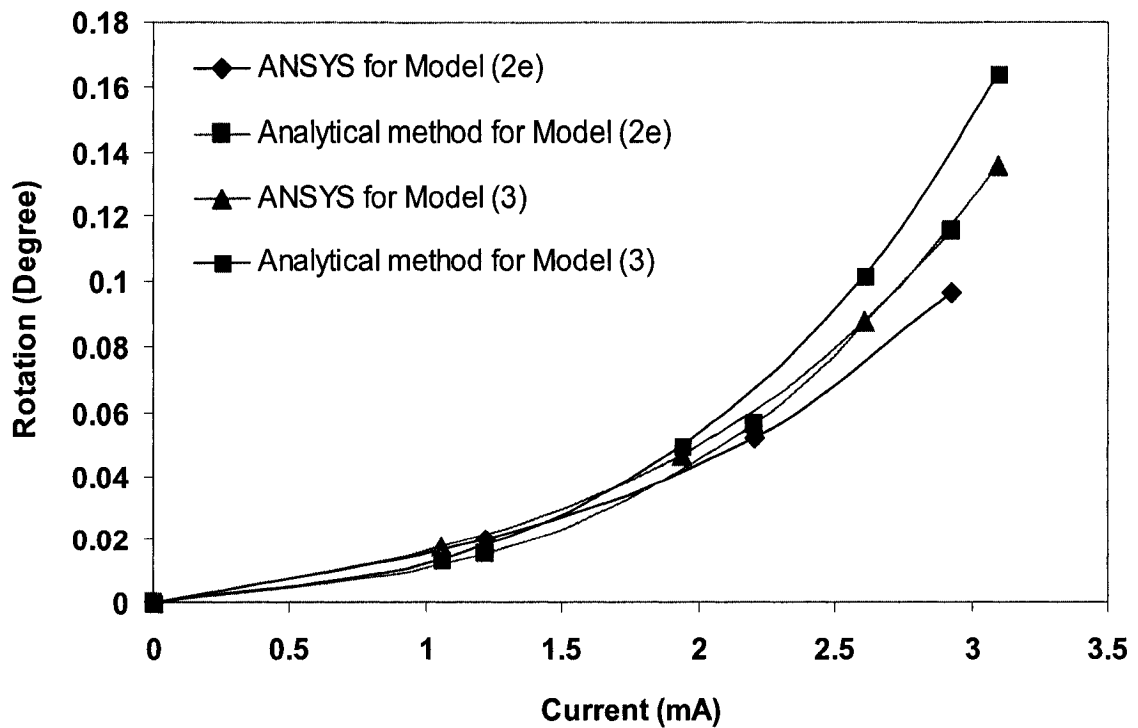


Figure 3.50: Comparison of rotational behavior of Model (3) and Model (2e) as a function of input current

The parametric analysis will help in choosing appropriate dimension of the device for fabrication.

Chapter 4

Experimental Testing

4.1 Experimental Scheme

The rotary type micro thermal actuators proposed in this investigation have been fabricated using MUMPS technology. The whole structure is realized out of one polysilicon layer namely Poly1. The proposed designs and fabricated proto type were presented in Chapter 2. Rotation of the disc is measured from the relative position of the outline of the structure before and after the application of load as shown in Figure 4.1. To facilitate this, picture of the device before and after loading was taken and relative rotation of the disc was estimated.

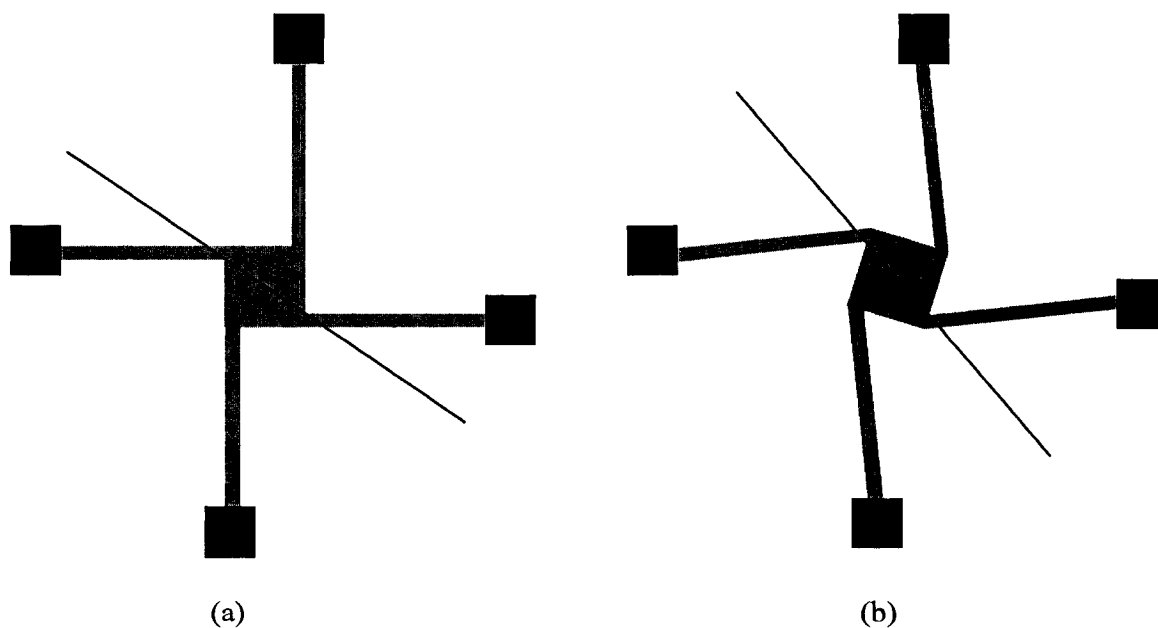


Figure 4.1: Outline for rotation measurement for a rotary thermal actuator. A reference line is drawn in (a) before applying load and (b) after applying load.

Equipments that were used for the experiment are a DC power supply with tuning range up to 25V, 2 multimeters- one for the record of potential applied across the device and

the other one for the record of current supplied, a microscope, CCD camera and computer for grabbing pictures and videos and post processing. The chip was positioned under the microscope with the CCD camera mounted on it. Block diagram for the experimental setup is shown in Figure 4.2. The voltage and current measurement scheme across the arm of the device is shown in Figure 4.3.

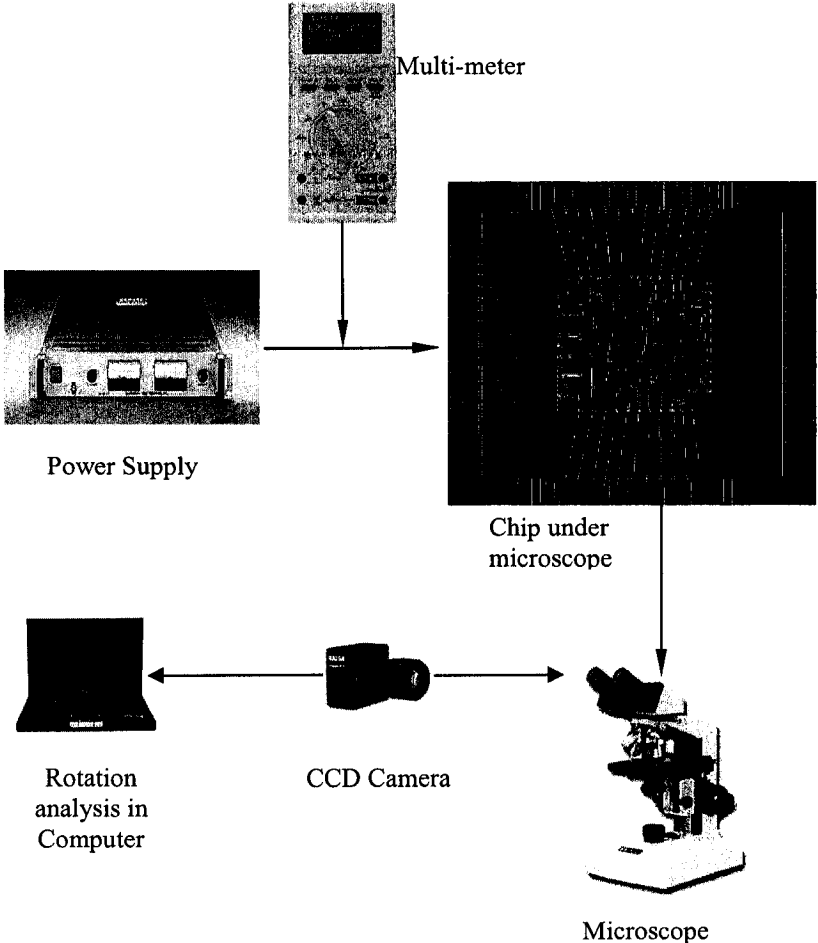


Figure 4.2: Block diagram for the experimental setup

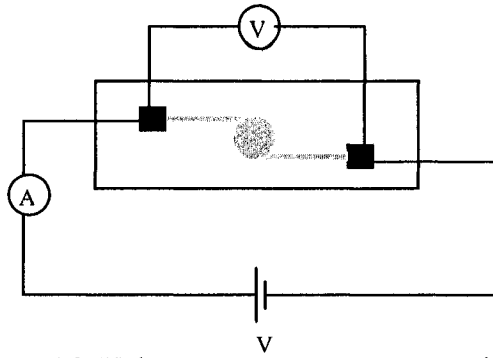


Figure 4.3: Voltage-current measurement scheme

Figure 4.4 shows a photograph of the actual measurement setup with all the equipment used.

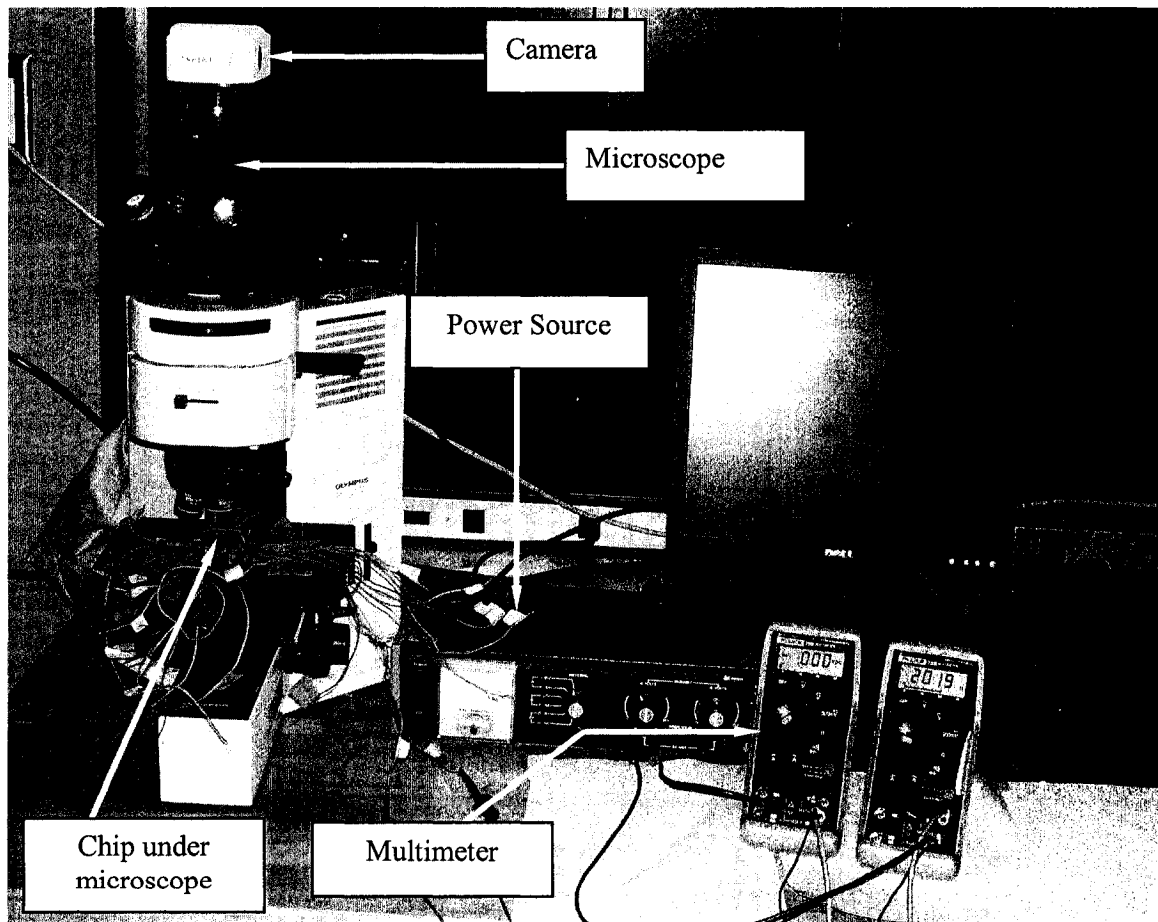


Figure 4.4: Experimental setup for measuring rotation of the rotary type micro thermal actuator

4.2 Experimental Results and Discussion

Experiments were carried out on different designs, namely, Design (1a), (1b) and (2). Criterion that are used for the validation of the theoretical models with the experimental results are-

1. Location of highest temperature along the beam length.
2. Comparison of I-V characteristics curve obtained from both the theoretical models and experiments.
3. Comparison of rotation of the disc obtained from both the theoretical models and experiments.

The following sections detail the experimental validation on Design (1a), (1b) and (2).

4.3.1 Validation for Design (1a)

The highest temperature on the actuator is identified by observing for hot spot along the length of the beams. During the experiment, the hot spot could be easily identified as glowing spot along the beam as shown for Design (1a) in Figure 4.5. This can be compared with the temperature solution of Design (1a), obtained using FEA as shown in Figure 3.9. Both the experimental and FEA results show that the highest temperature is generated approximately at the midsection of the beams.

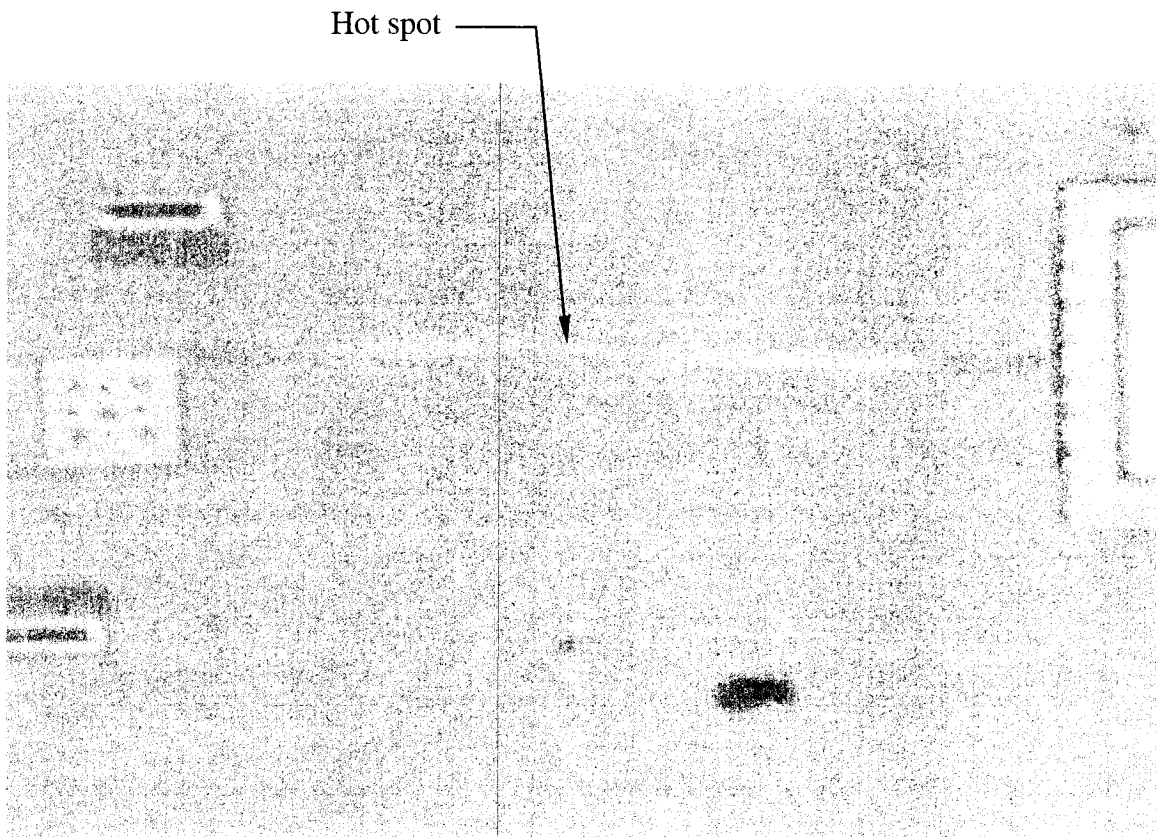


Figure 4.5: Appearance of hot spot i.e, maximum temperature in the beam

The experimentally measured variation in current with the voltage (I-V characteristics) for Design (1a) is presented in Figure 4.6 along with those obtained for the design using analytical method and ANSYS. As the results show, the experimental value of current as a function of voltage increases some what rapidly than those predicted by model simulations. This can be attributed to the fact that the resistivity of Polysilicon1 in the simulations are taken as 2×10^{-3} ohm-cm for standard dopant level from literature [38, 39, 44], and is for room temperature. It is thus possible that the actual resistivity under load is less than those reported at room temperature. Further more, there are etch holes on the cold disc from fabrication and are not included in analytical and ANSYS simulation.

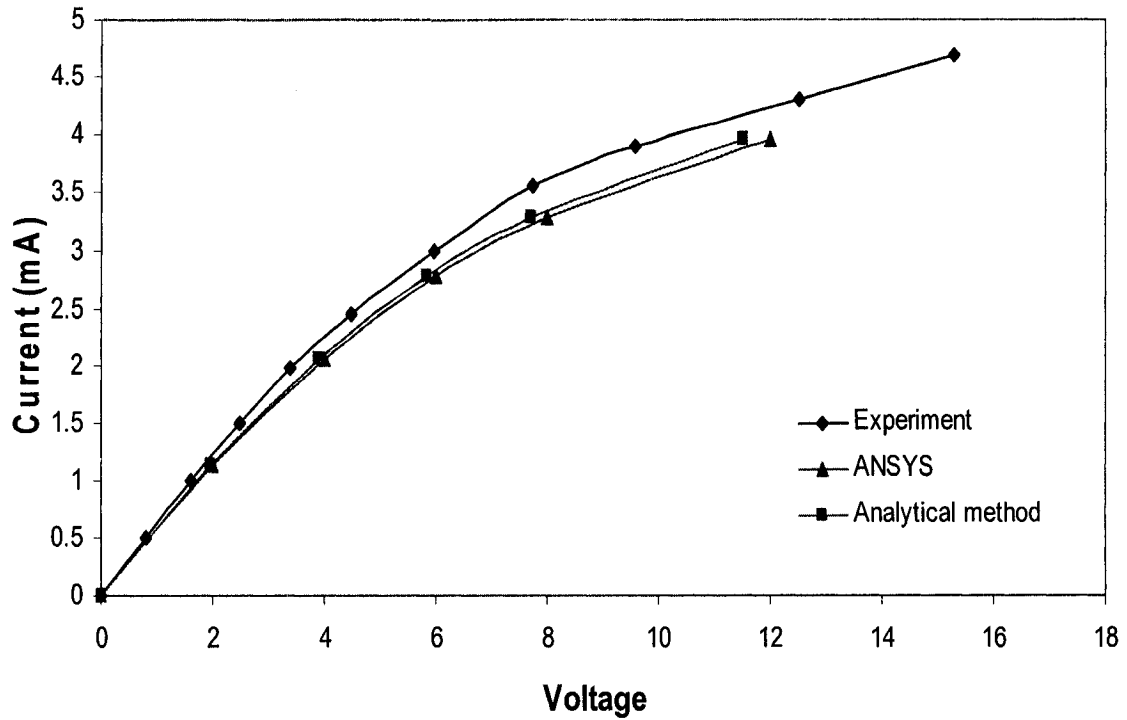


Figure 4.6: I-V Characteristics curve for Design (1a) with $\rho_0 = 2 \times 10^{-3}$ ohm-cm

Resistivity of Polysilicon1 is tuned in such a way that I-V characteristics curve from both analytical method and ANSYS match with that from the experiment. After tuning, the resistivity for Design (1a) was found to be 1.75×10^{-3} ohm-cm. The comparison of the tuned I-V characteristics is shown in Figure 4.7. Based on this new resistivity rotational behavior from various methods is compared with the experiment.

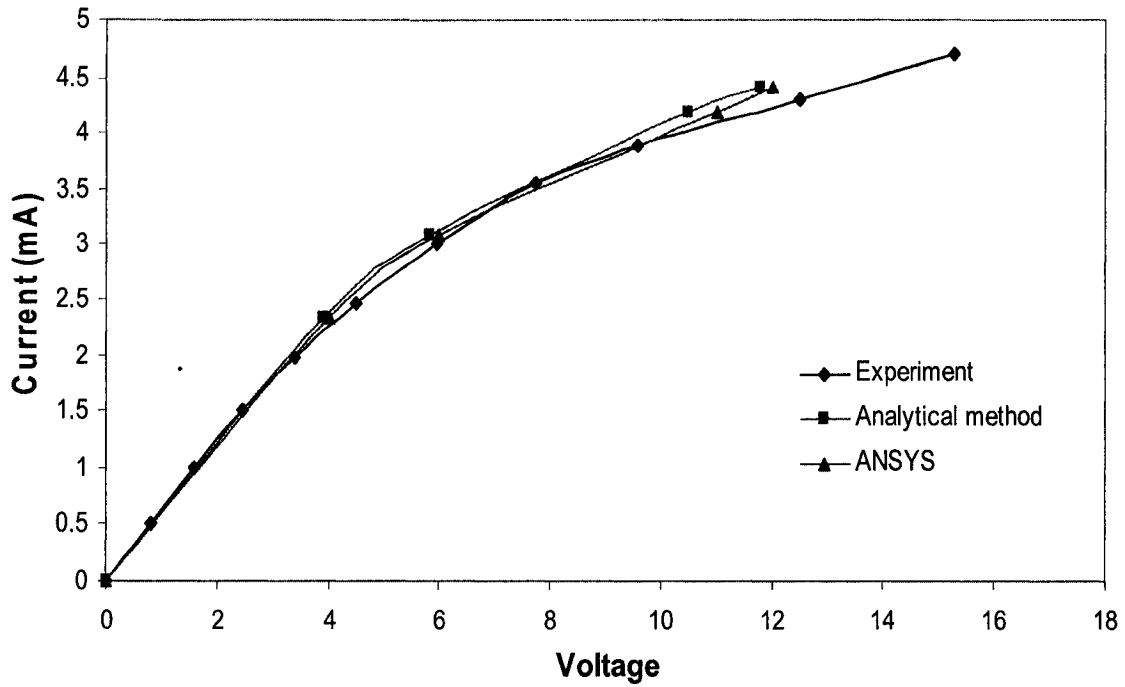


Figure 4.7: I-V Characteristics curve based on tuned resistivity for Design (1a) with $\rho_0 = 1.75 \times 10^{-3}$ ohm-cm

In order to estimate the angle of rotation for the device, a reference line on the disc in photographs taken before and after application of voltage was used as discussed earlier. New actuator rotates upon application of 15.29V. The before and after photograph of Design (1a) for application of 15.29V, is shown in Figure 4.8. The rotation angle estimated from this result is 2.28 degrees. Error in measurement is expected to be less than 2%.

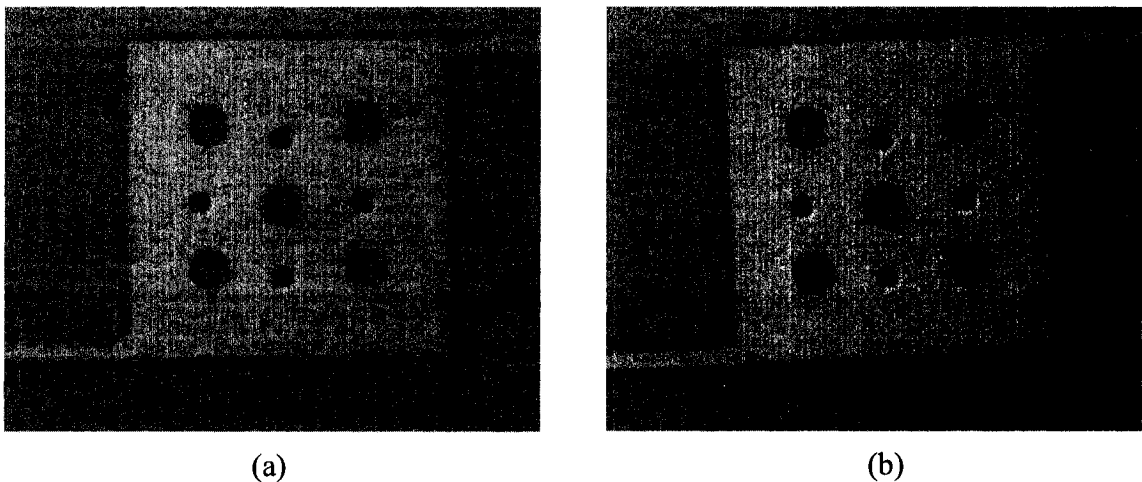


Figure 4.8: (a) Picture of the disc taken before applying voltage and (b) picture of the disc taken after application of 15.29V.

Further results used for estimation of rotation angle corresponding to other voltages are presented in Appendix-B. The experimentally observed rotational angle along with those predicted by analytical and ANSYS simulations are presented in Figure 4.9. The results show excellent agreement with those predicted using analytical model specially for low voltages. As the voltage is increased beyond 10Volts, the experimental rotation is slightly lower than those predicted by analytical method, but are more close to the motion predicted by ANSYS.

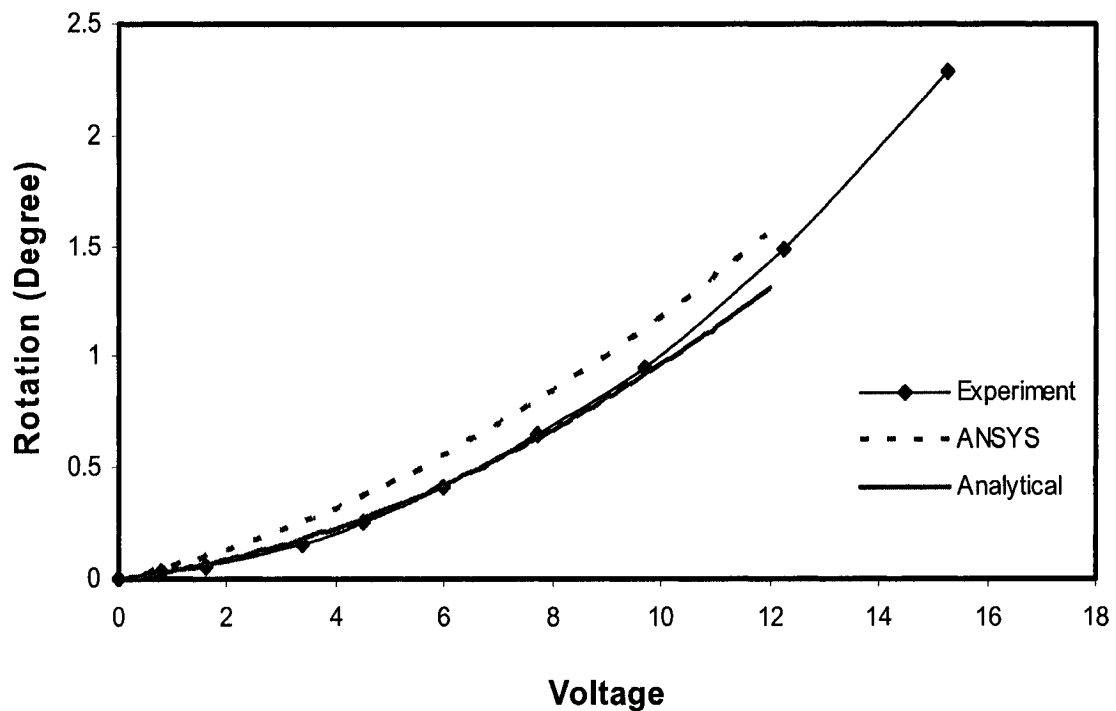


Figure 4.9: Variation of rotation against the applied voltages for Design (1a)

4.3.2 Validation for Design (1b)

Similar to design (1a), the I-V characteristic curve for Design (1b) is presented in Figure 4.10. A comparison of analytical and ANSYS results with those of experiment show similar trend as those observed for Design (1a). The deviation is again attributed to the uncertainty in the value of resistivity.

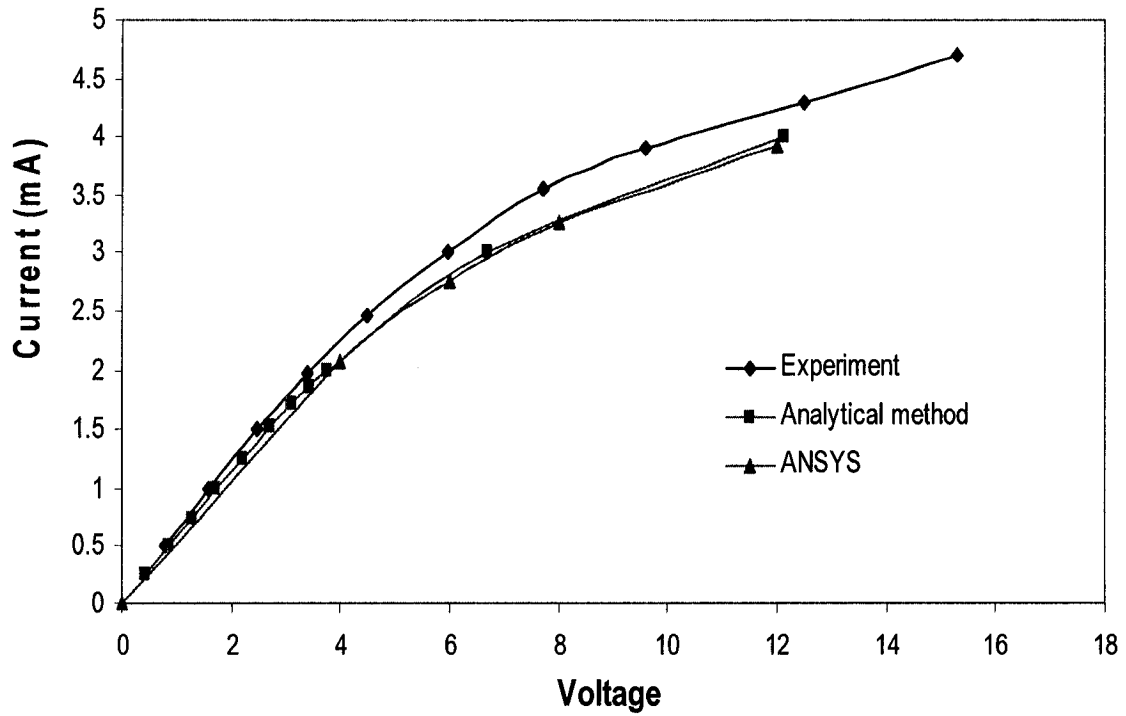


Figure 4.10: I-V Characteristics curve for Design (1b) with $\rho_0 = 2 \times 10^{-3}$ ohm-cm

Tuning of resistivity was done to match the I-V characteristics curve obtained from theoretical models with those obtained from the experiment. This tuning yields a resistivity of 1.75×10^{-3} ohm-cm for Design (1b) which is same as that of Design (1a). The comparison of the tuned I-V characteristics is shown in Figure 4.11. Again excellent agreement is observed when revised value of resistivity is used.

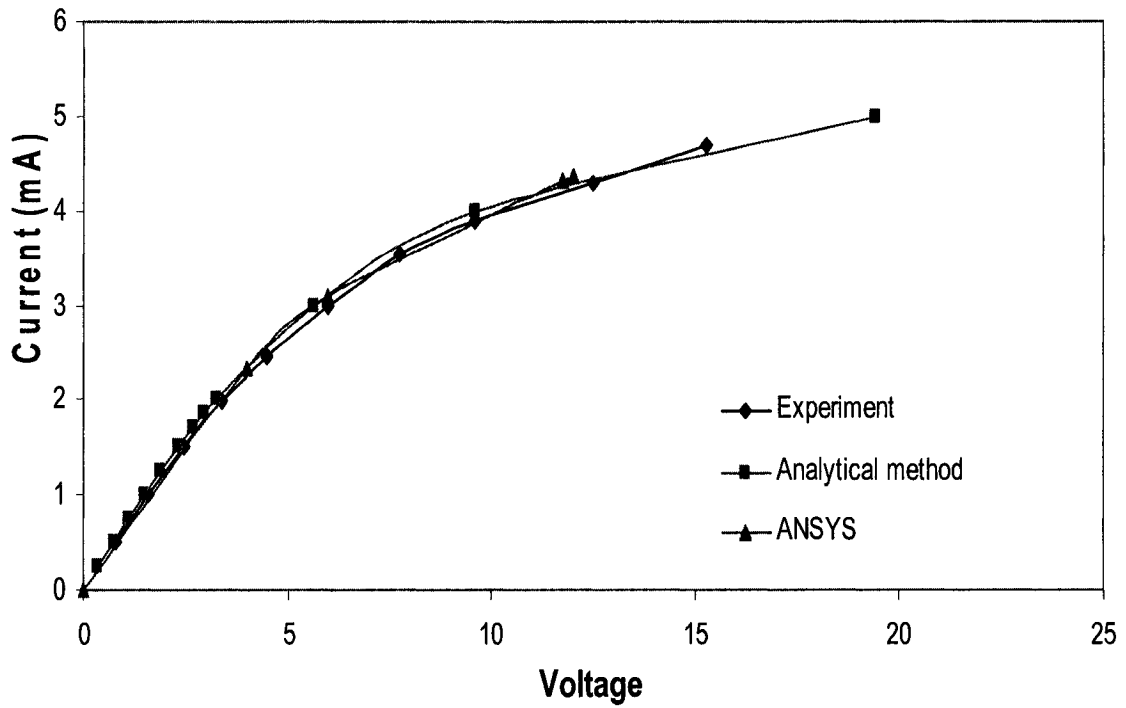


Figure 4.11: I-V Characteristics curve based on tuned resistivity for Design (1b) with $\rho_0 = 1.75e-3$ ohm-cm

Figure 4.12 shows photograph taken on Design (1b) before and after application of 3.091V. Angle of rotation is measured in a similar fashion as described in previous sections and was found to be 0.24 degrees in this case.

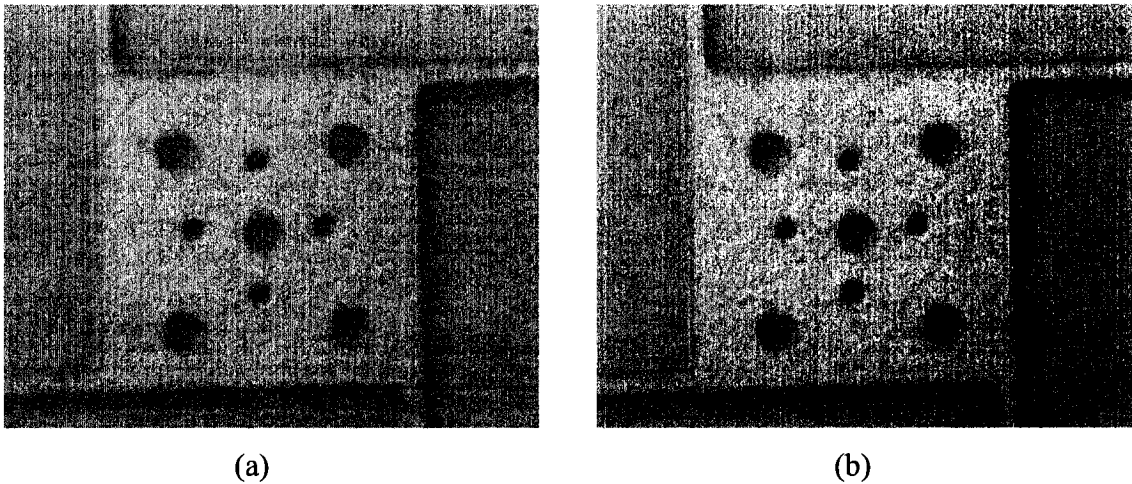


Figure 4.12: (a) Picture of the disc taken before applying voltage and (b) picture of the disc taken after application of 3.091V

Further results used for estimation of rotation angle corresponding to other voltages, are presented in Appendix-B. Rotary motions obtained from the simulation of theoretical models are compared with that obtained from the experiment in Figure 4.13 and was found to be in close agreement with the ANSYS results.

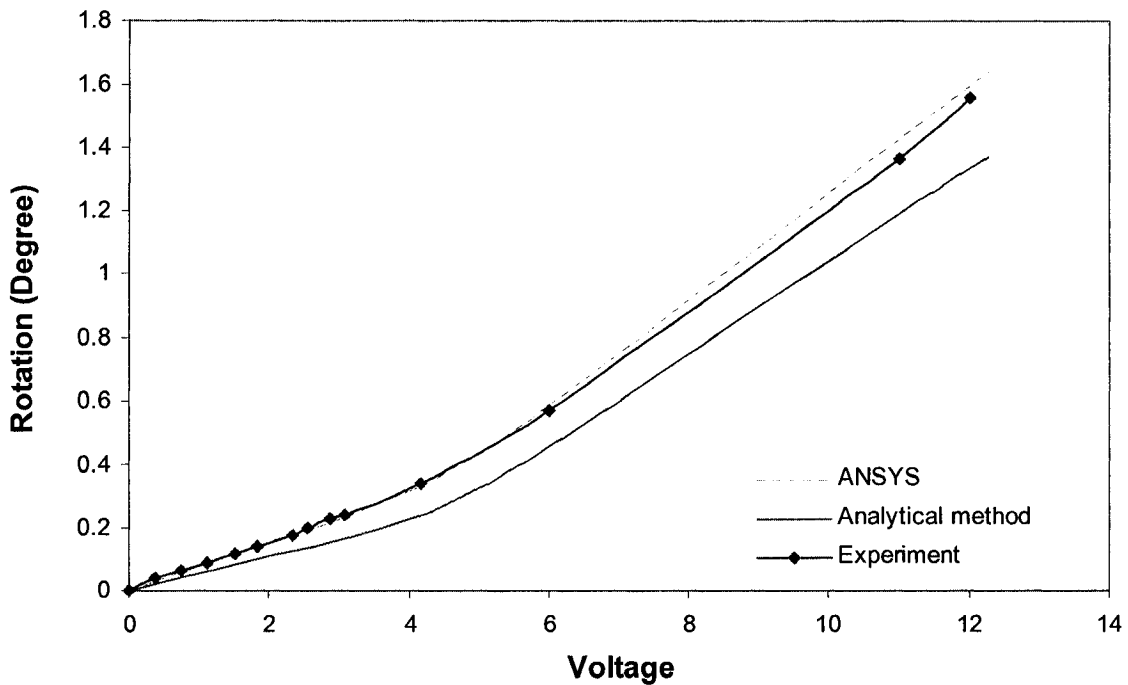


Figure 4.13: Variation of rotation against the applied voltages for Design (1b)

4.3.3 Validation for Design (2)

Similar to design (1a) and (1b), the I-V characteristic curve for Design (2) is presented in Figure 4.14. A comparison of analytical and ANSYS results with those of experiment show similar trend as those observed for Design (1a) and (1b). The deviation is again attributed to the uncertainty in the value of resistivity. Tuning of resistivity was done to match the I-V characteristics curve obtained from theoretical models with that of obtained from the experiment. This tuning yields a resistivity of 1.75×10^{-3} ohm-cm for

Design (2) which is same as that of Design (1a) and (1b). The comparison of the tuned I-V characteristics is shown in Figure 4.15.

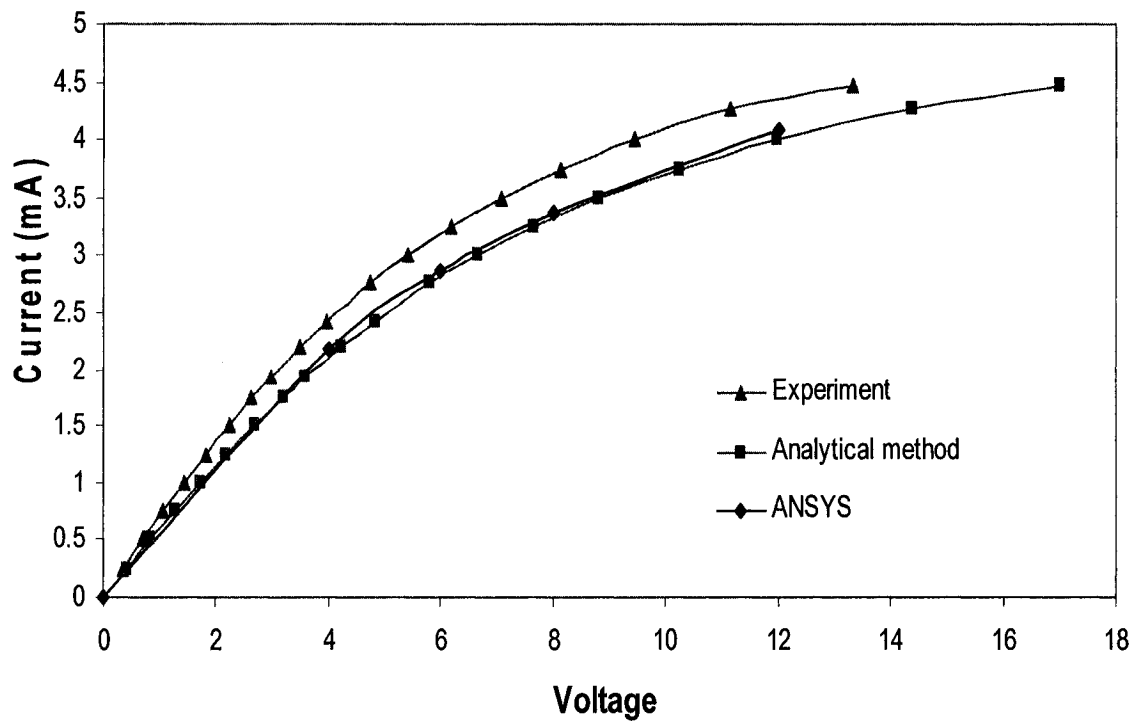


Figure 4.14: I-V Characteristics curve for Design (2) with $\rho_0 = 2 \times 10^{-3}$ ohm-cm

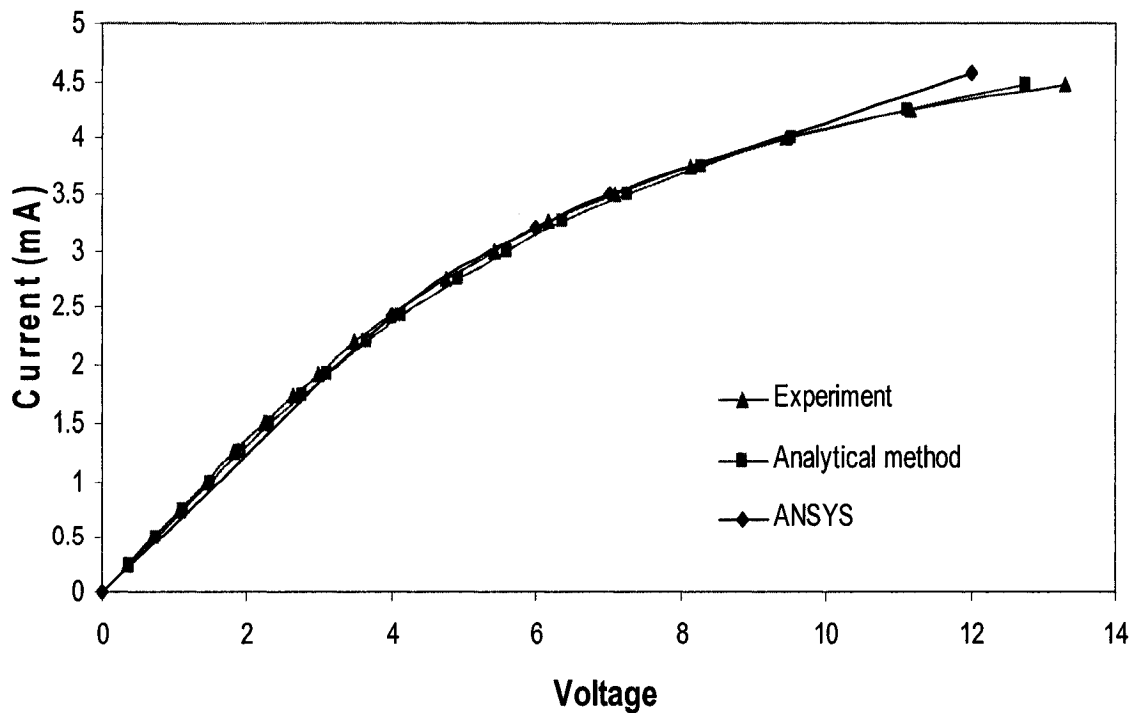


Figure 4.15: I-V Characteristics curve based on tuned resistivity for Design (2) with $\rho_0 = 1.75 \times 10^{-3}$ ohm-cm

Figure 4.16 shows photograph taken on Design (2) before and after application of 13.31V. Angle of rotation is measured in a similar fashion as described in previous sections and was found to be 1.54 degrees in this case.

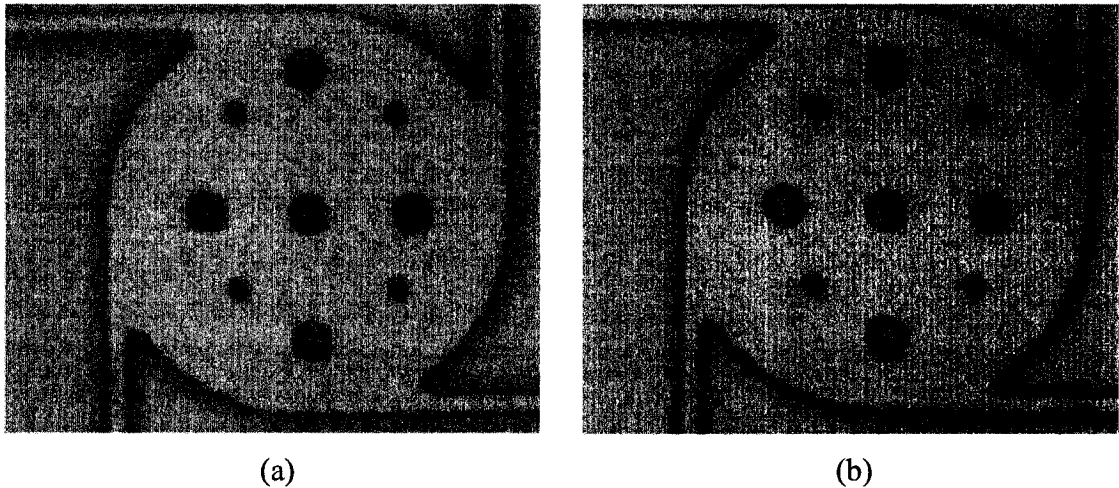


Figure 4.16: (a) Picture of the disc taken before applying voltage and (b) picture of the disc taken after application of 13.31V

Further results used for estimation of rotation angle corresponding to other voltages, are presented in Appendix-B. Rotary motions obtained from the simulation of theoretical models are compared with that obtained from the experiment in Figure 4.17. The results show excellent agreement with those predicted using analytical model specially for low voltages. As the voltage is increased beyond 6Volts, the experimental rotation is slightly lower than those predicted by analytical method, but are more close to the motion predicted by ANSYS.

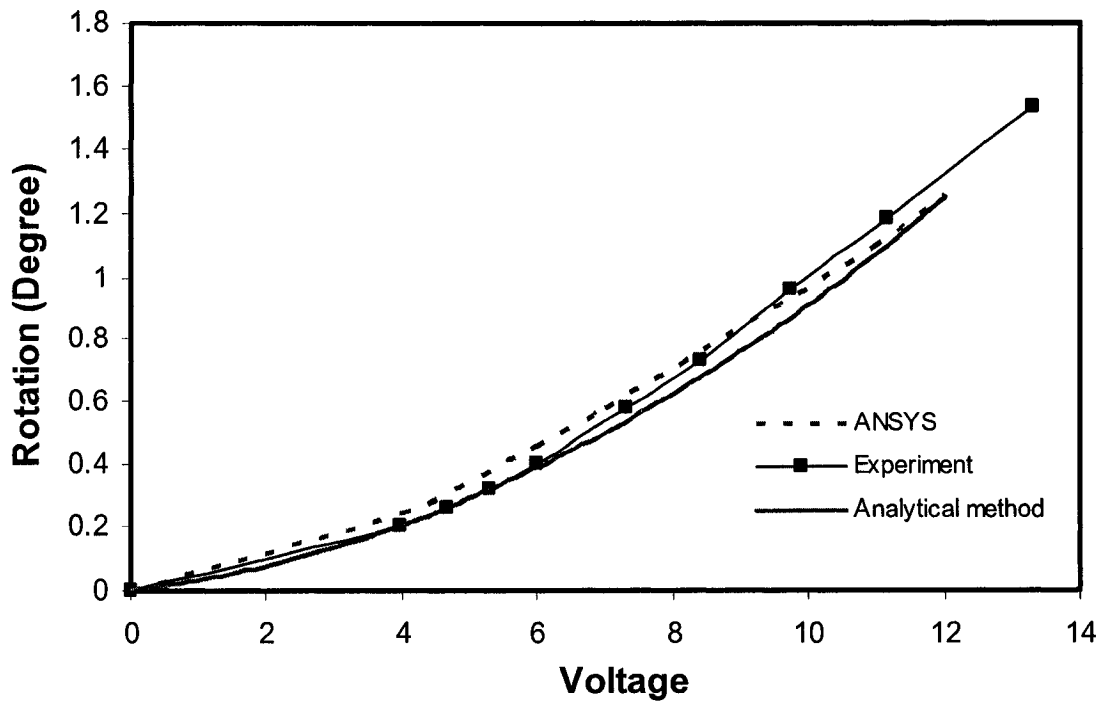


Figure 4.17: Variation of rotation against the applied voltages for Design (2)

Comparison of rotational behavior of the cold disc obtained from experiment with those from analytical model ANSYS for Design (1a), (1b) and (2) in previous sections show close agreement. Thus analytical and ANSYS models are validated. Also the experimental and theoretical results validate the feasibility of rotary type thermal actuator which will have many applications in Optical MEMS.

Chapter 5

Conclusion and Future work

Due to the numerous benefits, micro electro thermal actuator is still explored for new designs. A new rotary type micro thermal actuator is presented in this thesis. Various design topologies for this new actuator were also considered for the maximum rotation of the disc. The thesis presented design and modeling of rotary type thermal actuator with test results. The devices were fabricated in MUMPS technology as this is a widely famous fabrication technology for micro thermal actuator.

In Chapter 3, different modeling techniques for the device are detailed. Also a finite element solution for the device using ANSYS is presented. A close agreement was found between the results obtained from various mathematical models and ANSYS.

A parametric analysis is also presented in Chapter 3. This analysis shows that decreasing cold disc dimension increases rotation of the actuator. It was also found that the increasing beam length also increases actuator rotation. Design (1a) and (1b) which are identical in topology but have different number of arms, provide almost the same rotation. Despite of this fact, Design (1b) is favored as it is expected to be structurally more stable because of more number of arms.

It may be noted that minimum disc radius is usually restricted by the fabrication technology limitation. Designing a longer beam is restricted by the melting temperature

of the beam. The cold disc supported by longer narrow beam may result in sagging on the substrate where as gap between the structure and the substrate is very important for the heat generation of an actuator fabricated in MUMPS. Also, the parametric analysis helped to select loading condition that yields more rotation.

An experimental scheme used for the operation and measurement of the device is presented in Chapter 4. I-V characteristics curves that were obtained based on a standard Polysilicon1 resistivity from analytical and ANSYS, had a mismatch with those from experiments. The probable reasons for this were that actual resistivity might be different from the standard one because of dopant level variation and etch holes were not modeled in the theoretical models. Tuning the resistivity by matching I-V curves yields Polysilicon1 resistivity of 1.75×10^{-3} ohm-cm at room temperature. Photographs taken on the disc before and after application of voltages, show that the proposed design works. It is observed that the rotation obtained from the experiment for various designs show close agreement with those from theoretical model.

As a future work, effect of convection, radiation, geometrical nonlinearity, temperature dependent properties, thermal buckling, thermal cycling and creep can be studied on both static and dynamic behavior of the actuator. For simulation representing almost real life situation, consideration of etch holes and friction introduced by dimples with the substrate can be modeled. An analysis and testing of the device in vacuum condition may be carried out as vacuum reduces heat loss to the surrounding and increases rotation of

the actuator. Besides feasibility of this device in other fabrication technologies may be examined.

Finally the novel rotary thermal actuator presented in this application demonstrates its possible applicability for various optical applications such as, switching, attenuation, diffraction, etc.

Appendix A

Multi User MEMS Process

This appendix gives a brief description about Multi User MEMS Process (MUMPS) technology. MUMPS takes the benefit of 3 Polysilicon layers, 2 oxide layers, a nitride layer and a metal layer. Two polysilicon layers, namely Poly1 and Poly2 are used for fabricating devices and the first polysilicon layer can not be released from the structure. The oxide layers are used as sacrificial layers and the nitride layer is used electrical insulator between the polysilicon and the substrate. The metal layer is used as top layer of the device when a conductive layer is required.

The making of a structure in MUMPS can be synchronized as follows:

1. A silicon wafer is heavily doped with phosphorus in a standard diffusion furnace
2. A silicon nitride layer (0.5 micron thick) is deposited by LPCVD.
3. A layer of photo resist is deposited. The photo resist is patterned by exposing to UV light, developed and the exposed area is removed chemically. This creates an anchor hole for the silicon dioxide. The photo resist is stripped. This process is called photolithography. Photolithography is repeated for each sacrificial and structural layer.
4. A polysilicon layer called Poly0 (0.5 micron thick) is deposited and patterned by photolithography.
5. Poly0 is etched by reactive ion etching (RIE).
6. A phosphosilicate glass (PSG) layer called Oxide1 (2 micron thick) is deposited by LPCVD.

7. Dimple layer is patterned into Oxide1 and etched by RIE.
8. Anchor1 (this is a cut on the Oxide1 which facilitates the connection between the Poly1 and substrate) is patterned and etched by RIE.
9. A Polysilicon layer called Poly1 (2 micron thick) is deposited, covered with PSG and annealed at 1050°C.
10. Poly1 is patterned using photo resist through photolithography and etched by RIE.
11. Any remaining PSG is removed.
12. Oxide2 (0.75 microns thick) is deposited and patterned twice to get Poly1Poly2 via (P1P2via) and Anchor2. (a) P1P2via: this is a cut through Oxide2 that facilitates connection between Poly1 and Poly2 and (b) Anchor2: this is a cut through Oxide2 that facilitates connection between Poly2 and substrate.
13. A polysilicon layer called Poly2 (1.5 micron thick) is deposited, covered with PSG and annealed.
14. Poly2 is patterned and etched.
15. Any remaining PSG is removed.
16. Gold (0.5 microns thick) is deposited and patterned using lift-off.
17. A photo resist layer used as protective layer is applied
18. The wafer is diced for shipment.

MUMPS process has specific design rules for the allowable feature size and thickness and function of the layers. These rules limit the freedom to design more complex devices.

Figure A-1, shows cross section view of the layers involved in the fabrication of an electro static motor [47] fabricated by the MUMPS process. And the following Figure b shows cross section of structure after sacrificial oxide release.

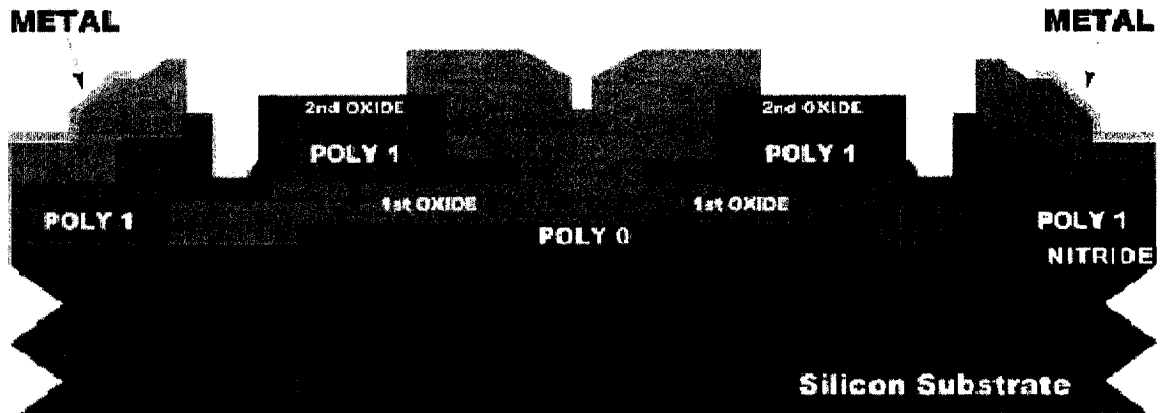


Figure A-1: Cross section of Electrostatic motor after the process is completed [47]

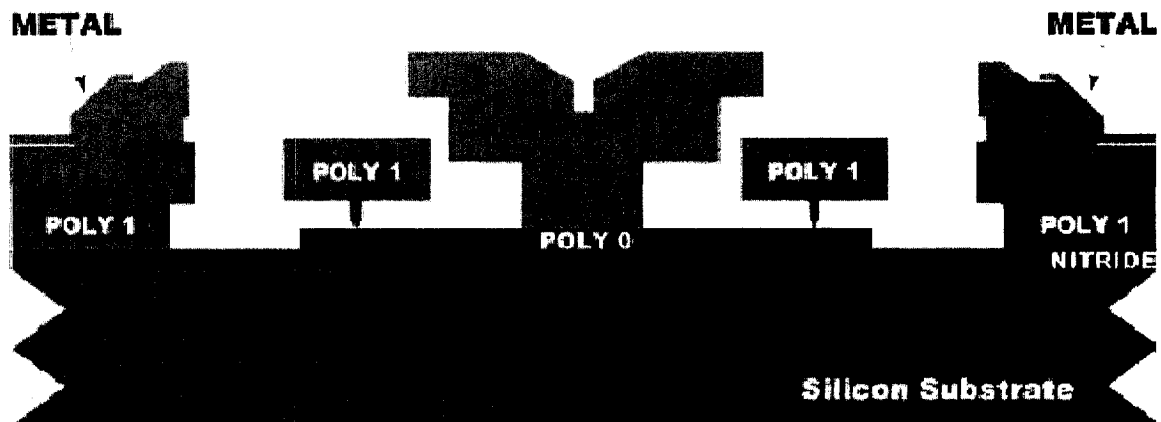
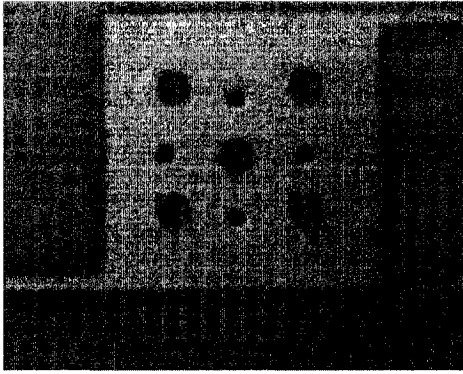
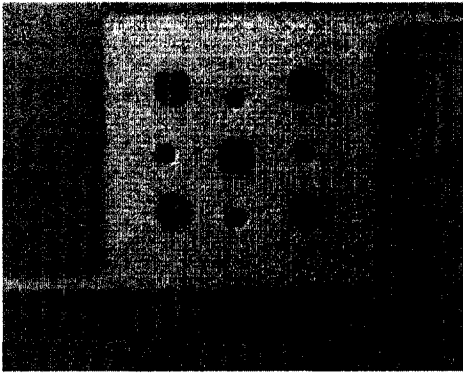
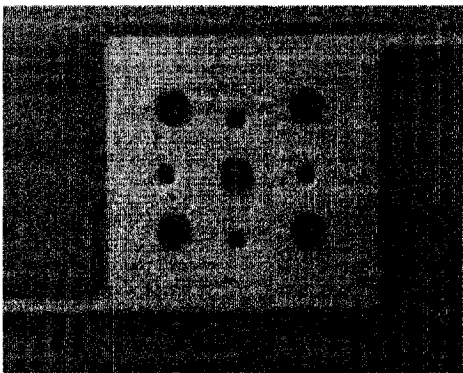
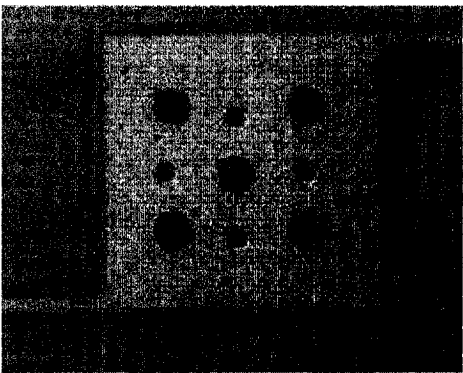


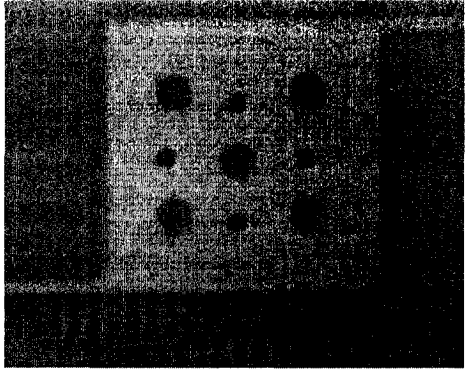
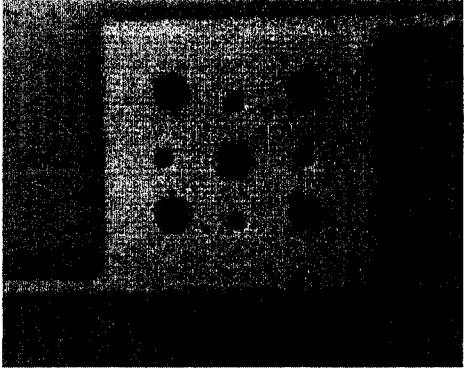
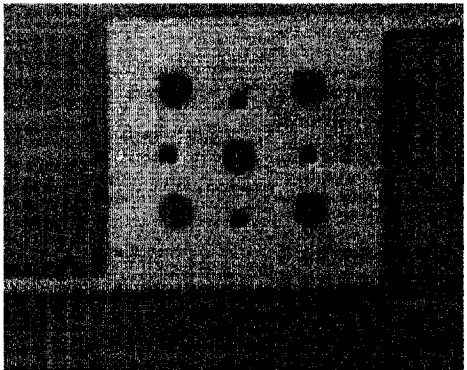
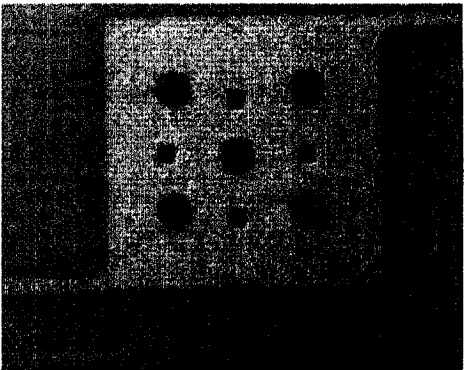
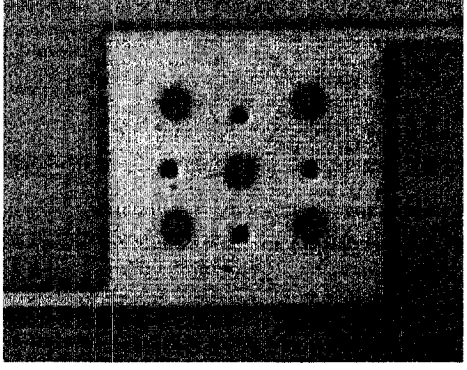
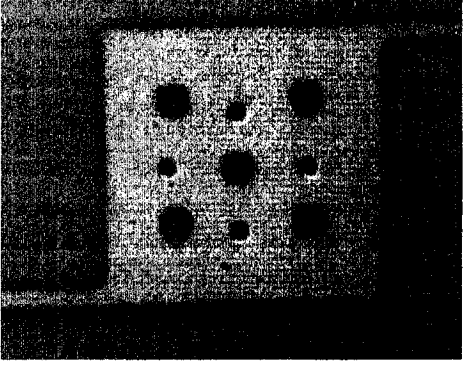
Figure A-2: Cross section of Electrostatic motor after release [47]

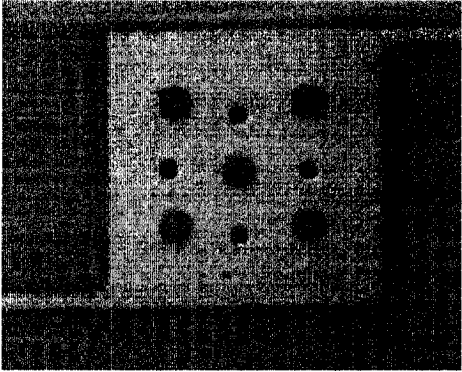
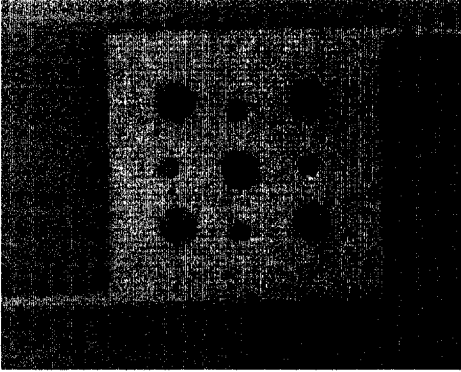
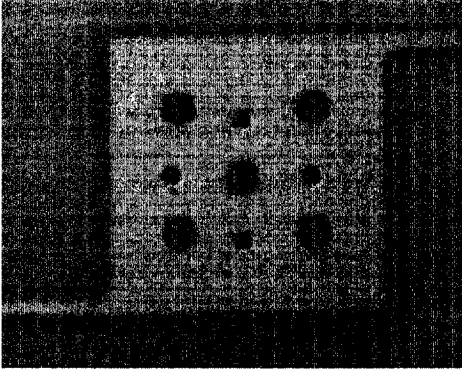
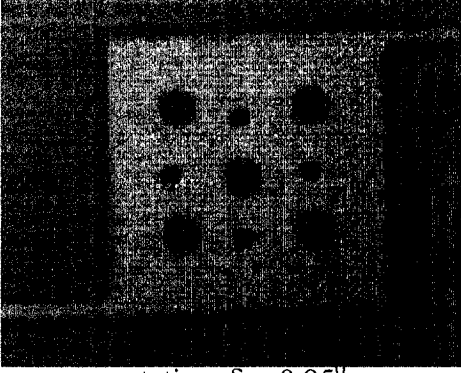
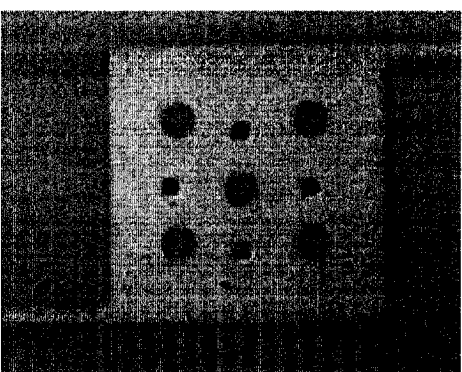
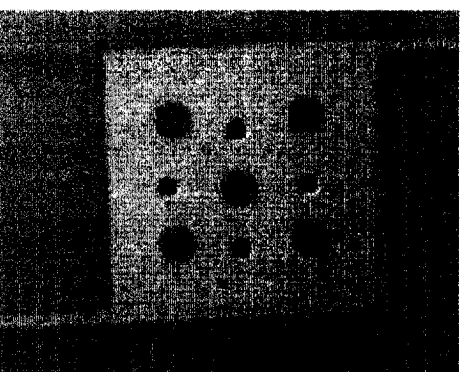
Appendix-B

This appendix contains photographs taken on Design (1a), (1b) and (2) before and after application of different voltages in the following tables-

Table B-1: Experiment photographs on Design (1a)

Voltage	Before application of voltage	After application of voltage
0.794V		 rotation, $\delta = 0.03^{\circ}$
1.598V		 rotation, $\delta = 0.06^{\circ}$

3.4V		 <p data-bbox="1089 628 1325 672">rotation, $\delta = 0.16^\circ$</p>
4.49V		 <p data-bbox="1081 1153 1333 1196">rotation, $\delta = 0.258^\circ$</p>
5.97V		 <p data-bbox="1089 1668 1325 1712">rotation, $\delta = 0.41^\circ$</p>

7.73V		 <p data-bbox="1089 628 1325 672">rotation, $\delta = 0.64^\circ$</p>
9.69V		 <p data-bbox="1089 1081 1325 1124">rotation, $\delta = 0.95^\circ$</p>
12.28V		 <p data-bbox="1078 1627 1333 1670">rotation, $\theta = 1.485^\circ$</p>

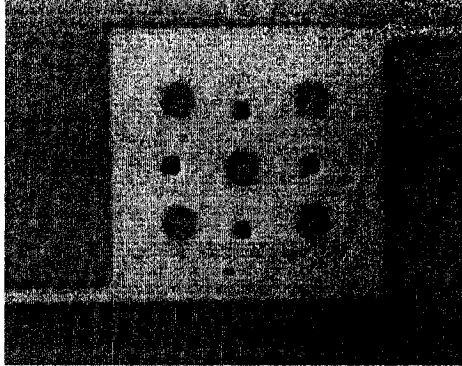
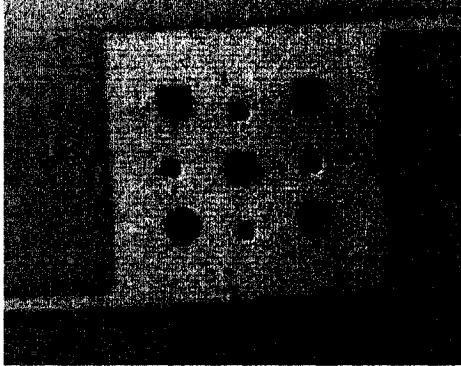
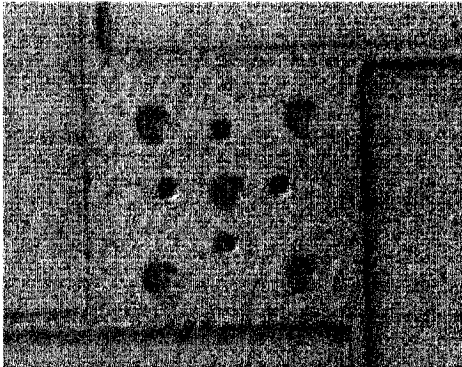
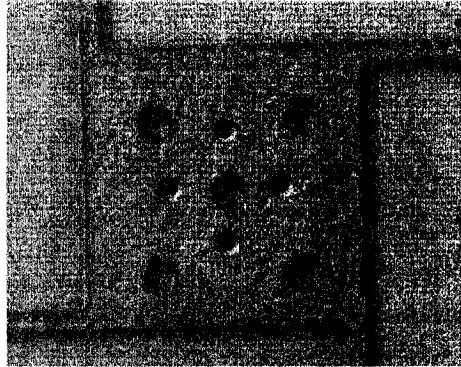
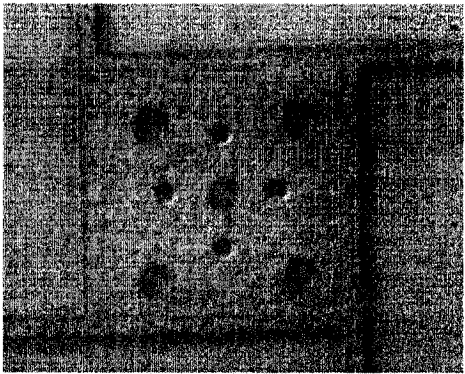
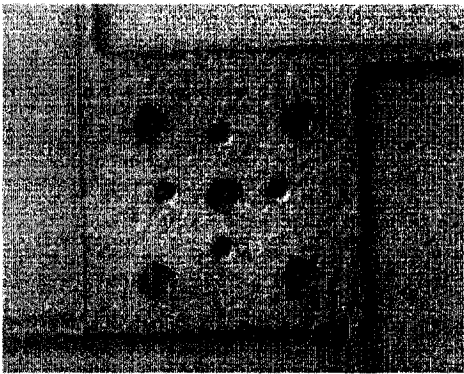
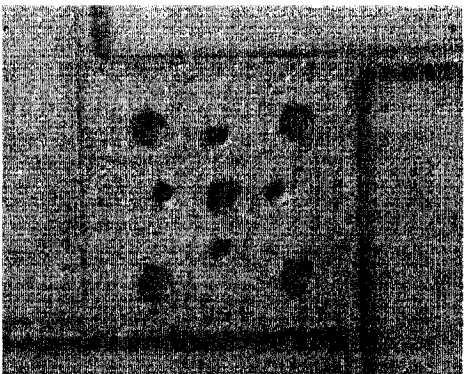
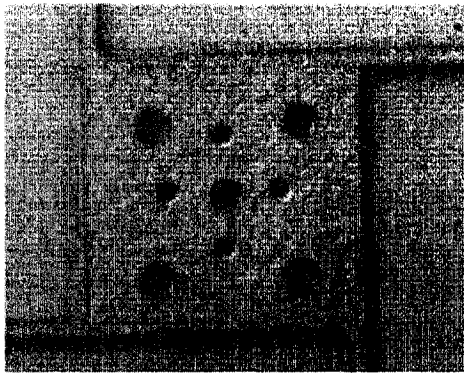
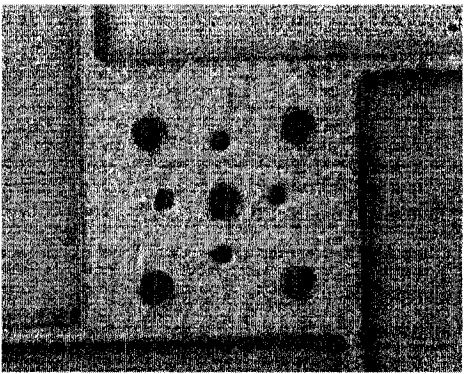
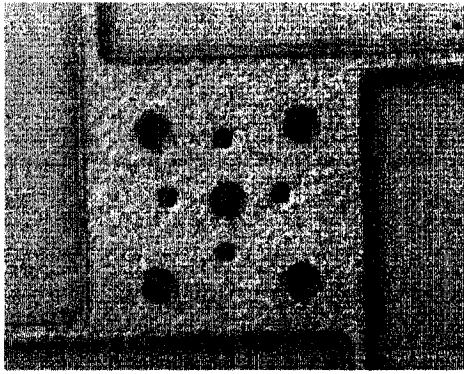
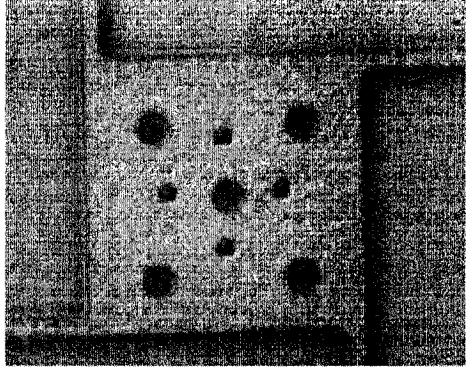
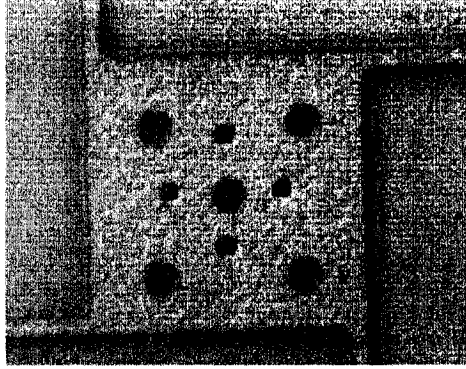
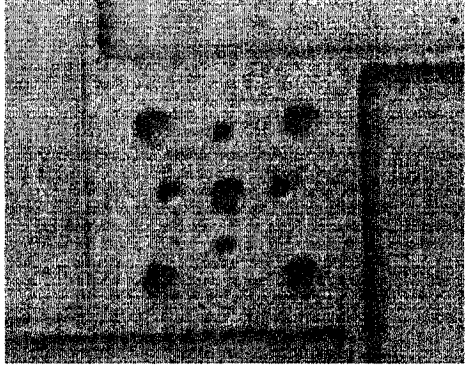
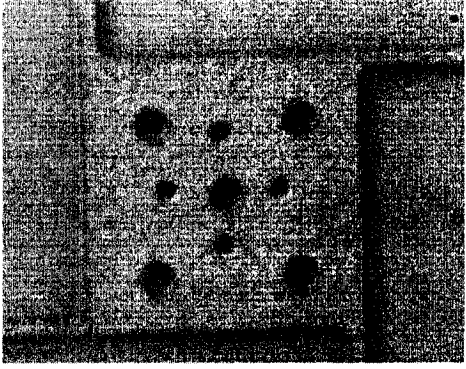
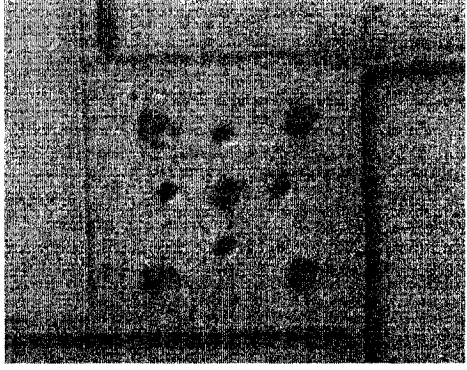
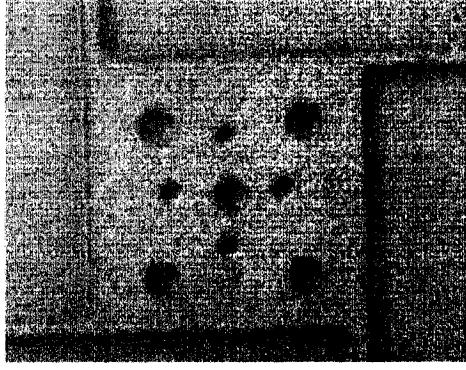
15.29V		 rotation, $\delta = 2.28444^\circ$
--------	---	--

Table B-2: Experiment Photographs on Design (1b)

Voltage	Before application of voltage	After application of voltage
0.375V		 rotation, $\delta = 0.04^\circ$

0.746V		 <p data-bbox="1081 628 1333 672">rotation, $\delta = 0.063^\circ$</p>
1.123V		 <p data-bbox="1081 1148 1333 1192">rotation, $\delta = 0.088^\circ$</p>
1.516V		 <p data-bbox="1081 1668 1333 1712">rotation, $\delta = 0.12^\circ$</p>

1.833V		 rotation, $\delta = 0.139^{\circ}$
2.35V		 rotation, $\delta = 0.177^{\circ}$
2.563V		 rotation, $\delta = 0.19891^{\circ}$

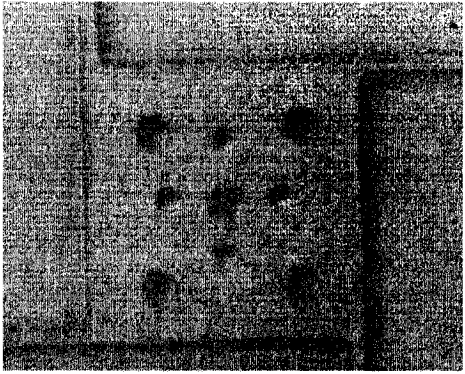
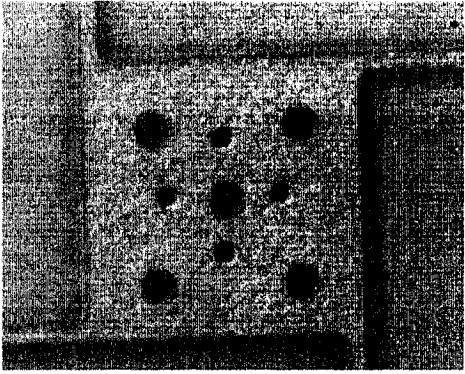
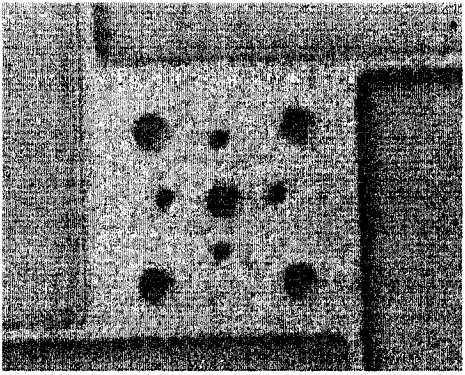
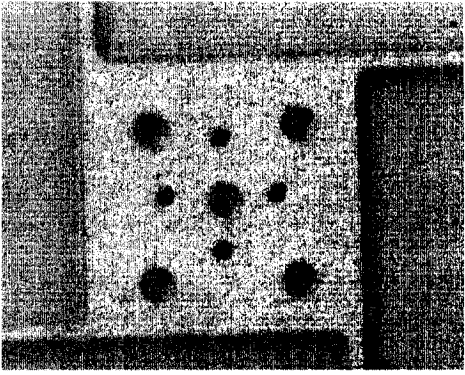
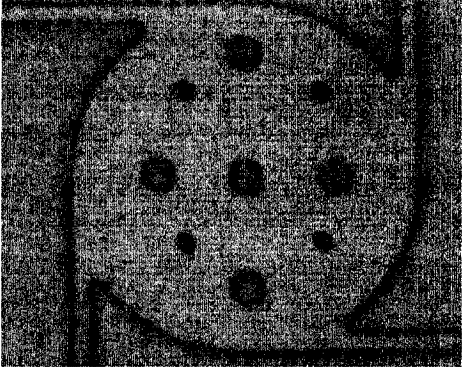
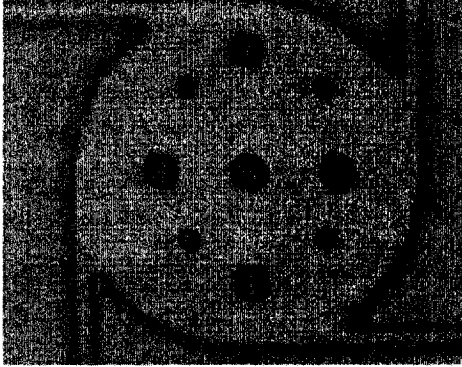
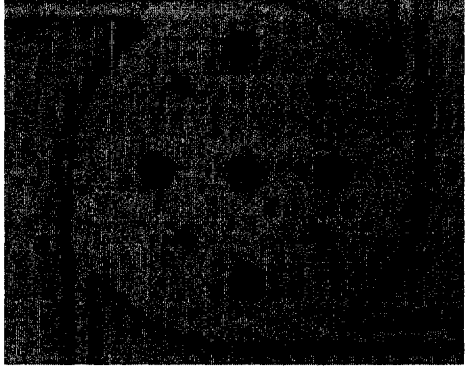

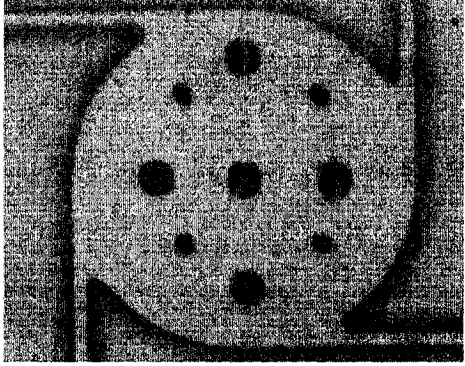
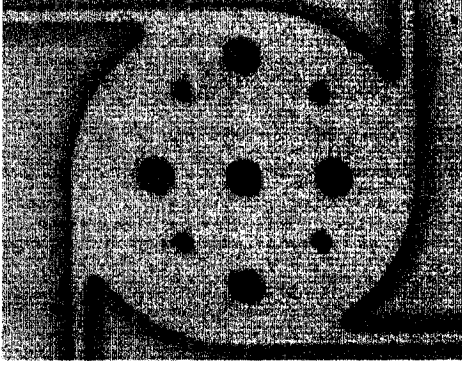
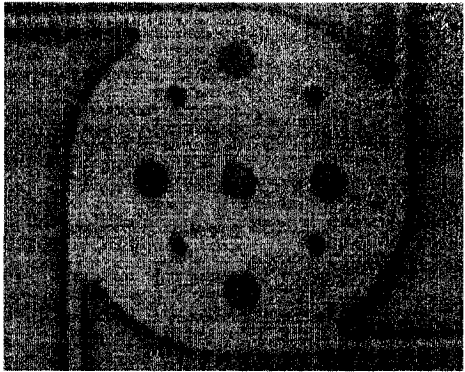
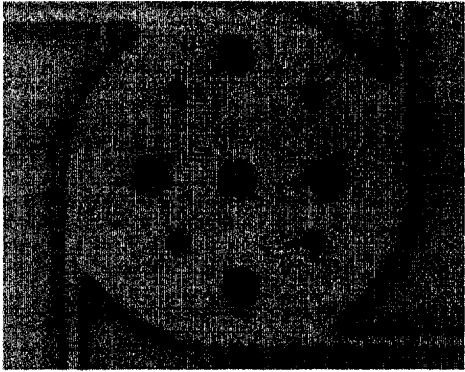
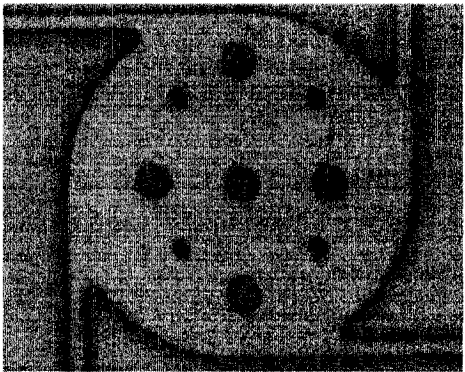
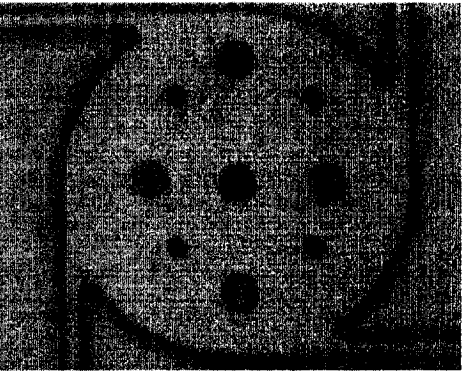
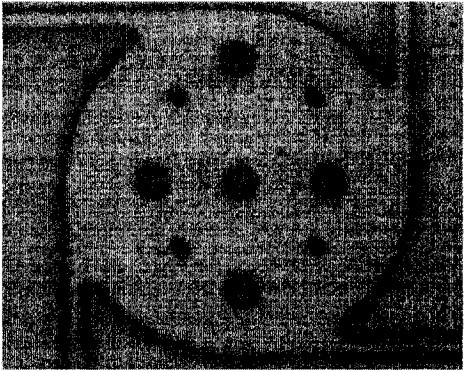
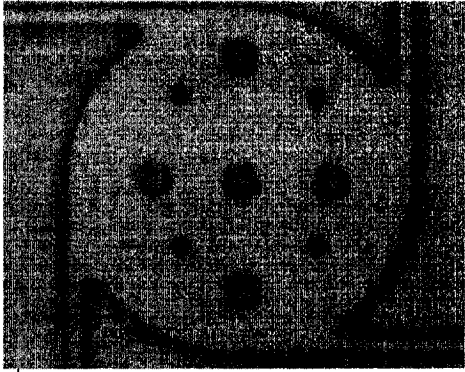
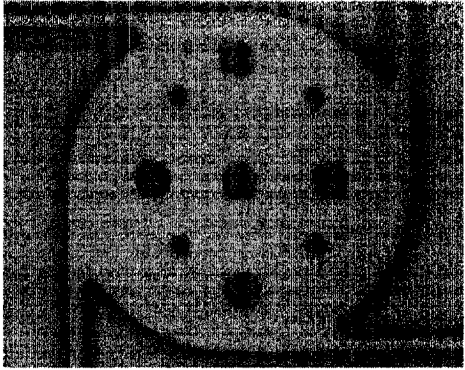
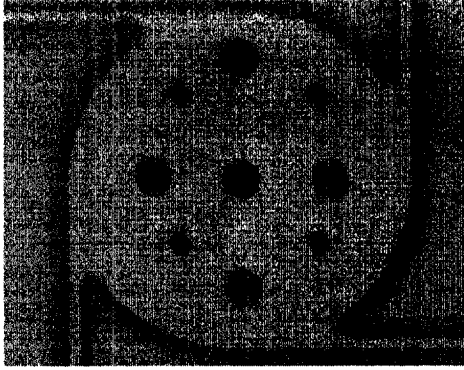
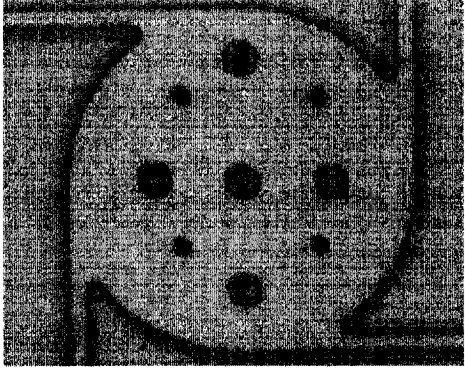
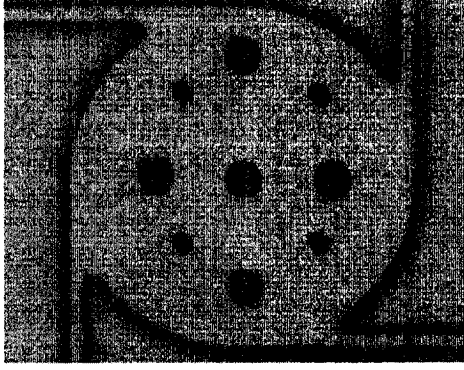
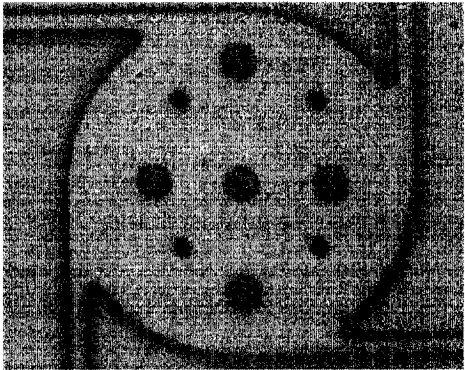
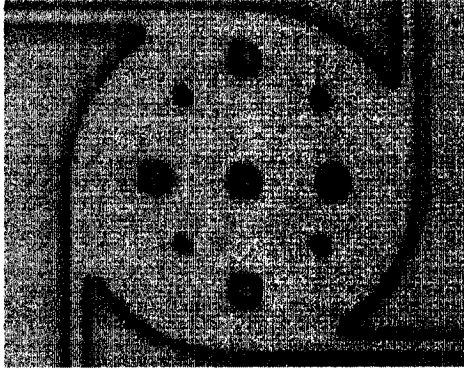
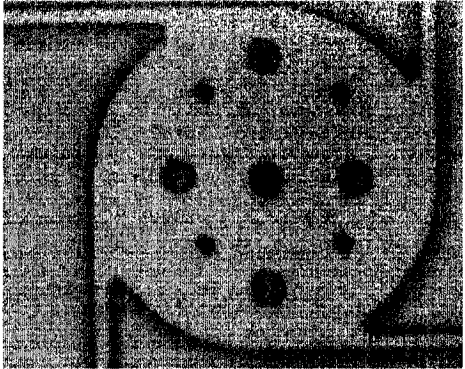
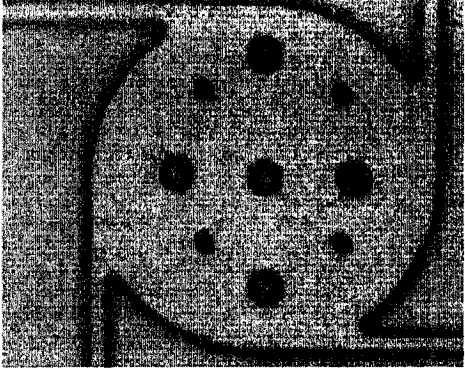
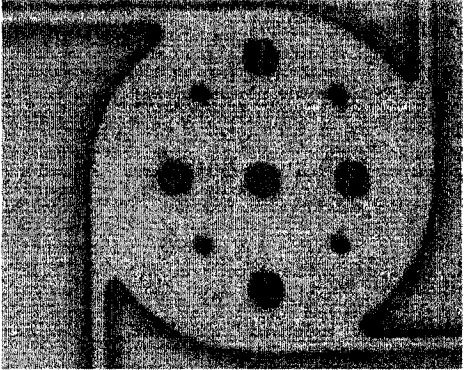
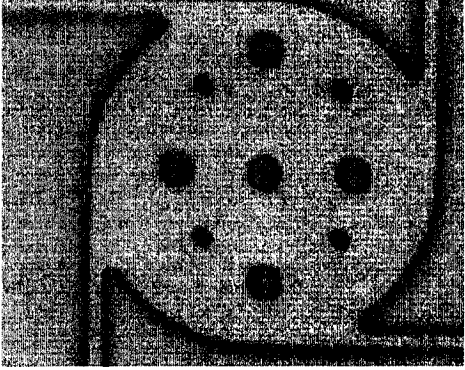
2.86V		 <p data-bbox="1063 635 1349 672">rotation, $\delta = 0.22625^\circ$</p>
3.091V		 <p data-bbox="1086 1153 1323 1190">rotation, $\delta = 0.24^\circ$</p>

Table B-3: Experiment Photographs on Design (2)

Voltage	Before application of voltage	After application of voltage
1.060V		
2.227V		
3.97V		 <p data-bbox="1057 1760 1360 1799">rotation, $\delta = 0.201611^{\circ}$</p>

4.67V		 <p data-bbox="1079 628 1336 672">rotation, $\delta = 0.259^\circ$</p>
5.3V		 <p data-bbox="1079 1153 1336 1196">rotation, $\delta = 0.317^\circ$</p>
6 V		 <p data-bbox="1096 1666 1320 1710">rotation, $\delta = 0.4^\circ$</p>

7.33V		 <p data-bbox="1078 628 1333 668">rotation, $\delta = 0.578^\circ$</p>
8.4V		 <p data-bbox="1078 1144 1333 1183">rotation, $\theta = 0.729^\circ$</p>
9.74V		 <p data-bbox="1078 1664 1333 1703">rotation, $\delta = 0.96^\circ$</p>

11.16V		 <p data-bbox="1057 628 1360 672">rotation, $\delta = 1.184614^{\circ}$</p>
13.31V		 <p data-bbox="1084 1153 1328 1196">rotation, $\delta = 1.535^{\circ}$</p>

References

1. Ohlckers, P. and Jackobsen, H., 'Challenges of the emerging Microsystems industry', *Microelectronics journal*, vol. 29, 1998, pp 587-600
2. Frazier, A.B., Warrington, R.O. and Friedrich, C., 'The miniaturization technologies: Past, present, and future', *IEEE Transactions on Industrial Electronics*, vol. 42., no 5, October 1995, pp. 423-430
3. Turner, P., *MEMS and Microstructure technology (MST): An applications and market evaluation 2nd edition*, an executive white paper by Venture Development Corporation, Massachusetts, August 2002
4. Wicht Technologie Consulting on behalf of NEXUS, 'NEXUS market analysis for MEMS and Microsystems III, 2005-2009', 2006
5. Sasaki, M., Bouno, F. and Hane, K., 'Electrostatically driven two-dimensional mems actuator', A short presentation in First International Workshop on Networked Sensing Systems Program-INSS 2004, Japan, June 2004,
6. Yasseen, A. A., Mitchell, J. N., Klemic, J. F., Smith, D. A. and Mehregany, M., 'A rotary electrostatic micromotor 1x8 optical switch', *IEEE journal of selected topics in Quantum Electronics*, vol. 5, no. 1, 1999, pp. 26-32
7. Grade, J. D. and Jerman, H., 'MEMS electrostatic actuators for optical switching applications', *Conference on Optical Fiber Communications, Technical Digest Series*, v. 54, n. 3, pp. WX2/1-WX2/3
8. Petersen, K.E., 'Silicon as a mechanical material', *Proceedings of IEEE*, vol. 70, no5, May 1982, pp. 420-457

9. Howe, R.T. and Muller, R.S., 'Polycrystalline silicon micromechanical beams', Journal of Electrochemical society: Solid state science and technology, June 1983, pp. 1420-1423
10. Howe, R.T. and Muller, R.S., 'Resonant microbridge vapor sensor', IEEE transactions on Electron Devices, vol. ED-33, no 4, April 1986, pp. 499-506
11. Guckel, H., Klein, J., Christenson, T., Skrobis, K., Laudon, M. and Lovell, E., 'Thermo-magnetic metal flexure actuators', Technical digest, Solid State Sensor and Actuator Workshop, 1992, pp. 73-75
12. Comtois, J.H. and Bright, V.M., 'Surface micromachined polysilicon thermal actuator arrays and applications', Technical Digest, Solid State Sensor and Actuator workshop, Hilton Head, SC, 1990, pp 174-177
13. Comtois, J.H. and Bright, V.M., 'Design techniques for surface-micromachining MEMS processes', Proceeding of SPIE, vol. 2639, 1995, 211-222
14. Comtois, J.H., Bright, V.M and Phipps, M.W., 'Thermal microactuators for surface micromachining processes', Proceeding of SPIE, vol. 2642, 1995, pp. 10-21
15. Comtois, J.H. and Bright, V.M, 'Applications for surface-micromachined polysilicon thermal actuators and arrays', Sensors and Actuators A, vol. 58, 1997, pp 19-25.
16. Butler, J.T., Bright V.M. and Reid, J.R., 'Scanning and rotating micromirrors using thermal actuators', Proceeding of SPIE, vol. 3131, 1997, pp. 134-144.

17. Lerch, P., Slimane, C.K., Romanowicz, B. And Renaud, Ph., 'Modelization and characterization of asymmetrical thermal micro-actuators' Journal of Micromechanics and Microengineering, vol. 6, 1996, pp 134-137
18. Reid, J. R., Bright, V. M. and Comtois, J.H., 'Force measurements of polysilicon thermal microactuators', Micromachined Devices and Components, SPIE, vol. 2882, 1996, pp. 296-300
19. Comtois, J.H., Michalick, M. A. and Barron, C.C., 'Electrothermal actuators fabricated in four-level planarized surface micromachined polycrystalline silicon', Sensors and Actuators A vol. 70, 1998, pp. 23-31
20. Sandia National Laboratory, World wide web address: <http://www.mdl.sandia.gov>
21. Butler, J.T., Bright, V.M. and Cowan, W.D., 'SPICE modeling of polysilicon thermal actuators', Proceedings of SPIE, vol. 3224, 1997, pp. 284-293
22. Butler, J.T. and Bright V.M., 'Electrothermal and fabrication modeling of polysilicon thermal actuators', ASME DSC-MEMS, vol. 66, 1998, pp. 571-576
23. Kolesar, E.S., Allen, P.B., Howard, J.T., Wilken, J.M. and Boydston, N., 'Thermally actuated cantilever beam for achieving large in-plane mechanical deflections', Thin Solid Films, vol. 355-356, 1999, pp. 295-302
24. Burns, David M. and Bright, Victor M., 'Design and performance of a double hot arm polysilicon thermal actuator', Proceedings of SPIE, vol. 3224, 1997, pp. 296-306
25. Kolesar, E.S., Ruff, M.D., Odom, W.E., Jayachadran, J.A., McAllister, J.B., Ko, S.Y., Howard, J.T., Allen, P.B., Wilken, J.M., Boydston, N.C., Bosch, J.E. and Wilks, R.J., 'Single- and double-hot arm asymmetrical polysilicon surface

- micromachined electrothermal microactuators applied to realize a microengine',
Thin Solid Films, vol. 420-421, 2002, pp. 530-538
26. Li, J. and Ananthasuresh, G.K., 'Microfabrication and characterization of electro-thermal-compliant micro devices', Proceedings of DETC '00, ASME 2000 Design Engineering Technical Conference and Computers and Information in Engineering Conference; Baltimore, Maryland; September 10-13, 2000; pp. 621-633
27. Moulton, T. and Ananthasuresh, G.K., 'Micromechanical device with embedded electro-thermal-compliant actuation', Sensors and Actuators A, vol. 90, 2001, pp. 38-45
28. Pan, C.S. and Hsu, W., 'An electro-thermally and laterally driven polysilicon microactuator', Journal of Micromechanics and Microengineering, vol. 7, 1997, pp. 7-13
29. Lee, C.C. and Hsu, W., 'Optimization of an electro-thermally and laterally driven microactuator', Microsystem Technologies, vol. 9, 2003, pp. 331-334
30. Mankame, N.D and Ananthasuresh, G.K., 'Effect of thermal boundary conditions and scale on the behavior electro-thermal-compliant micromechanisms', Proceedings of Modeling and Simulation of Microsystems, 2000, pp. 609-612
31. Mankame, N.D. and Ananthasuresh, G.K., 'Comprehensive thermal modeling and characterization of an electro-thermal-compliant microactuator', Journal of Micromechanics and Microengineering, vol. 11, 2001, pp. 1-11
32. Lin, L. and Chiao, M., 'Electrothermal responses of lineshape microstructures', Sensors and Actuators A., vol. 15, 1996, 35-41

33. Hickey, R., 'Analysis and optimal design of micro-machined thermal actuators', M.A.Sc. Thesis, Dalhousie University, Nova Scotia, Canada 2001
34. Hickey, R., Sameoto, D., Hubbard, T. and Kujath, M., 'Time and frequency response of two-arm micromachined thermal actuators', Journal of Micromechanics and Microengineering, vol. 13, 2003, pp. 40-46
35. Huang, Q.A. and Lee, N.K.S., 'Analytical modeling and optimization for a laterally-driven polysilicon thermal actuator', Microsystem Technologies, vol. 5, 1999, pp. 133-137
36. Huang, Q.A. and Lee, N.K.S., ' Analysis and design of polysilicon thermal flexure actuator', Journal of Micromechanics and Microengineering, vol. 9, 1999, pp. 64-70
37. Huang, Q.A. and Lee, N.K.S., 'A simple approach to characterizing the driving force of polysilicon laterally driven thermal microactuators', Sensors and Actuators, vol. 80, 2000, 267-272
38. Lott, C.D., McLain, T.W., Harb, J.N., and Howell, L.L., 'Thermal modeling of a surface micromachined linear thermomechanical actuator', Modeling and Simulation of Microsystems, 2001, pp. 370-373
39. Lott, C.D., McLain, T.W., Harb, J.N. and Howell, L.L., 'Modeling the thermal behavior of a surface-micromachined linear-displacement thermomechanical microactuator', Sensors and Actuators A, vol. 101, 2002, pp. 239-250
40. Yan, D., Khajepour, A. and Mansour, R., 'Modeling of two-hot-arm horizontal thermal actuator', Journal of Micromechanics and Microengineering, vol. 13, 2003, pp. 312-322

41. Yan, D., Khajepour, A. and Mansour, R., 'Design and modeling of a MEMS bidirectional vertical thermal actuator', Journal of Micromechanics and Microengineering, vol. 14, 2004, pp. 841-850
42. Li, L. and Uttamchandani, D., 'Modified asymmetric micro-electrothermal actuator: analysis and experimentation', Journal of Micromechanics and Microengineering, vol. 14, 2004, pp. 1734-1741
43. Luo, J., He, J. H., Flewitt, A., Moore, D.F., Spearing, S.M., Fleck, N.A., Milne, W.I, 'Development of all metal electrothermal actuator and its applications', Journal of Microlithography, Microfabrication and Microsystems, vol. 4(2), 2005, 1537-1646
44. Atre, A. and Boedo, S., 'Effect of Thermophysical property variations on surface micromachined polysilicon beam flexure actuators', NSTI-Nanotech 2004, vol. 2, 2004, pp. 263-266
45. Calliester, W. D. Jr., Materials Science and Engineering- An Introduction, Sixth edition, John Wiley & Sons Inc.
46. French, P.J. and Sarroe, P.M., 'Surface versus bulk micromachining: the contest for suitable applications', Journal of Micromechanics and Microengineering, vol. 8, 1998, pp. 45-53
47. Cronos Integrated Microsystems, 3026 Cornwallis Road, Research Triangle Park, NC 27709